2008

Endurance materials for hydrogen sulfide splitting in electrolytic cell

Jonathan Chinwendu Mbah
University of South Florida

Endurance Materials for Hydrogen Sulfide Splitting in Electrolytic Cell

by

Jonathan Chinwendu Mbah

A dissertation submitted in partial fulfillment
of the requirements for the degree of
Doctor of Philosophy
Department of Chemical and Biomedical Engineering
College of Engineering
University of South Florida

Major Professor: John T. Wolan, Ph.D.
Yogi Goswami, Ph.D.
Elias Stefanakos, Ph.D.
Vinay Gupta, Ph.D.
Matthias Batzill, Ph.D.
Burton Krakow, Ph.D.

Date of Approval:
November 5, 2008

Keywords: Solid Acid, Permeability, CsHSO4, Ionic Conductivity, RuO2/CoS2

ACKNOWLEDGEMENTS

To my Creator from whom all good things come, I glorify. Thanks to all my advisors, colleagues, friends, and family members for making this journey possible.

TABLE OF CONTENTS

LIST OF TABLES

LIST OF FIGURES

ENDURANCE MATERIALS FOR HYDROGEN SULFIDE SPLITTING IN ELECTROLYTIC CELL

Jonathan Chinwendu Mbah

ABSTRACT

This study describes the development of a novel thin membrane exchange assembly (MEA) from a solid acid material, cesium hydrogen sulfate ($CsHSO_4$), and from a composite anode electrocatalyst for electrolytic splitting of (100 %) H_2S feed content gas operating at 135 kPa and 150 ^oC. A new class of anode electrocatalyst with the general composition, RuO_2/CoS_2, and an improved proton conductor, $CsHSO_4$, have shown great stability and desired properties at typical operating conditions. This configuration demonstrated stable electrochemical operation for 24 h with a (100 %) H_2S fuel stream at 423 K. This same system showed a maximum current density of (19 mA/cm^2) at 900 mV. The performance of this new anode electrocatalyst when compared to that of Pt black investigated in a previous study showed an overall superiority in application. We have achieved a 30 % reduction in the overall system performance by fabricating a thin (200 μm) $CsHSO_4$ electrolyte, which reduced the whole MEA thickness from 2.3 mm to 500 μm. The result of permeability measurements proved that this thin solid electrolyte is impermeable to H_2S gas and physical integrity was preserved throughout the experimental period. Further resistance losses were compensated by using a high energy planetary milling system to enhance the ionic conductivity of $CsHSO_4$. The difference in

stability and electrochemical performance of these cells compared to that of Pt anode based systems is directly attributable to the anode materials developed in this project.

Factorial experiments were used to characterize the effect of controllable process variables (electrolyte thickness, time, age of the electrolyte) on the cell current density and interfacial polarization resistances. As expected, cell current density and interfacial polarization resistances were a function of electrolyte thickness and age. Nevertheless, the effect of electrolyte thickness has a more prominent effect on the measured parameters. In addition, these experiments were used to identify regions of optimum system performance.

Tafel plots were constructed to investigate the kinetic behavior of various anode based electrocatalysts. Exchange current densities, which are directly a measure of the electrochemical reaction, increased with RuO_2/CoS_2-based anodes. These experiments also suggested that high levels of feed utilization were possible using these materials. This was an impressive result considering the drastic improvement in electrochemical performance, current density, and sulfur tolerance compared to the other anode configurations.

1 INTRODUCTION

Hydrogen sulfide (H_2S) is extremely toxic and undesirable; yet over 12 million tons of it is produced annually in the US alone as a result of many industrial activities[1]. The rotten egg like smell accompanying it is disagreeable and the ability to detect it via smell diminishes rapidly with exposure, hence one can dangerously be exposed to a high concentration and yet be oblivious. Highly flammable under normal conditions- hydrogen sulfide readily forms explosive mixtures with air (4 % lower explosion limit, LEL, H_2S).

Many processes are available to eliminate H_2S but most of these processes are not efficient and generate other pollutants as well[2]. In addition, most processes are multistage which may require a huge capital investment. A common process used in H_2S splitting is the Claus process. In this process H_2S is extracted along with carbon dioxide in a stream called acid gas. Partial oxidation of the acid gas with air yields elemental sulfur and water with a waste stream of dilute carbon dioxide in nitrogen. Electrolytic splitting of the extracted hydrogen sulfide can yield sulfur and hydrogen (instead of sulfur and water). The carbon dioxide is separated before electrolysis, which leaves a concentrated carbon dioxide waste stream which is easier to sequester. The small Gibbs energy possessed by H_2S enables it to cleanly split into elemental sulfur and diatomic hydrogen with a low energy and voltage requirement. The energy benefit of electrolytic splitting of

the H_2S is illustrated in Eqns. (1.1, 1.2). The value of the hydrogen makes the system more profitable.

$$H_2S\,(g) \rightarrow S\,(l) + H_2\,(g) - 2 \text{ Faradays @ } 0.26V \quad \Delta G^{o} = 8.9 \text{ kcal/mole @ } 400K \qquad (1.1)$$

$$H_2O \rightarrow H_2 + O_2 - 2 \text{ Faradays @ } 1.2V \qquad \Delta G^{o} = 57 \text{ kcal/mole} \qquad (1.2)$$

Therefore, removal of H_2S from process gas streams electrochemically has many economic and environmental benefits. At present H_2S is not employed as a hydrogen or high-grade energy resource such as found in methanol or ethanol. Therefore, except for a process such as oil refining where a use for the heat generated by the Claus process is present, the capital investment can not be economically justified. Other disadvantages of the Claus process are that its hydrogen sulfide conversion efficiency is only about 92 percent and other pollutants such as CS_2 and COS are normally also produced by the Claus process[3]. Thus, for many applications, H_2S decomposition by the Claus method is not practical.

An electrolysis process requires a membrane exchange assembly (MEA) to provide both the reaction interface and the ion migration route. In addition, it provides a good surface for electron dispersal away from the reaction interface. Therefore, a good electrolyte capable of splitting H_2S gas to liquid sulfur and hydrogen is of utmost importance. The preference of solid electrolytes over liquid electrolytes has been proven in previous publications[4]. There is currently no published article on H_2S splitting to produce liquid sulfur and hydrogen using a solid acid electrolyte such as the one we reported here, but many articles have been published on H_2S splitting using different solid electrolytes[4]. In

most of these processes, H_2S containing gas was utilized as a feed in fuel cells to generate power and produces sulfur and H_2O.

The need for a solid electrolyte that maintains its integrity and proton conductivity at high temperatures and also allows the anode product, sulfur, to exist in liquid form so that it can easily flow out of the electrolytic cell without hindrance cannot be overemphasized. A group of solid acid electrolytes (SAE) have exhibited capability in there use as fuel cell membranes[5]. They belong to inorganic crystals, with intermediate properties between normal acids, such as H_2SO_4 or H_3PO_4, and normal salts, such as K_2SO_4[6]. Solid acids still have the capacity to act as proton donors even with only some of their normal acid's hydrogen atoms replaced[7]. To electrolyze H_2S we exploited these recent developments in SAE whose proton conductivities rise rapidly with temperature.

One other important components of the MEA are the electrocatalysts required to completely split H_2S into sulfur and hydrogen proton at the reaction interface. Electrocatalysis is the term used to indicate the catalysis of electrode reactions. This can be accomplished by the action of the electrode material[8]. In harmony with the field of heterogeneous electrocatalysis, heterogeneous electrocatalysis deals with the effect of the electrode material on the rate and the mechanism of electrode reactions[9]. In order to be a suitable candidate for the electrochemical splitting of H_2S, an anode material must possess good electrical conductivity and sulfur tolerance at high temperatures, in addition to good catalytic activity. Pt or Pt based anode catalysts have good catalytic activity, but degrade over time in H_2S streams. Moreover; most metals and metal oxides are severely

corroded by H_2S at elevated temperatures. A pyrochlore-based anode material, $Gd_2Ti_{1.4}Mo_{0.6}O_7$, showed remarkable tolerance to sulfur-containing fuels used in fuel cells application. The anode/electrolyte interfacial resistance was only 0.2 Ω cm^2 at 950 °C in a fuel gas mixture of 10 % H_2S and 90 % H_2, demonstrating a peak power density of 342 mW cm^{-2}. The fuel cell operated under these conditions continuously for 6 days without any observable degradation, suggesting that $Gd_2Ti_{1.4}Mo_{0.6}O_7$ anode exhibits not only excellent stability but also good catalytic activity toward the splitting of H_2S containing gas[10]. But a major draw back in this application is the high temperature of operation.

One attempt to overcome this problem in a fuel cell utilizing H_2S is proposed in United States patent[11]. In this is disclosed a fuel cell, in which a redox couple is used as the negative electrolyte which is oxidized at the fuel cell anode and then subjected to reduction outside the electrolytic cell by reaction with H_2S in a remotely located reaction column. The sulfur formed in the reaction column is removed from the electrolyte before the reduced electrolyte is recirculated back into the fuel cell. Consequently, the sulfur is prevented from inactivating the platinum or Raney nickel anode catalyst of the fuel cell. A major drawback of this patent anode catalyst is due to the fact that performance is generally based upon a crystalline structure. In a crystalline structure the catalytically active sites which provide the catalytic effect of such materials result primarily from accidently occurring, surface irregularities which interrupt the periodicity of the crystalline lattice. A few examples of such surface irregularities are dislocation sites, crystal steps, surface impurities and foreign adsorbates.

A major problem with a crystalline structure is that the number of such irregularities forming the catalytically active sites is relatively few and occurs only on the surface of the crystalline lattice[12]. This results in the catalytic material having a density of catalytically active sites which is relatively low. Thus, the catalytic efficiency of the material and the device in which it is utilized is substantially less than that which would be possible if a greater number of catalytically active sites were available for the hydrogen sulfide decomposition or other desired reaction. For these reasons, high catalytic efficiency from a relatively low cost material which is resistant to poisoning and stable in the H_2S cell environment, remain a desired results which must be attained before there will be commercial utilization of this devices.

Catalytic materials must have a high density of active sites and have improved catalytic activity. It is therefore intuitive to consider metal sulfides as alternative potentially useful catalysts. These materials having increased catalytic activity[13] serve to increase operating efficiencies to thereby reduce operating costs and result in more complete removal of hydrogen sulfide contaminants. The catalytic materials are also resistant to poisoning primarily due to their increased density of catalytically active sites and can provide a stable performance over a long period of time[14]. The increased numbers of catalytically active sites also enables the materials to be more resistant to poisoning[3]. This is because with these materials a certain number of catalytically active sites can be sacrificed to the effects of poisonous species while a large number of unpoisoned sites still remain to provide the desired reaction.

Transition metals form good homogeneous or heterogeneous catalysts, for example iron is the catalyst for the Haber process. Vanadium (V) oxide used for the contact process, nickel is used to make margarine and platinum is used to speed up the manufacture of nitric acid[15]. This is because they are able to form numerous oxidation states, and as such, are able to form new compounds during a reaction providing an alternative route with a lower overall activation energy.

The improved catalytic activity can be accomplished by manipulating the local chemical order and hence the local structural order by the incorporation of selected modifier elements into a host matrix to create the desired disordered material[16]. The catalytic materials include at least one element forming a host matrix and at least one modifier element intimately incorporated into the host matrix. The element or elements forming the host matrix include at least one transition element. The host matrix or substrate can also be formed from or with carbon. The host matrix element is selected from the group consisting of C, Co, Mo, Fe, Ru, Ti, W, Cu and Pb and modifying element is incorporated to provide a sulfide or oxide of said host matrix element.

The modifier elements include sulfur or oxygen to form a sulfide, oxide of the transition metal or metals of the host matrix. The incorporation of the modifier element or elements acts to disorder the structure of the material and to create local structural chemical environments which are capable of acting as catalytically active sites for the hydrogen sulfide splitting reaction. The utilization of a disordered structure allows the creation of an increased density and a wide spectrum of catalytically active sites to yield materials

which operate at high catalytic efficiency and are more resistant to poisoning and corrosion[17].

Metal sulfides are inexpensive when compared with precious metals like Pt. Among them, CoS_2, a hexagonal layered n-type semiconductor, is a widely used component in catalysts for a variety of hydrogenation/dehydrogenation and hydrodesulfurization processes in the petroleum industry. Bimetallic sulfides of molybdenum with cobalt, iron, and nickel are each active catalysts for hydrodesulfurization processes[18]. The activity is attributed in part to the presence of CoS_2-like aggregates. An important attribute of these catalysts is sulfur tolerance. Although CoS_2 has not been studied intensively for H_2S decomposition, MoS_2 has been shown to be an effective catalyst for reversible decomposition of H_2S above 600 °C, which indicates that MoS_2 is chemically stable in a high temperature H_2S stream and is not poisoned. The interesting thing about Co is that it is one of the three noteworthy elements in the transition metals family. These elements are iron, cobalt, and nickel, and they are the only elements known to produce a magnetic field.

One major issue that affects the electrolytic cell performance is the thickness of the membrane employed which tends to increase in ohmic resistance as the thickness increases. Therefore, gas permeability testing of electrolytes is critical to the development of ultrathin membranes, where gas leaks can prove catastrophic. Although reducing electrolyte thickness improves the cell performance, there are several practical issues that limit how thin the electrolyte can be made. As the electrolyte thickness is reduced, the

crossover of reactants may increase. This leads to an undesirable parasitic loss which can eventually become so large that further thickness decreases are counter productive[19].

For solid electrolytes, the membrane cannot be made so thin that structural risks of breaking or developing pinholes become an issue. Membrane failure can result in catastrophic mixing of the fuel and cathodic product (hydrogen). Even mechanically sound, pinhole-free electrolytes may fail if the thickness varies considerably across the cell. Thin electrolyte areas may become hot spots that are subject to rapid deterioration and failure. In addition extremely thin electrolytes (solid or liquid) risk electrical shorting, especially when the electrolyte thickness is on the same order of magnitude as the electrode roughness.

Furthermore, part of the electrolyte resistance is associated with the interface between the electrolyte and the electrode. This contact resistance is independent of electrolyte thickness. Also, the ultimate physical limit to solid-electrolyte thickness is given by the electrolyte breakdown properties. This limit is reached when the electrolyte is made so thin that the electric field across the membrane exceeds the dielectric breakdown field for the material[20].

The main research goal was to establish a novel environmentally benign one-step pathway for splitting H_2S electrolytically by using effective MEA to produce hydrogen and liquid sulfur. In order to accomplish this task, we have investigated and developed: (1) a solid acid membrane, (2) fabrication pattern for a MEA and electrolytic cell, and (3) implementation of exit gas control and monitoring systems. In this study, which we

report here, an electrochemical process was applied in the splitting of (100 %) H_2S feed content gas to yield liquid sulfur and hydrogen using a thin membrane MEA developed in our laboratory. This work was successful in achieving the electrochemical splitting of H_2S in an electrochemical system. Furthermore, it provides valuable insight into the nature of electrolyte material by incorporating a series of electrochemical analytical methods and techniques.

2 BACKGROUNDS AND LITERATURE REVIEW

2.1 Electrochemical Cell Description

The beauty of electrochemical devices is that the energy of chemical bonding is converted directly to electrical energy. This is because electrochemical energy conversion is not based on the transfer of heat between a hot and cold reservoir, Carnot limitations are avoided and inherently more efficient processes are, in principle, possible. The basic concept of an electrochemical cell includes a test-bed with porous electrodes in which a solid proton conducting membrane separates the electrodes. A simplified schematic of an electrochemical cell system is shown in Figure 2.1**.** The process consists of passing H_2S gas through the anode chamber to contact a catalytic anode, where electrochemical reaction takes place to produce elemental sulfur, protons and electrons. The protons pass through the membrane from the anode chamber to the cathode chamber, where they react with electrons from the catalytic cathode to produce hydrogen gas. The electrolyte membrane separating both electrodes is impermeable to fuel and product flows, but allows the transport of ionic species between both sides of the cell.

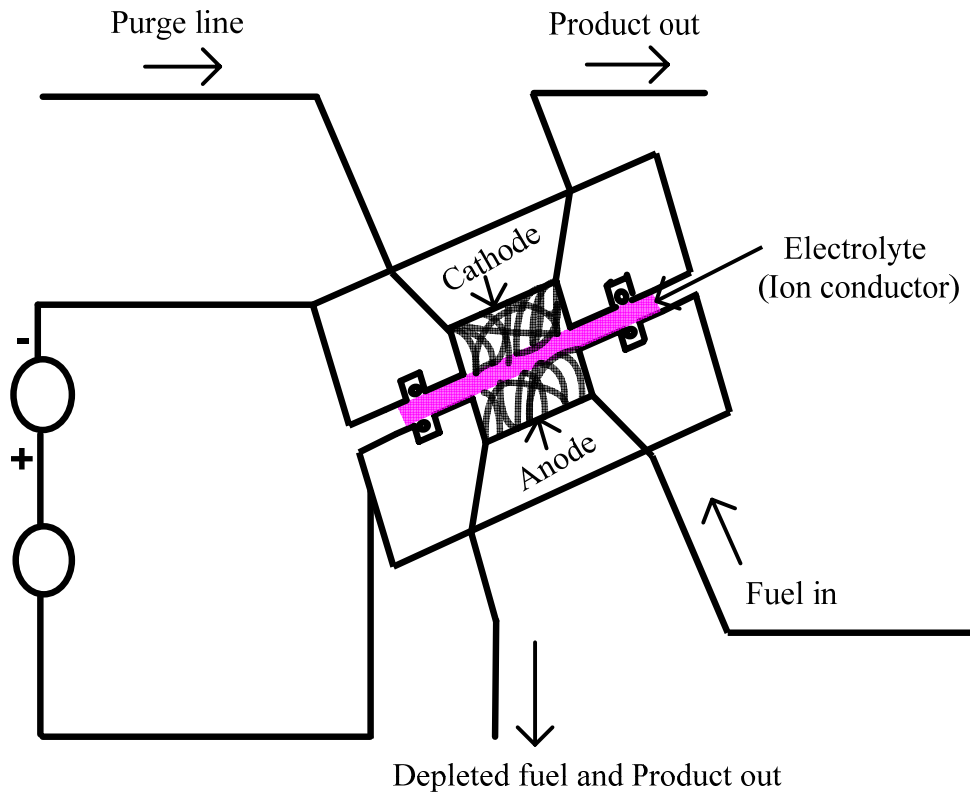

Figure 2.1 Simplified schematic of an electrochemical cell system

2.2 **Essential Anode Properties**

An effective anode material for the H_2S electrolysis has to be electronically conductive, chemically and electrochemically stable, and catalytically active to split H_2S at system operating conditions. It must provide intimate gas contact at the triple phase boundary (TPB) of the fuel-electrolyte-electrode interface and a large interfacial area to maximize electrochemical oxidation rates. Thermal expansivity properties of the anode have to be the same or close to those of other cell components, particularly the cell electrolyte and current collector to avoid different layers from physical damage during system operation. In addition, it has to be chemically inert to other cell constituents as this may lead to drop in system performance.

2.3 **Phases and Ionic Conductivity of $CsHSO_4$**

Solid acids are chemical intermediates between normal salts (a salt that has neither hydrogen (H) nor hydroxyl (OH) in its formula) and normal acids. If a normal acid such as sulfuric acid reacts with a normal salt such as cesium sulfate, the product is a solid acid, cesium hydrogen sulfate (cesium bisulfate):

$$\tfrac{1}{2}CsSO_4\ (\text{salt}) + \tfrac{1}{2}H_2SO_4\ (\text{acid}) \rightarrow CsHSO_4\ (\text{solid acid}) \qquad (2.1)$$

this is the prototypical solid acid used in solid acid fuel cells (SAFCs). Their physical appearances are similar to salts, such as common table salt (NaCl). They show orderly structural arrangements at low temperatures. Nevertheless, at elevated temperatures some solid acids undergo phase transitions to highly disordered structures which cause the conductivity to jump dramatically[21].

Cesium hydrogen sulfate ($CsHSO_4$) belong to a group of crystal $MeXAO_4$, family of compounds (where Me = Cs, Rb; X = H, D; A = S, Se) first observed to undergo a phase transition to a so-called superionic state. They show a high proton conductivity at elevated-temperature phase, usually tagged ‘‘a superprotonic phase’’[22,23,24,25]. In these compounds, tetrahedral XO_4 anions form hydrogen bond networks. The assumption is that the proton transport takes place via the hydrogen bond, acting through by reorientation of the XO_4 tetrahedron. Nevertheless, proton dynamics at molecular is still being investigated. How fast is the reorientation of the HSO_4 ions and how fast is the proton transfer between two neighboring SO_4 tetrahedra? Are the two motions paired or not? In the first stage, hydrogen bond is broken, whereas the hydrogen bond and the chemical bond are exchanged in the second stage. $CsHSO_4$ is one of the most basic

systems among the solid acids and the phase diagrams and crystal structures have been studied extensively[26,27,28,29,30].

The bisulfate (HSO_4^-) group of $CsHSO_4$ forms a tetrahedron with an oxygen atom at each corner and a hydrogen atom sitting on one of the oxygen. At room temperature, all the sulfate groups are frozen into place. When the temperature is raised, disorder takes over and the sulfate groups reorient, changing the positions of the hydrogen atoms as they do so (Figure 2.2). The reorientation takes about 1/6 of a minute to complete. Frequently, a proton from one sulfate oxyanion moves over to the next, with a transfer rate close to 109 Hz[31]. Importantly, these oxyanions rotate almost freely and approximately in every 101 reorientations or so, they are in exactly the right position for a proton transfer to occur[32,33,34]. Subsequently, as the material goes through this superprotonic transition, there is a sudden increase in conductivity of several orders of magnitude. These conductivity values for the acid salts can be matched to those of Nafion and other polymer electrolytes, but at slightly higher temperatures. There are quite a number of such different solid acid compounds exhibiting this kind of behavior.

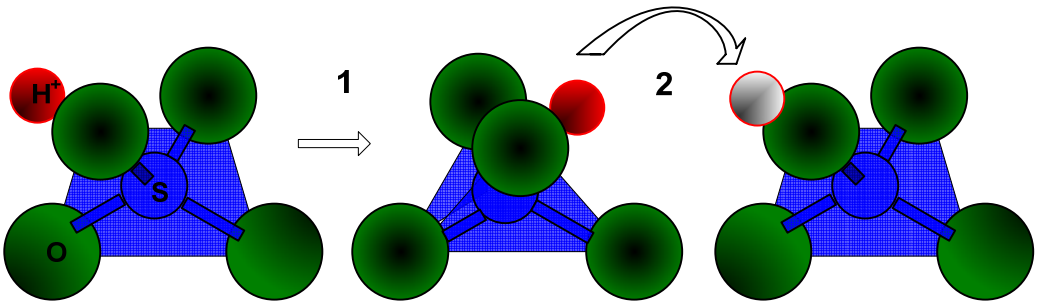

Figure 2.2 Proton conduction mechanism for solid acids ($CsHSO_4$). Protons (H^+) attached to oxyanions are rapidly repositioned (101 Hz) by rotations of the tetrahedra (1). Approximately once every one hundred rotations (109 Hz), the H^+ finds itself in an ideal configuration to hop from one neighboring tetrahedra to another (2)[35].

$CsHSO_4$ exists in 3 phases. Phase III has a hexagonal array of cesium ions stacked along a bent direction at room temperature. Zigzag chains of hydrogen bonded HSO_4^- ions are perpendicular to the loose packed Cs^+ ion plane and ties the Cs^+ ions. The structure is an intermediate between the non-protonic glasrite structure and the ferroelectric CsH_2PO_4 structure with two different types of hydrogen-bonded chains surrounding the Cs^+ cations[35,36,37]. X-ray diffraction shows the phase III structure, which is confirmed by infrared and Raman spectra, particularly the statistical distribution of protons between two potential minima of the OH…O hydrogen bonded chains[38,39 ,40]. There are two first order phase transitions one observed at approximately 318K (III→II) and the other at 417K (II→I). As a result of weakening of the hydrogen bonds and a structural disorder of the anions, the III→II transition has been explained on the basis of spectral vibration analysis where a conversion of infinite chains into cyclic dimers occurs. In the low conductivity phases III and II the number of protons per unit cell is equal to the number of positions for them. Hydrogen bonds link SO_4 tetrahedra so as to form zigzag chains. Hydrogen atoms are localized on the bonds and their mobility is low. For the superionic phase I there is a further weakening of the hydrogen bonds and an increasing level of disorder. There is also evidence of rapid re-orientation of HSO_4^- species and translation disorder of Cs^+ ions. The high proton mobility was observed by H and D NMR, as well as quasi-elastic neutron scattering[41,42,43].

When the temperature is lowered gradually, metastable phases (I→II→III) occur, with long annealing below 280K being required to reach the phase III stage. Essentially, the kinetics is largely influenced by the presence of water traces. Samples prepared by slowly

evaporating solutions of Cs_2SO_4 and H_2SO_4 to produce small crystals (0.5 to 1 mm), do not undergo phase transitions when stored in a sealed container. However complex DSC traces are observed for the temperature range 315-380K. According to the study, this is supported by the measured enthalpy values (ΔH) for the III→II transition which varies reversibly between 4.8 and 14.4 kJ/mol being dependant on the concentration of the defect, while the II→I (II↔I) phase transition ΔH value yields approximately 14.4 or 29.2 kJ/mol. The stretching intensity of the S-O and S-OH bands is directly affected by the grinding force during the sample preparation and is not influenced by the time factor. Weak and strongly ground samples show different spectra. The Raman spectrum shows typical cyclic dimer occurrence as in phases II and III. Thus, $CsHSO_4$ at room temperature can be structurally modified by mechanical treatment which converts the chains of HSO_4^- ions into cyclic dimers. The applied pressure also referred to as the mechanical treatment, is responsible for the chain/dimer ratio[44,45 ,46,47].

$CsHSO_4$ conductivity is influenced by two major factors: how many carriers are available to transport charge and the mobility of those carriers within the material. Therefore, conductivity is determined by carrier concentration and carrier mobility. Charge transport in the $CsHSO_4$ crystalline ionic conductor is accomplished by mobile ions (H^+) protons which hop from position to position within the lattice. The hopping process only occurs when lattice defects such as vacancies or interstitials are present. Ion mobility for the material is dependent on the rate at which ions can hop from position to position within the lattice. The hopping rate is exponentially activated[48,49]. However, an activation barrier impedes the motion of the atoms as it hops between positions. We might associate this

energy barrier with the displacements that the atom causes as it squeezes through the crystal lattice between lattice sites[50]. Thus, carrier concentration in a crystalline electrolyte is controlled by the density of the mobile defect species[50]. Most crystalline materials conduct via a vacancy mechanism. These vacancies are intentionally introduced into the lattice by doping or by mechanical pulverization such as ball milling[51].

Solid electrolytes are preferable to liquid due to a number of reasons. Most importantly, the temperature ranges of operation for such electrolytes are either very high (above 600 °C) or rather low (below 90 °C)[52]. The high-temperature electrolytes are not currently practical in mobile applications such as automobiles-one of the major potential markets for fuel cells-due to start-up and other limitations[53]. Low-temperature fuel cells, on the other hand, are not as flexible in the fuel they can use, and much of the energy they release is needed just to maintain operation. State of the art polymer electrolyte membranes composed of a sulfonated fluorocarbon, also known as Nafion®, have high current and power densities, but tend to lose integrity and proton conductivity as a result of dehydration of the membrane at temperatures above 90 ^{o}C. Another limitation of Nafion® in the application under study is that the anode product is solid sulfur, which accumulates at the anode surface, and thereby reduces the activity of the system with time on stream.

Although these classes of solid electrolytes are known to be soluble in water, they do not pose any problem to our application at 150 ^{o}C because steam instead of water exists at this temperature and does not affect the membrane performance. At the transition phase

temperature of $CsHSO_4$, sulfur is a low viscous liquid and can flow out of the electrolytic cell quickly and easily (Figure 2.3).

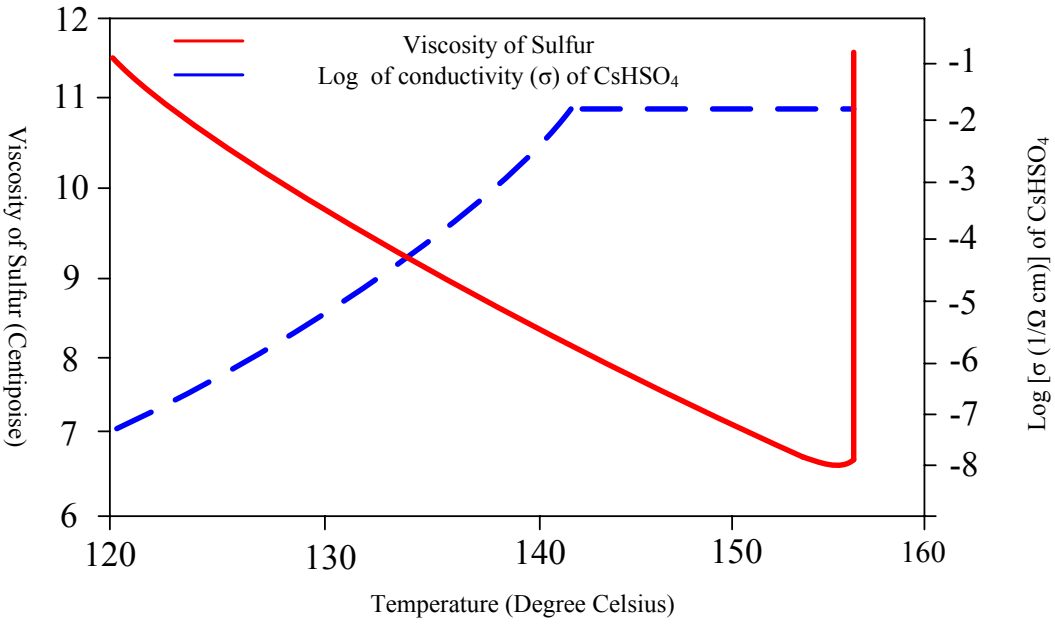

Figure 2.3 Viscosity of sulfur, conductivity of $CsHSO_4$ vs. Temperature[54].

Thermomechanical and electrochemical studies conducted previously show that this material is stable for more than 85h of continuous voltage measurements in an oxygen atmosphere and that the ionic transference number is~1 Based on extensive studies of the material, it is clear that the mobile species are protons[53]. But there are still some issues to be resolved. A major concern with this SAE is the possibility that performance will be lost gradually through the depletion of the sulfur in the $CsHSO_4$ electrolyte since the compound can react with molecular hydrogen to form hydrogen sulfide. A thorough investigation of the decomposition and behaviors at transition temperatures of $CsHSO_4$ could provide valuable insight into the thermochemical requirements necessary to create a stable solid acid electrolyte for electrolytic cell applications. For complete splitting of H_2S, the electrolyte must demonstrate high ionic conductivity: that is, the entirety of the

current should be carried by ions rather than electronic species and the membrane must be impermeable to H_2S.

2.4 Previous Work on H_2S Splitting

The ability to electrochemically split H_2S in a fuel cell was carried out in the late 1980s[55]. Subsequently, this led to the study of alternative electrolytes and anode electrocatalysts for H_2S splitting in electrolytic cell[12]. O^{2-} conducting yttria-stabilized zirconia (YSZ) electrolytes were the most commonly used electrolytes in H_2S splitting cell. Recently, ceria-based O^{2-} conducting electrolytes[56,57] and H^+ conducting electrolytes have proven to have some new advantages for H_2S electrolysis operated at temperatures below 700 °C. Active anode materials ($Li_2S/CoS_{1.035}$ and WS_2) were found to enhance H_2S electrolytic cell performance tremendously. In order to be a suitable candidate for the electrochemical splitting of H_2S, an anode material must possess good electrical conductivity and sulfur tolerance at high temperatures, in addition to good catalytic activity. Pt anode catalysts have good catalytic activity, but degrade over time in H_2S streams. Moreover; most metals and metal oxides are severely corroded by H_2S at elevated temperatures.

2.5 Gas Permeability

High proton migration which subsequently leads to high conductivity of $CsHSO_4$ at elevated temperature is eliminated if the cell electrolyte exhibits any type of permeability. Permeability measures the ease with which gases move through a material. Even low porous materials can experience permeability if most of their pores are open or connected. In this work it was found, via electrochemical impedance spectroscopy that by

reducing the electrolyte membrane thickness to one-fifth improved the cell performance by over 30 %. Gas permeability testing of these ultrathin membranes whose thicknesses range from (0.1 -0.02 cm) is critical to the development of high performance electrolytes, where gas leaks can prove catastrophic. Although reducing electrolyte thickness improves the cell performance, there are several practical issues that limit how thin the electrolyte can be made. As the electrolyte thickness is reduced, the crossover of reactants may increase. This leads to an undesirable parasitic loss which can eventually become so large that further thickness decreases are counterproductive[19]. For solid electrolytes, the membrane cannot be made so thin that physical breaking or developing pinholes become an issue. Membrane failure can result in sudden and violent mixing of the fuel and cathodic product (hydrogen). Even mechanically sound, pinhole-free electrolytes may fail if the thickness varies considerably across the cell. Thin electrolyte areas may be subjected to rapid deterioration and failure. In addition, extremely thin electrolytes (solid or liquid) risk electrical shorting, especially when the electrolyte thickness is on the same order of magnitude as the electrode roughness. Furthermore, part of the electrolyte resistance is associated with the interface between the electrolyte and the electrode. This contact resistance is independent of electrolyte thickness. Also, the ultimate physical limit to solid-electrolyte thickness is determined by the electrolyte breakdown properties. This limit is reached when the electrolyte is made so thin that the electric field across the membrane exceeds the dielectric breakdown field for the material. Our system can be described by Eqn. 2.2. Permeability (K) is determined by measuring the volume of gas (Δ V) that passes through a sample in a given period of time (Δ t) when driven by a given pressure drop (Δ p = p_1-p_2):

$$K = \frac{I}{\Delta p} - \frac{\Delta V}{\Delta t}\frac{2p_2}{(p_1 + p_2)\Delta p} \qquad (2.2)$$

Where I = Dl is a constant with a diffusion coefficient, D, l is the thickness per area of the membrane, and p_1 and p_2 are the pressures in the delivery and receiving compartments of permeation cell respectively[51].

It was found, via electrochemical impedance spectroscopy, that by reducing the electrolyte membrane thickness by one-fifth improved the cell performance by over 30 %. In this investigation, possible H_2S gas permeation through various thicknesses of $CsHSO_4$ ulta-thin membranes at 150 ^oC is reported for the first time. Herein, we will show that $CsHSO_4$ membrane is impermeable to H_2S gas, with innocuous effect, over prolonged periods of operation. Previous study has shown that at the superprotonic transition phase of $CsHSO_4$ (140-160 ^oC) permeance to hydrogen gas decreased[58]. However, analyses conducted by a material science group at California Institute of Technology report that the low open circuit voltage (OCV) observed using $CsHSO_4$ electrolytes could be attributed to hydrogen permeability[53]. Herein we will show that $CsHSO_4$ membrane is impermeable to H_2S gas, with innocuous effect, over prolonged periods of operation.

3 THEORY

3.1 Physical Properties and Sources of H_2S

H_2S information was obtained from Specialty Gases of America, purity = 99.5 %, Mwt: 34.08, specific volume: 1.23 ft^3/lb, labels: *P, *F: *P = poison-inhalation hazard, *F = flammable gas, ΔfH^0gas, -20.5 kJ/mol (exothermic), autoignition temperature, 500 ^oF or 260 ^oC, density, 1.363 g/L. Hydrogen sulfide, H_2S, at room temperature is a colorless, extremely poisonous vapor (MSDS data: IHL-HMN LC50 800 ppm 5 min). Highly flammable under normal conditions - hydrogen sulfide readily forms explosive mixtures with air (4 % lower explosion limit, LEL, H_2S). It occurs naturally in crude petroleum, natural gas, volcanic gases and hot springs at concentrations ranging from a few ppm to 50 % or higher. It also can result from bacterial breakdown of organic matter including human and animal wastes. Other source includes, industrial activities, such as food processing, coal processing in the integrated gasification combined cycle (IGCC) power plants, desulfurization of hydrocarbon resources, coke ovens, Kraft paper mills, tanneries, petroleum refineries and many other such processes.

3.2 H_2S Electrochemical Splitting

The fundamental principle underlying the splitting of H_2S electrochemically consist of having an anode and cathode compartments in which a solid proton conducting membrane separates an anode chamber from a cathode chamber (Figure 3.1). The process

consists of passing H_2S containing gas through the anode chamber to contact a catalytic anode, where reaction Eqn. 3.1 takes place to produce elemental sulfur, protons and electrons.

$$H_2S \rightarrow \frac{1}{2}S_2 + 2H^+ + 2e^- \qquad E^o\,(423\ K) = 0.19 \qquad (3.1)$$

The protons pass through the membrane from the anode chamber to the cathode chamber, where reaction (Eqn. 3.2) occurs with electrons from the catalytic cathode to produce hydrogen gas.

$$2H^+ + 2e^- \rightarrow H_2 \qquad (3.2)$$

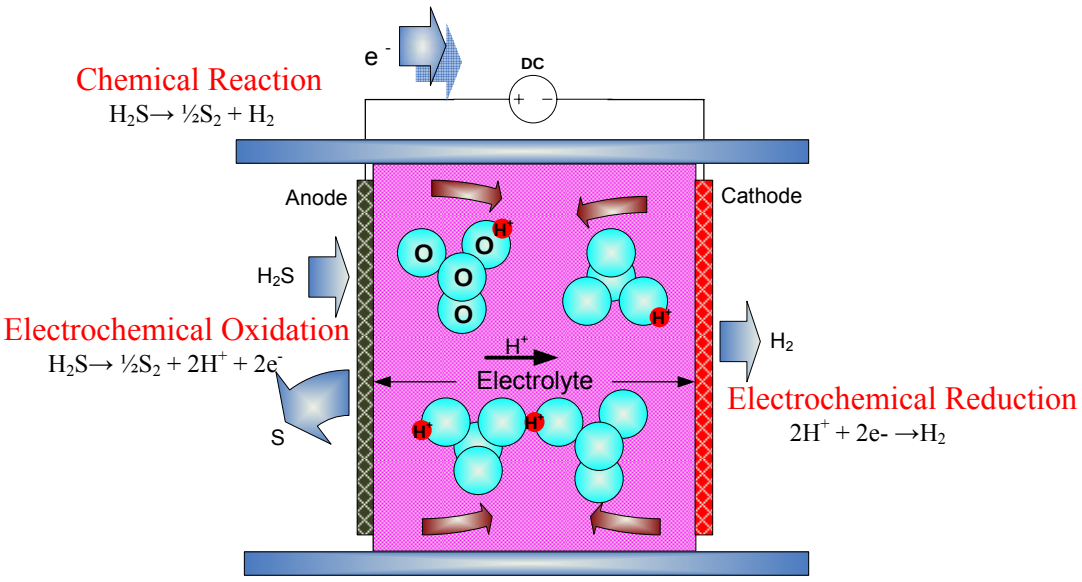

Figure 3.1 Basic operating principle of H_2S electrolysis

The chemical reaction taken place is given by reaction (Eqn. 3.3)

$$H_2S \rightarrow \frac{1}{2}\,S_2 + H_2 \qquad (3.3)$$

3.3 **Electrochemical Thermodynamics**

Any electrochemical reaction involves the transfer of electrons between an electrode surface and a chemical species adjacent to the electrode surface. Thermodynamically favorable electron transfer processes is harnessed in order to extract the electrical energy requirement for the oxidation process. To carry out a thermodynamic analysis, it is pertinent to relate thermodynamic (reversible) potential to state variables. For a reasonable analysis to be performed, it is common to assume electrochemical operation occurs at constant temperature and pressure. The choice of fuel (H_2S) makes it easy to define the electrochemical processes occurring within the cell as well as the reaction free energies associated with the components. Furthermore, if a closed system operating under these conditions is considered, then a thermodynamic analysis can be carried. This implies that the electrical work output by a system can be related to its total change in Gibbs free energy.

$$\Delta G = -\omega_{electrical} \tag{3.4}$$

A well known expression for maximum amount of electrical energy which can be deliverd by a system is (Eqn. 3.5)[48]:

$$\omega_{electrical} = nFE \tag{3.5}$$

Where $\omega_{electrical}$ is the maximum electrical work, n is the number of electrons (per ionic species) taking part in the reaction, F is Faraday's constant (96,487 A sec/equiv), and E is the reversible cell potential. The latter is the necessary driving force for any electrochemical process to occur. Combining these two expressions (Eqns. 3.4, 3.5),

yields the key equation relating electrical work to traditional thermodynamics (Eqn. 3.6). Eqn. 3.6 statement represents the possible maximum predicted electrical work output.

$$\Delta G = - nFE \tag{3.6}$$

However, since this analysis is for a reversible (ideal) system, the electrical work in a real electrochemical cell device will be smaller. Eqn. 3.6 is the key equation relating electrical potential to the traditional thermodynamic framework. The free energy of reaction can be calculated from free energy of formation $\Delta G_{i,f}$ data by

$$\Delta G = \sum_i si \Delta G_{i,f} \tag{3.7}$$

where s_i is the stoichiometric coefficient (positive for products and negative for reactants[48]).

3.4 **Nernst Equation**

The ideal standard potential for an electrochemical reaction may be obtained either from tabulated data or by using standard Gibbs-free energy data in Eqn. 3.6. The Nernst equation is given by Eqn. 3.8 which relates concentration changes to changes in reversible potential[59].

$$E = E^O - \frac{RT}{nF} 1n\left(\prod a_i^{vi}\right) \tag{3.8}$$

Here R is the gas constant (8.314 J/mol K), T is the absolute temperature in K, a_i is the activity and vi is the stoichiometric coefficient of electro-active species i. Ideal gas behavior is assumed, where the activity of gaseous species equals their partial pressure as in (Eqn. 3.9):

$$E = E^O - \frac{RT}{nF} 1n\left(\prod p_i^{vi}\right) \tag{3.9}$$

where *Pi* is the partial pressure of species i in the gas phase. Since sulfur is the product in the electrochemical splitting of H_2S by (Eqn. 3.3) the Nernst equation takes the form:

$$E = E^O - \frac{RT}{2F} 1n\left(\prod \frac{p_S^{1/2} p_H^{2}}{p_{H_2S}}\right) \qquad E^O(423\text{ K}) = 0.19 \tag{3.10}$$

It is clear from the Nernst equation that a set of concentrations exists that will result in a reversible potential of zero. This state corresponds to the thermodynamic equilibrium and the equilibrium constant K can be obtained from (Eqn. 3.11).

$$E = E^O - \frac{RT}{nF} 1nK$$

$$= 0$$

Therefore,

$$E^O = \frac{RT}{nF} 1nK \tag{3.11}$$

3.5 **Cell Performance**

There several factors that contribute to irreversible losses associated with electrochemical performance commonly referred to as polarization losses. Such factors include: activation losses (η_{act}) due to kinetics, ohmic losses (η_{ohmic}) from ionic and electronic resistance, and concentration losses (η_{conc}) due to mass transport[60].

3.5.1 **Activation Polarization (η_{act})**

Activation polarization represents the amount of voltage sacrificed (lost) to overcome the activation barrier associated with the electrochemical reaction. This usually occurs as a result of slow kinetics which impedes the rate of electrochemical reactions at the electrodes. Consequently, activation polarization is a strong function of reaction rates, i.e., oxidations or reductions at either the cell anode or cathode.

3.5.2 **Potential and Rate: Butler-Volmer Equation**

The Butler-Volmer equation basically states that the current produced by an electrochemical reaction increases exponentially with activation overvoltage (Eqn. 3.12)

$$j = j_0\left(e^{\alpha nF\eta/(RT)} - e^{-(1-\alpha)nF\eta/(RT)}\right) \tag{3.12}$$

where j is the current density, j_0 is the exchange current density for the reaction and represents the state of dynamic equilibrium at which the net reaction rate is zero for both the forward and reverse reactions, α is the transfer coefficient expresses how the change in the electrical potential across the reaction interface changes the size of the forward versus reverse activation barrier (values lies between 0 and 1), η is the activation polarization, and n is the number of electrons transferred per reaction.

Kinetics can be simplified with two useful approximations to the Butler-Volmer equation when the activation overvoltage (η_{act}) is either very small or very large:

a. When η_{act} is very small. For small η_{act} (less than about 15 mV at room temperature), a taylor series expansion of the exponential terms gives a linear relationship of current and overvoltage (Eqn. 3.13).

$$j = j_0 \frac{nF\eta_{act}}{RT} \tag{3.13}$$

b. When η_{act} is large (greater than 50-100 mV at room temperature), the second exponential in the Butler-Volmer equation becomes negligible. In other words, the forward–reaction direction dominates, corresponding to a completely irreversible reaction process. Simplifying and solving the equation for η_{act}, yields the well known Tafel equation[59] (Eqn. 3.14).

$$\eta_{act} = -\frac{RT}{\alpha nF} 1nj_0 + \frac{RT}{\alpha nF} 1nj \tag{3.14}$$

In generalized form, this equation becomes

$$\eta_{act} = a + b \log j \tag{3.15}$$

where b is the Tafel slope.

A plot of η_{act} versus 1n j is a straight line from which the values of j_0 and α are obtained. This proves more useful in most discussions.

3.5.3 **Concentration Losses (η_{conc})**

Overpotential associated with mass transport is called concentration overpotential. This form of overpotential (η_{conc}) is caused by mass transport limitations occurring as a result of reactant depletion (or product accumulation) within the catalyst layer which adversely affect performance. It is also caused by inadequate flow of reactants to or removal of products from the cell electrode. Gas transport within the electrodes is dominated by diffusion because of the tortuous, sheltering geometry of the electrodes which insulates

gas molecules from the convective forces present in the flow channels[50]. The 3 major transport processes are:

a. diffusion of fuel and product flows in the bulk,

b. diffusion of fuel and products in the electrode, and

c. proton diffusion in the electrolyte.

The first two types of diffusion, which are not covered by this study, can be modeled by Fick's law of diffusion; listed below are the two effects these transport processes have on the performance of the system:

a. Nernstian losses: The reversible cell voltage will increase as predicted by the Nernst equation since the reactant concentration at the catalyst layer is decreased relative to the bulk concentration and the product concentration at the catalyst layer is increased relative to the bulk concentration.

b. Reaction losses: The reaction rate (activation) losses will be increased because the reactant concentration at the catalyst layer is decreased relative to the bulk concentration and the product concentration at the catalyst layer is increased relative to the bulk concentration.

3.5.4 **Ohmic Losses (η_{Ohmic})**

These are caused by resistance to flow of charged species (electrons and ions) at cell electrodes and electrolytes respectively. It results primarily from the concentration cell that is established between the bulk electrolyte and the electrode surface. At the cell anode, sulfur poisoning tends to increase the polarization resistance which physically affects the anode structure bringing about de-lamination of the cell electrode. As a result,

an insulation layer is formed which inhibits the transport of ions and electrons through the electrolyte and the electrode respectively causing the cell performance to drop.

Ohmic losses obey Ohms law:

$$\eta_{Ohmic} = IR_{Total} \tag{3.16}$$

I is the current drawn from the cell and R_{Total} *is* the total cell resistance; this includes contributions from the electrolyte and the whole of the electrochemical system. The intrinsic resistance from the electrolyte is given by Eqn. 3.17.

$$R_{electrolyte} = \frac{\rho_{electrolyte} x}{A} \tag{3.17}$$

where $\rho_{electrolyte}$ is the ionic resistance of the electrolyte, x is the electrolyte thickness, and A is the electrolyte area. Impedance spectroscopy or other available methods are usually used to determine cell resistance due to interface contacts and lead wires.

3.6 **Physical Meaning of Conductivity**

Conductivity quantifies the ability of a material to permit the flow of charge when driven by an electric field. In other words, conductivity (σ) is a measure of how well a material accommodates charge transport. A material conductivity is influenced by two major factors: how many carriers are available to transport charge and the mobility of those carriers within the material. The following equation defines σ in those terms:

$$\sigma_i = (|z_i| F) c_i u_i \tag{3.18}$$

where c_i represents the molar concentration of charge carriers (how many moles of carrier is available per unit volume) and u_i is the mobility of charge carriers within the material. The quantity $|z_i| F$ is necessary to convert charge carrier concentration from

units of moles to units of coulombs. Here, z_i is the charge number for the carrier, the absolute-value function ensures that conductivity is always a positive number, and F is Faraday's constant.

A material's conductivity is therefore determined by carrier concentration c_i and carrier mobility u_i. These properties are in turn set by the structure and conduction mechanisms within the material. Up to this point, the charge transport equations apply equally well to both electronic and ionic conduction. However, their path will diverge because electronic and ionic conduction mechanisms are vastly different hence; the electronic and ionic conductivities are also quite different.

3.7 **Ionic Conductivity in a Crystalline Solid Electrolyte**

In contrast to electron transport in metals where valence electrons detach from immobile metal atom cores and move freely in response to an applied field, charge transport in crystalline ionic conductors is accomplished by mobile anions which hop from position to position within the lattice. The hopping process only occurs when lattice defects such as vacancies or interstitials are present. As a result, conduction hoping process leads to a very different expression for mobility as compared to a metallic electron conductor. Ion mobility for the material is dependent on the rate at which ions can hop from position to position within the lattice. The hopping rate is exponentially activated.

A calculation of the net flux (net movement) of atoms in an imaginary plane A which lies between two real atomic planes in the material is shown below. The assumption made is that the flux of grey atoms hopping in the forward direction (and therefore through plane

A) is simply determined by the number (concentration) of grey atoms available to hop times the hopping rate[49,59]:

$$J_A^{+} = \frac{1}{2} v c_1 \Delta x \tag{3.19}$$

where J_A^{+} is the forward flux through plane A, v is the hopping rate, c_1 is the volume concentration (mol/cm^3) of grey atoms in plane 1, Δx is the atomic spacing required to convert volume concentration to planar concentration (mol/cm^2), and the $\frac{1}{2}$ accounts for the fact that on average only half of the jumps will be forward jumps. Similarly, the flux of grey atoms hopping from plane 2 backward through plane A will be given by

$$J_A^{-} = \frac{1}{2} v c_2 \Delta x \tag{3.20}$$

where J_A^- is the backward flux through plane A and c_2 is the volume concentration (mol/cm^3) of grey atoms in plane 2. The flux of grey atoms across plane A is therefore given by the difference between the forward and backward fluxes through plane A:

$$J_{net} = \frac{1}{2} v \Delta x \left(c_2 - c_1\right) \tag{3.21}$$

A familiar expression for diffusion is given by Fick's first law, $J = -D\left(dc/dx\right)$. Eqn. 3.21 can be expressed in terms of a concentration gradient as

$$J_{net} = -\frac{1}{2}\left(\Delta x\right)^2 \frac{\left(c_2 - c_1\right)}{\Delta x} \tag{3.22}$$

$$= -\frac{1}{2} v \left(\Delta x\right)^2 \frac{\Delta c}{\Delta x}$$

$$= -\frac{1}{2} v \left(\Delta x\right)^2 \frac{dc}{dx} \qquad \text{(for small } x\text{)} \tag{3.23}$$

Comparison with the Fick's first law of diffusion equation $J = -D(dc/dx)$ allows us to identify what we call the diffusivity as

$$D = \frac{1}{2} v(\Delta x)^2 \tag{3.24}$$

The above expression illustrates that diffusivity is a function of the intrinsic hopping rate for atoms in the material and the atomic length scale associated with the material. However, an activation barrier impedes the motion of the atoms as it hops between positions. We might associate this energy barrier with the displacements that the atom causes as it squeezes through the crystal lattice between lattice sites. We can write the hopping rate as

$$v = v_0 e^{-\Delta Gact/(RT)} \tag{3.25}$$

Where ΔG_{act} the activation barrier for the hopping process and v_0 is the jump attempt frequency. Based on this activation model for diffusion, we can then write a complex expression for the diffusivity as

$$D = \frac{1}{2}(\Delta x)^2 v_0 e^{-\Delta Gact/(RT)} \tag{3.26}$$

Or, lumping all the preexponential constants into a D_0 term,

$$D = D_0 e^{-\Delta Gact/(RT)} \tag{3.27}$$

Where D_0 is a constant reflecting the attempt frequency of the hopping process, R is the gas constant, and T is the temperature (K). The overall mobility of ions in the solid electrolyte is then given by

$$u = \frac{|zi|FD}{RT} \tag{3.28}$$

Where $|zi|$ is the charge number on the ion, F is the Faraday's constant, R is the gas constant, and T is the temperature (K).

Inserting the expression for ion mobility given by (Eqn. 3.28) into equation for conductivity (Eqn. 3.18) yields

$$\sigma = \frac{c(ziF)^2 D}{RT} \tag{3.29}$$

Combining Eqns. 3.27, 3.28 and 3.29 in what is known as the Einstein-Smoluchowski equation we obtain an expression for ionic conductivity of SAE in the form of an Arrhenius relationship (Eqn. 3.30)

$$\sigma(T) = e.c.u = A_O e^{(-\Delta Ha / KpT)} \tag{3.30}$$

where $A_O = \frac{c(ziF)^2 D_O}{RT}$ is the preexponential or the frequency factor, K is the Boltzmann constant, H_a is the migration enthalpy.

Thus, carrier concentration in a crystalline electrolyte is controlled by the density of the mobile defect species. Most crystalline electrolytes conduct via a vacancy mechanism. These vacancies are intentionally introduced into the lattice by dopping or by mechanical pulverization.

3.8 **Electrochemical Impedance Spectroscopy (EIS) Characterization**

Impedance measurements are usually made by applying a small sinusoidal voltage perturbation, $V(t) = V_0 \cos(wt)$, and monitoring the system's resultant current response,

$i(t) = i_0 \cos(wt - \phi)$. In these expressions, $V(t)$ and $i(t)$ are the potential and current at time t, V_0 and i_0 are the amplitudes of the voltage and current signals, and w is the radial frequency. The relationship between radial frequency w (expressed in radians per second) and frequency f (expressed in hertz) is[61]

$$w = 2\pi f \tag{3.31}$$

In general, the current response of a system may be shifted in phase compared to the voltage perturbation. This phase shift effect is described by ϕ. A graphical representation of the relationship between a sinusoidal voltage perturbation and phase-shifted current response is shown in Figure 3.2 (for a linear system).

Impedance is given by the ratio between a time-dependent voltage and a time-dependent current:

$$Z = \frac{V(t)}{i(t)} \tag{3.32}$$

Following Eqn. 3.32 we can write the sinusoidal impedance response of a system as

$$Z = \frac{V_0 \cos(wt)}{i_0 \cos(wt - \phi)} = Z_0 \frac{\cos(wt)}{\cos(wt - \phi)} \tag{3.33}$$

Alternatively, complex notation can be used to write the impedance response of a system in terms of a real and imaginary component:

$$Z = \frac{V_0 \cos(wt)}{i_0 e^{(jwt - j\phi)}} = Z_0 e^{j\phi} = Z_0 (\cos\phi + j \sin\phi) \tag{3.34}$$

The impedance of a system can therefore be expressed in terms of an impedance magnitude Z_0 and a phase shift ϕ, or in terms of a real component ($Z_{real} = Z_0 \cos\phi$) and

an imaginary number ($Z_{imag} = Z_0 \sin \phi j$). The expression j represents the imaginary number ($j = \sqrt{-1}$), not the current density used later in the text.

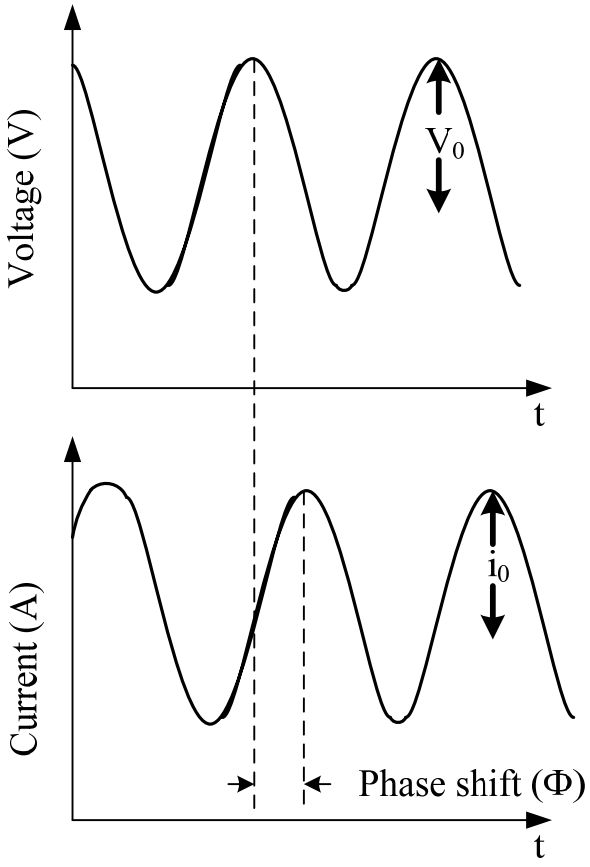

Figure 3.2 A sinusoidal voltage perturbation/ resulting sinusoidal current response. The current response will possess the same period (frequency) as the voltage perturbation but will generally be phase shifted by an amount Φ.

Normally, impedance data are plotted in terms of the real and imaginary components of impedance (Z_{real} on the x axis and $-Z_{imag}$ on the y axis). Such graphical representations of impedance data are known as Nyquist plots. Because impedance measurements are made at dozens or even hundreds of different frequencies, Nyquist plots generally summarize the impedance behavior of a system over many orders of magnitude in frequency.

4 EXPERIMENTAL EQUIPMENT AND TECHNIQUES

4.1 Introduction

Selecting the most efficient approach from various different routes to make the same product is not always simple. Inthis study, our most successful anode material, p-dichlorobenzene/ $CsHSO_4$/ ruthenium (IV) oxide/cobalt sulfide and 200 μm modified electrolyte disc is used as an illustration. Our approach is to develop a stable solid electrolyte first, and then identify which anode materials improve ionic and electronic properties.

4.2 Experimental Apparatus

The experimental apparatus used in splitting (100 %) H_2S content gas is illustrated in Figure 4.1. The electrolytic splitting of H_2S in a solid acid electrochemical cell was performed in laboratory constructed equipment consisting of: (a) a gas handling system; (b) an electrolysis cell; and (c) an exit gas control and monitoring system, as described here. Electrolytic cell, with a 1.25 cm electrolyte disc is operational. It operates at 150 ^oC with gaseous H_2S and liquid sulfur in the anode compartment and hydrogen gas in the cathode compartment. The cell has thick walls to accommodate pipe fittings. The housing is chrome plated (316) stainless steel. Aflas o-rings and gaskets are employed to resist the corrosive anode contents. The total exposed surface on each side of the electrolyte pellet is 0.4 cm^2. The active area is less because of electrode coverage. The

pellet thickness is 200 μm. The high area to thickness ratio implies a small ohmic resistance. The sulfur compartments are modeled after the sulfur compartments in sodium sulfur batteries which are filled with carbon felt. This carbon felt, which is in direct contact with the electrolyte, conducts electrons from the electrolyte in the anode compartment. The same material is being used in the cathode compartment. Apparatus for monitoring and control of the hydrogen sulfide sulfur and hydrogen flows have been designed and tested. A liquid sulfur collection system was fabricated and a water displacement apparatus for the hydrogen produced was utilized. Hydrogen sulfide is delivered to the anode compartment of the electrolytic cell via (316) stainless steel tubing regulated by a pressure regulator on the tank, monitored by a flow meter and controlled by a micrometering valve in the line. The pressure is continuously monitored.

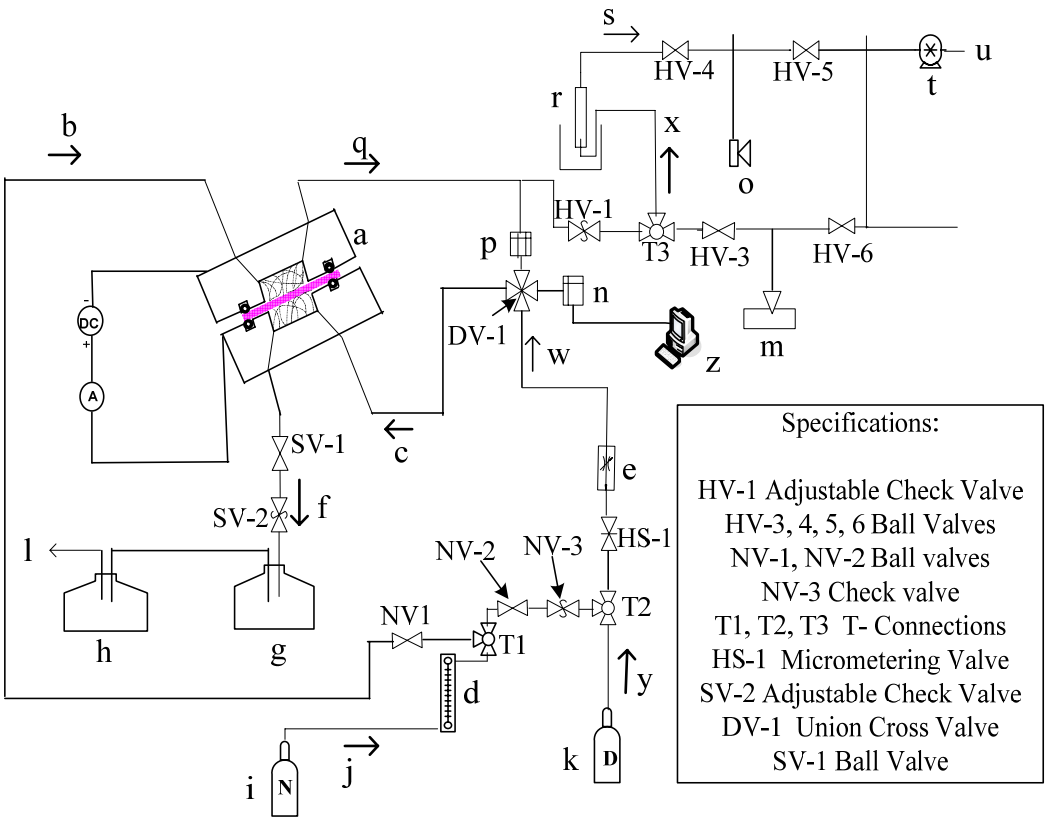

Figure 4.1 Schematic of electrolytic splitting cell. (a) electrolyzer; (b) cathode purge line; (c) H_2S line; (d) flowmeter 1; (e) flowmeter 2; (f) sulfur line; (g) sulfur collection apparatus; (h) NaOH solution; (i) nitrogen tank; (j) anode purge line; (k) H_2S tank; (l) to vent; (m) infrared cell; (n) pressure transducer; (o) ejector for GC analysis; (p) pressure differential; (q) cathode product outlet; (r) water displacement apparatus; (s) hydrogen gas; (t) vacuum pump; (u) to vent; (v) H_2S inlet; (w) cathode product; (y) H_2S line; (z) computer interfaced LabView.

The differential pressure of the hydrogen exiting the cell and the hydrogen sulfide entering is measured directly for greatest sensitivity. Our intentions are to make the electrolyte disc as thin as possible to maximize conductance. This requires minimizing the pressure difference they must withstand. Hence this difference is carefully measured and kept small. There are nitrogen purge lines for purging both compartments before and after experiments. The cell was sealed using hermetic sealing at all joints and insulation of electrical components was ensured by using an aflas gasket. The velocity of the H_2S

gas stream was controlled using a micrometering valve (Upchurch). Two pressure transducers are used to monitor the pressures in the anode and cathode compartments for greatest sensitivity and the pressures in each half cell were maintained using two back pressure micrometering valves (Upchurch). The pressure was kept constant throughout the duration of the experiment. Before each experiment the hermetic sealing of the cell was confirmed at room temperature and then at the operating temperature, using nitrogen as the test gas.

4.3 **Preparation of Anode Electrocatalyst**

A mixture of $CsHSO_4$, p-dichlorobenzene, CoS_2, and RuO_2 was used to prepare the anode electrocatalyst. Throughout the experiment, Pt black served as the cathode electrocatalyst. The ratio of the respective components was 1:0.5:3:3 by mass. Compressed carbon felt was used for both anode and cathode electrode with a specific mass of 0.00136 g/m^2 ; this also served as current collectors for both electrodes and a source of mechanical strength for the thin electrolyte disc.

The anode catalyst materials, with the ratios specified, are mixed for several hours in a high energy planetary ball mill. To get a uniform mixture, ethanol is added to the combination to make a suspension that is mixed thoroughly for 3 h. Then ethanol will be allowed to evaporate slowly to leave the mixture as powders. The powdery mixture are heat-treated in N_2 atmosphere at 150 ^oC for 2 h and allowed to cool under N_2 to room temperature in an autosorb apparatus in the outgassing station. The resulting powders were then used to prepare the anode catalysts. The specific surface area determinations of

the catalysts were carried out with Autosorb-1 software using a BET Multipoint approach.

4.4 **Cell Fabrications**

$CsHSO_4$-based MEAs were fabricated by pressing in an evacuated die set. An electrocatalyst layer, an electrolyte layer, and a second gas diffusion layer with electrocatalyst layer were sequentially added to a carbon felt gas diffusion electrode. After addition of each layer, the structure was uniaxially pressed to promote adhesion between layers, forming the final layer of the sandwiched structure, shown in Figure 4.2. The electrolyte thickness was calculated from the weight of $CsHSO_4$ incorporated into the electrolyte. Prior to the electrolysis run, the p-dichlorobenzene was removed under gentle heating (12 h) at 70 ^oC in inert atmosphere, followed by a 2 ^oC/min ramp to 174 ^oC, the boiling point of p-dichlorobenzene, leaving behind open porosity in the electrocatalyst layers. Porous carbon felt, with average pore size and porosity of 35 μm and 38-40 %, respectively, served as a current collector/gas-diffusion electrode and also served to provide mechanical support for the thin membrane disc.

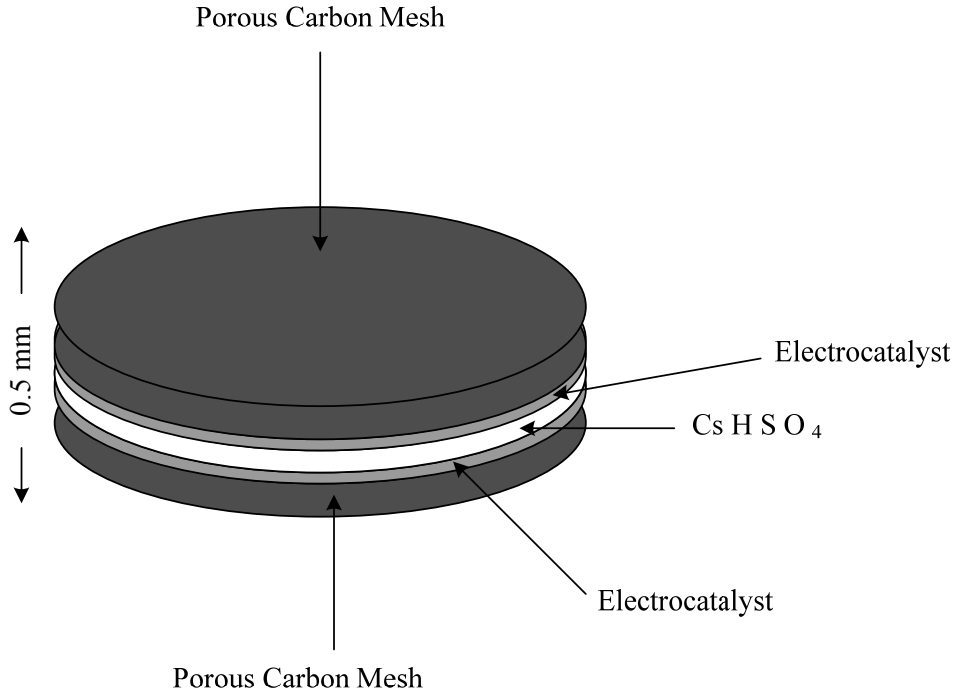

Figure 4.2 Schematic diagram of a fabricated cell ($CsHSO_4$-based MEA).

4.5 **Permeability of H_2S on $CsHSO_4$ Pellet**

A $CsHSO_4$ membrane was fabricated by pressing in an evacuated die set at (55 MPa). The membrane thicknesses whose permeations were examined are 0.1 cm, 0.05 cm and 0.02 cm. The test bed consists of a 1.25 cm diameter permeation cell made of chrome plated stainless steel with both the delivery and receiving compartments separated by the membrane under study. The membrane as used here consists solely of the disc material investigated. The permeation cell was placed in a gravity convection electrical oven (Yamato DX 300) with programmable temperature controlled within ±1 ^{o}C.

H_2S is delivered to the delivery compartment of the permeation cell to contact the solid membrane via 316 stainless steel tubing regulated by a pressure regulator on the tank,

monitored by a flow meter and controlled by an in-line micrometering valve and system pressure is continuously monitored. Before each experiment the hermetic sealing of the cell was confirmed at room temperature and then at the operating temperature using nitrogen as the test gas. Nitrogen continued to flow into the two compartments at a regulated flowrate to maintain a zero pressure differential in the system. The cell is allowed to attain a steady-state temperature of 150 ^{o}C before replacing nitrogen with H_2S at a flow rate of 0.25 cm^3 min^{-1}. Again, the flows in the two compartments are regulated to maintain a zero pressure differential after which, the flow of nitrogen is cut off from the receiving compartment and the system is allowed to attain steady-state at which the differential pressure remained constant with time. Once steady-state was achieved, the pressures in the two compartments and the differential pressure between the two compartments were noted. If the membrane material is permeable, H_2S will pass through the membrane to the receiving compartment driven by a pressure drop in the delivery compartment. This pressure drop would lead to a decrease on the existing pressure differential as more H_2S permeates through the membrane. Gas samples of 22 nmol were taken from the receiving compartment every 10 h for GC-MS analysis using a gas-tight syringe for an extended period of 96 h. Since the volume of the delivery compartment is 127 μL, 0.39 % cell volume is utilized for each sample analysis. The permeability measurements were carried out separately for each membrane thickness (0.1 cm, 0.05 cm and 0.02 cm) investigated.

4.6 **Experimental Procedure**

In this work, experiments were conducted using the constructed cell and fabricated cell ($CsHSO_4$-based MEA) prepared earlier to electrolyze H_2S gas at different voltage applications in order to study the effect of variation of voltage on H_2S splitting. Subsequently, this was followed by a series of experiments to elucidate the performance of the MEA materials by applying different anode electrocatalysts configurations as shown in Table 4.1 at constant applied voltage 900 mV to split H_2S. Although this voltage is high compared to the thermodynamic decomposition potential, commercial application requires keeping energy consumption as low as possible. This entails working at high current and low voltage. Because of poisoning of the anode catalyst by sulfur in the presence of Pt, RuO_2 was used which acts as the host matrix while CoS_2 is used as the modifier as outlined in the factorial experiment. The electrochemical cell was placed in a gravity convection electrical oven (Yamato DX 300) with programmable temperature controlled within ±1 ^oC. H_2S introduced into the anode compartment of an electrolytic cell contacts the solid electrolyte and catalytic anode, and splits electrolytically to form liquid sulfur at the anode and gaseous hydrogen at the cathode at a temperature at which liquid sulfur has a low viscosity and can flow out of the electrolytic cell quickly and easily. The solid curve in Figure 2.3 gives the viscosity of liquid sulfur and shows that it is minimized near 150 ^oC. The cell operating pressure is 138 kPa. The proof of this principle is now accomplished.

Table 4.1 Various catalysts configurations of anode catalysts.

No	Anode catalyst	Cathode catalyst
S1	RuO_2/p-dichlorobenzene/$CsHSO_4$/Pt black	Pt black
S2	RuO_2/p-dichlorobenzene/$CsHSO_4$	Pt black
S3	RuO_2/$CsHSO_4$	Pt black
S4	CoS_2/p-dichlorobenzene/$CsHSO_4$	Pt black
S5	CoS_2/RuO_2/p-dichlorobenzene/$CsHSO_4$	Pt black

Electrons are removed in the anode compartment to yield hydrogen ions and liquid sulfur. The liquid sulfur pools at the bottom of the compartment and runs out of a drain tube there for collection. The liquid pool seals the drain tube against outflow of hydrogen sulfide from the compartment. Hydrogen ions pass through the solid electrolyte to the cathode compartment where they gain electrons to form hydrogen gas that flows out at the top. The hydrogen produced flows into a manifold from which samples are taken for analyses. The gas is collected for analysis by displacement of water in a graduated container that immediately shows its volume. For safety, the water includes dissolved alkali to absorb any acid gas contaminants. The hydrogen so collected is analyzed by using an Agilent 6890N GC gas chromatography. The current generated and the cell resistances were measured using a computer interfaced LabView program.

4.7 **Synthesis and Ionic Conductivity of $CsHSO_4$**

$CsHSO_4$, used both in the electrocatalyst and electrolyte layers, was synthesized by chilled acetone-induced precipitation from aqueous solutions of stoichiometric quantities of $CsSO_4$ and H_2SO_4 (see Eqn. (4.1)) followed by vacuum filtration. The resulting $CsHSO_4$ powder was vacuum dried in a Schlenk filtration manifold for a period of 24 h at 80 ^oC under nitrogen atmosphere to remove any acid gas and other contaminants.

$$Cs_2SO_4 + H_2SO_4 \rightarrow 2CsHSO_4 \qquad (4.1)$$

The mechano-chemical process employing high energy planetary milling was initiated by loading pure $CsHSO_4$ powders into a ball mill referred to as Fritsch pulversette planetary mono mill, P6 in an inert atmosphere. 10 grams of powder and 15 stainless steel balls (1.5 cm in diameter, 14 g in mass) were sealed under inert, into the stainless steel vials (80 cm^3 volume). The rotation speed of the milling vials (ω, anticlockwise rotation) which are fixed onto a rotating disk and the rotation speed of disk (Ω, clockwise rotation) can be set independently. Milling condition was associated by 3 essential parameters (Ω (rpm)/ω (rpm)/ Δt (h)) where Δt was the duration of the milling process. The milling parameters such as ball to powder mass ratio and milling speed were optimized to 20/1 and 300 rpm, respectively. The milling duration was 3 h after which the fine crystal powder was stored in a dessicator prior to characterization. The $CsHSO_4$ that did not pass through the process of ball milling was also stored in a desicator.

Proton conductivity measurements of unmodified and modified $CsHSO_4$ were carried out by electrochemical impedance spectroscopy (EIS) in the temperature range of 60–280 ^oC.

The unmodified and modified, as used in this context, represent $CsHSO_4$ that did not pass through the mechanical ball milling and that which was subjected to mechanical ball milling process respectively. The ionic conductivity of $CsHSO_4$ disc was measured by two-probe AC measurements techniques. In the 2-probe setup only two leads wires are located at the endpoints of the copper strips as shown in Figure 4.3. A disc of $CsHSO_4$ was made by pressing a measured amount of modified $CsHSO_4$ in a vacuum die set. This disc was then sandwiched between two copper gold plated strips serving as the electrode material and placed in a programmable furnace with a heating rate of 3 $^{o}C\ min^{-1}$. The impedance measurements was carried out with an Agilent HP 4284A LCR impedance analyzer interfaced with a computer in the frequency range of 20 Hz–1 MHz with an applied voltage of 1.0 V. The whole process starting from disc preparation to conductivity measurements were repeated for the unmodified $CsHSO_4$.

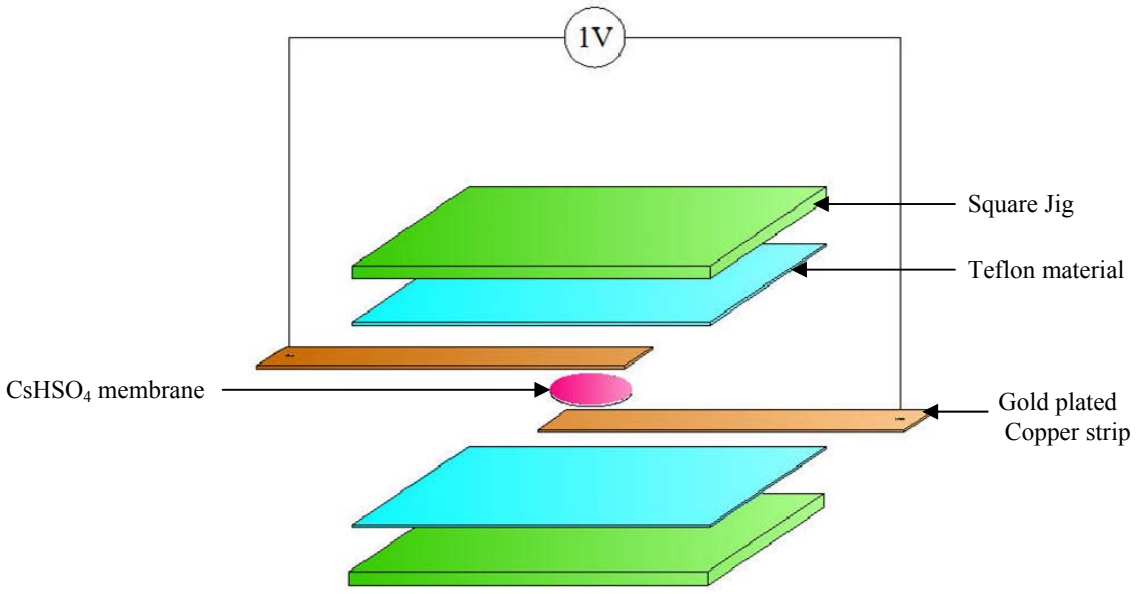

Figure 4.3 Illustration of the two-probe AC conductivity measurement setup.

4.8 **Design of Experiments**

A full factorial experiment was utilized to investigate different combinations of process variables factors at different treatment levels in the electrolytic system. This technique was employed to identify possible interactions between variables and also directs the modeling and characterization of the system.

Table 4.2 shows the tested variable factors, the levels of testing (high and low), and the measured effects for metal sulfides based anodes. The number of experimental runs is limited by using a 2^{k-1} design. Fractional designs are expressed as l^{k-1}, where l is the number of levels of each factor investigated, k is the number of factors investigated.

Table 4.3 gives the experimental combinations of chosen variables. Other factors are kept constant except for the chosen variables in order to maintain consistency and minimize error in the experiment. These other factors includes H_2S flow rate (0.25 cm^3/min), current collector wires, cathodes, H_2S delivery tubes, etc. in order to reduce any outside interference to the measurements.

Table 4.2 Factors, treatment levels, and effects for metal sulfides.

Variable Factor	Variable Name	Treatment Level		Measured Effects
		High	Low	
Electrolyte thickness	a	0.2 mm	1 mm	l_A , R_{cell}
Time on stream	b	12 hr	6 hr	l_A, R_{cell}
Electrolyte age	c	1 day	7 days	l_A, R_{cel}l

Table 4.3 Two-level 3-factor full-factorial experiment design pattern. + and –'s refer to the treatment levels (high-low) of each factor.

Run Order	Comb.	Factors		
		a	b	c
1	(1)	-	-	-
2	a	+	-	-
3	b	-	+	-
4	ab	+	+	-
5	c	-	-	+
6	ac	+	-	+
7	bc	-	+	+
$8 = 2^3$	abc	+	+	+

5 RESULTS AND DISCUSSION

5.1 XRD Structural Characterization of Modified and Unmodified $CsHSO_4$

The powder X-ray diffraction (XRD) of the synthesized $CsHSO_4$ was carried out by a Philips X'pert diffractometer with Cu Kα radiation of known wavelength, λ = 1.54060 Å. The incident and the diffraction slit width employed for the measurements are 1^o and 2^o respectively and mask size is 0.10 cm. Prior to this measurement the diffraction from the paraffilm tape was calibrated and the angle of occurrence 13^o was obtained. Phase identification and particle size calculations have been carried out by PANanalytical X'pert Highscore software version 1.0f[62].

XRD characterization was employed for structural characterization of solid acid for purpose of phase identification, structure determination, and crystal orientation. Figure 5.1 (a) and (b) represent the XRD diffractograms of both the unmodified and modified $CsHSO_4$ respectively. In Figure 5.1 (b), the spectrum obtained has a reduction in size at maximum intensity as a result of decrease in particle size resulting from the mechano-chemical process of the 3 h ball mill under a N_2 ambient environment.

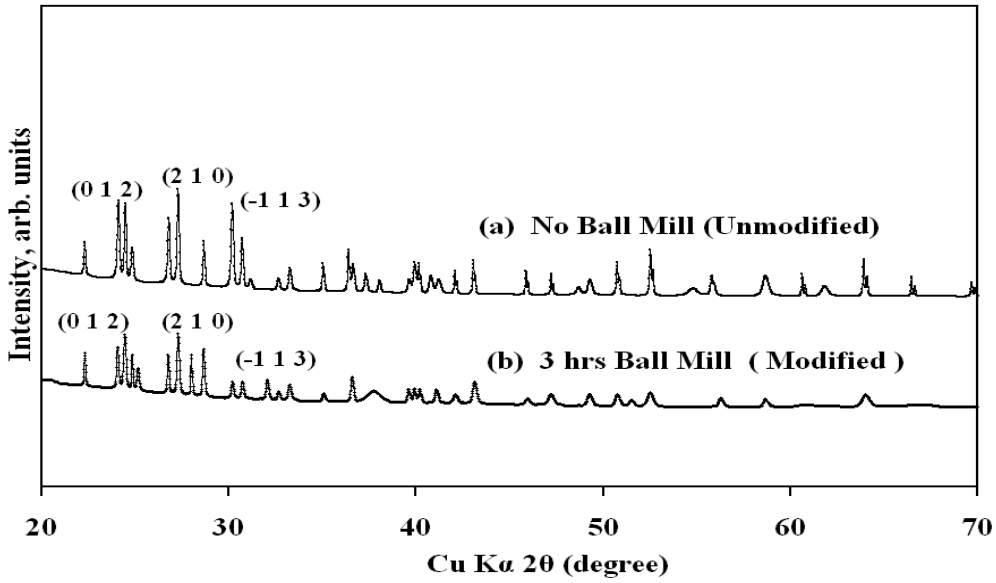

Figure 5.1 X-ray diffractograms of (a) unmodified and (b), modified $CsHSO_4$. Reflections at high intensities in all and the miller indices assigned to the reflection peaks correspond to $CsHSO_4$ (phase III).

The XRD pattern of powders produced under these conditions, (Ω (rpm)/ω (rpm)/ Δt (h)), 300/50/3, of power values of shocks was selected to test the performance of our conductivity model. It is expected that ball milling process will improve the concentration of defects resulting from disorder of this material and facilitate the rate of proton diffusion and hence increase its ionic conductivity as a result of increase in the number of vacant sites for proton migration[51,51] . It has been known from previous studies that the behavior of this material is preceded by order-disorder phase transition. Also from Scherrer's calculation shown in Table 5.1, it was observed that the particle size decreased with mechanical pulverization of the ball milling process as compared to a non milling condition.

Table 5.1 Comparison of crystal parameters for unmodified and modified $CsHSO_4$.

Preparation method	Unmodified	Modified
Crystal size calculation from Scherrer's equation	33.4 nm – 75 nm	18.6 nm – 28.2 nm
FWHM	0.0984	0.1574

The full width at half maximum (FWHM) intensity of the modified $CsHSO_4$ increased (at least two times) with ball milling as depicted in Table 5.1 reflecting a reduction in intensity of the reflected spectra in Figure 5.1a.

5.2 **Simultaneous Gravimetric and Calorimetric Analysis of $CsHSO_4$**

Analysis using Simultaneous differential scanning calorimetry and thermo gravimetric analysis (SDT) for the weight loss and the heat flow for the reaction enthalpy during the superprotonic phase transition and the thermal decomposition temperatures of $CsHSO_4$ were estimated by the TA SDT-Q600 analytical tool. The calibration of SDT was carried out in four steps with an empty pan and standard sapphire disc. The four calibration subroutines such as thermo gravimetric analysis (TGA) weight, differential thermo analysis (DTA) baseline, and temperature and differential scanning calorimetry (DSC) heat flow were performed before sample measurements were conducted. A pre-weighed sample was loaded into the ceramic pan and covered with the ceramic lid to prevent air or moisture from getting into the sample. The ramp rate for the SDT measurements was 2 ^{o}C/min. TA's universal analysis 2000 software program was used to analyze the SDT profiles.

A typical thermal analysis result for a $CsHSO_4$ sample at fixed heating rate (3 $^oC\ min^{-1}$) is presented in Figure 5.2. The TGA and DSC results are presented. The TGA analysis shows the temperature at which $CsHSO_4$ is decomposed and that is in consonance with the literature reported value for this material which place the decomposition temperature of this material between 200 ^oC to 220 ^oC[20]. For the decomposition of $CsHSO_4$ by the following reaction:

$$2CsHSO_4 \rightarrow Cs_2S_2O_7 + H_2O \qquad (5.1)$$

a weight loss of 0.8 % was observed at 197.91 ^oC while an expected weight loss at 220 ^oC was ~1 %.

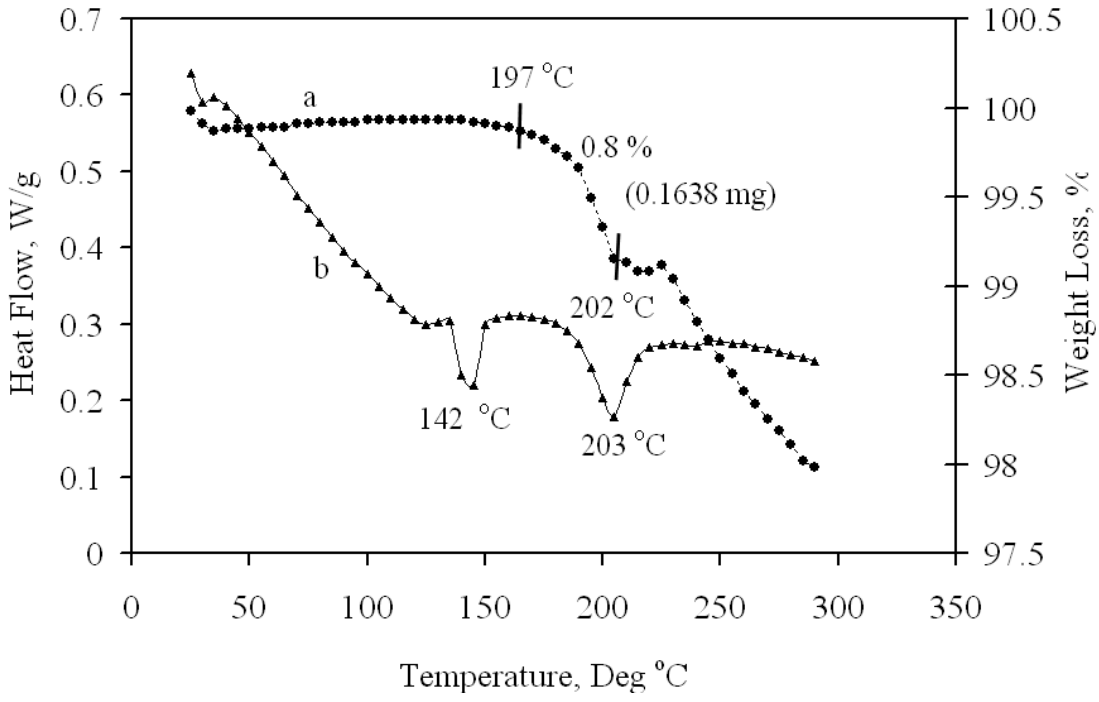

Figure 5.2 Simultaneous differential scanning calorimetry and thermogravimetric analysis (SDT) measurement. (a) TGA spectra showing weight loss, $CsHSO_4$ decomposes into: $2CsHSO_4 \rightarrow Cs_2S_2O_7 + H_2O$; (b) DSC spectra showing the phase transition and decomposition temperatures of $CsHSO_4$[52].

It is evident from these thermal measurements that the decomposition of this material progressed with increasing temperature and rapidly degrades at higher temperatures. Quite significantly, regardless of sample surface area, in all cases (modified or unmodified) a phase transition, independent of decomposition, is clearly evident at ~ 142 ^{o}C. Although the impact of this transition on conductivity cannot be assessed from thermal analysis alone, we assign this transformation as the superprotonic transition described earlier[32,63].

5.3 Ionic Conductivity Modeling of $CsHSO_4$

Protonic conductivity was the principal property of interest in the material examined here. For this, extensive use of alternating current (AC) impedance spectroscopy has been made to characterize the protonic conductivity of solid acid compound (modified and unmodified) as a function of temperature at ambient pressure. This is necessary since no information on the ionic conductivity of mechano-chemically processed $CsHSO_4$ exist so, this will provide a datum for comparison with known data from previous works on unmodified method. As mentioned earlier, superprotonic behavior of solid acids compound is (to date) always associated with an order-disorder phase transition and they conduct via a vacancy mechanism. Therefore, effort has been made to characterize these phase transition. Thermal analysis to measure the temperature of this transition, as well as to evaluate decomposition behavior, has been an essential tool in these investigations.

Conventionally, impedance data is analyzed using an equivalent circuit consisting of a parallel resistor- capacitor (RC) elements connected in series[64]. As shown in Figure

5.3(a), R and C are the resistance and capacitance of the circuit components. The complex impedance of the resistor and capacitor of RC element in parallel can be described as:

$$Z = \frac{R}{(1 + jwCR)} = \frac{R}{1 + jw\tau} \tag{5.2}$$

where $\tau = RC$, and τ is the time constant of the RC element. Each parallel RC element of the equivalent circuit used to represent an electro-active region within the sample will result in a semicircular arc in the complex impedance plane, Z plot as shown in Figure 5.3 (c). The frequency at which the semicircular arc maximum occurs is determined by the time constant τ of the parallel RC element as described by:

$$w_{\max} = \tau^{-1} = (RC)^{-1} \tag{5.3}$$

where $w_{\max}$ is the angular frequency at the top of the semicircular arc. According to Eqns. (40) and (41), the elements of the equivalent RC circuit can be extracted from Z plots, and the fitting results of $CsHSO_4$ sample was shown in Figure 5.3 (d). The curve n<1in the Figure 5.3(d) is draw according to the fitting results. Based on the simple RC equivalent circuit, the semicircle in Z plane should be a full one with its center on the real axis of the complex plane.

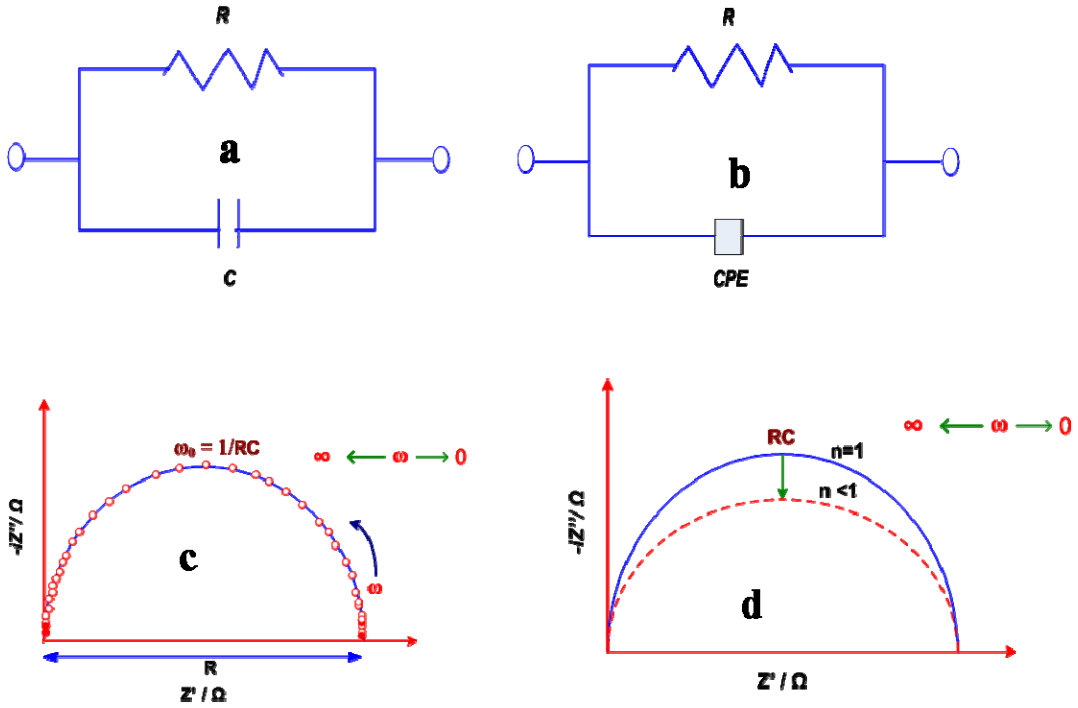

Figure 5.3 The elements of the equivalent RC circuit and the fitting results of $CsHSO_4$ sample. (a) The RC effective circuit; (b) the modified model: the resistor and the CPE element connected in parallel; (c) Nyquist plot of (a); (d) experimental data (square dots) and fitting results (solid lines) of the $CsHSO_4$ sample. Z' and Z'' are the real part and image part of the complex impedance Z, respectively. Curve n=1 represents the RC model (a) and Curve n<1 represents the CPE model (b).

However, as shown above, experimental data are only rarely found to yield a full semicircle, instead depressed one with its center below the real axis. The observed plot was indeed the arc of a circle, but with the center some distance below the x-axis. This is mainly due to the distribution of the relaxation time τ, continuous or discrete, around a mean $\tau_m = w_m^{-1}$. The observed plot is related to charge storage phenomena. The interface impedance behaves as if there are two components in parallel. The fictitious element responsible for this behavior is known as the constant phase angle element (CPE) in place

of the capacitor. In order to circumvent that and obtain a good fitting, the CPE was introduced to replace the capacitor in the RC circuit, as shown in Figure 5.3 (b). And the impedance of CPE can be described as[65]:

$$Z_{CPE} = \left(\frac{1}{A}\right) \times (jw)^{-\psi} \tag{5.4}$$

where A and ψ are frequency-independent parameters which usually depend on temperature, and $0 \le \psi \le 1$. The CPE describes an ideal capacitor with $C = A$ for $\psi = 1$ and an ideal resistor with $R = 1/A$ for $\psi = 0$, and the experimental data is corresponding to $0 < \psi < 1$ generally. The complex impedance of the equivalent circuit of the resistor and CPE in parallel can be described as:

$$Z = \frac{R}{\left(1 + (jw)^{\psi} RA\right)} = \frac{R}{\left((1 + jw)^{\psi}\right)} \tag{5.5}$$

where $\tau^{\psi} = RA$, and Eq. (5.3) may be expressed as:

$$w_{\max} = \tau^{-1} = (RA)^{-1/\psi} \tag{5.6}$$

According to the Eqns. (5.5, 5.6), equivalent circuit elements can be fitted from the Z plane. Curve n<1 in Figure 5.3(d) is fitting result by using CPE model, and fitting parameters (e.g. R, A and τ). Curve n<1 is closer to the experimental data than Curve n=1, so the CPE element is an effective tool to fit the experimental data. The refined material resistance R is then normalized by using area specific resistance (ASR), then:

$$\sigma = L/ASR \tag{5.7}$$

L is the length of the conductor, the lower the resistance and ASR = RA (representing the pellet resistance and area respectively). It is intuitive that a shorter path results in less resistance.

The results of AC impedance measurements for polycrystalline samples under ambient pressure conditions are presented in Arrhenius plot in Figure 5.4(a, b) for modified and unmodified $CsHSO_4$ respectively.

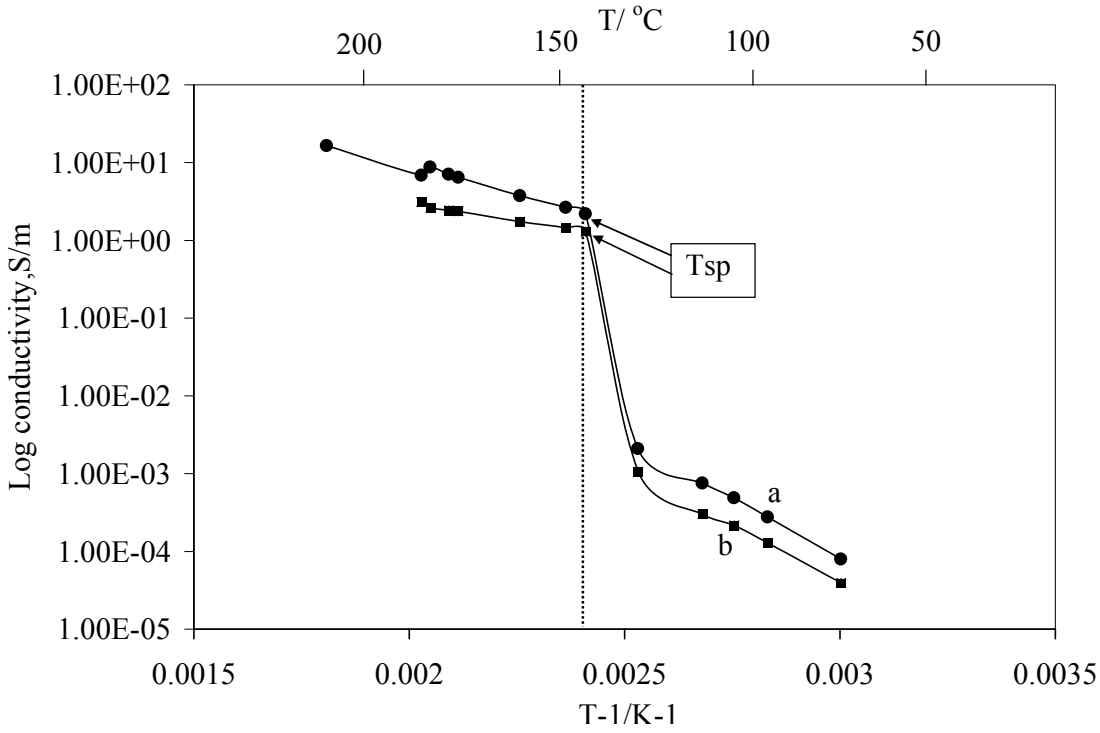

Figure 5.4 Fitting the conductivity to Arrhenius law upon heating at 3 $^{o}C\ min^{-1}$. (a) modified; (b) unmodified ($CsHSO_4$) respectively. T_{SP} is the superprotonic phase transition temperature (142 ^{o}C).

The activation enthalpy or migration enthalpy (ΔH_a) of H^+, carrying one elementary charge $\Delta H_a \approx 0.59$ eV and the frequency factor, A_o obtained for modified and

unmodified samples were $2.0 \times 10^5\ \Omega^{-1}\ cm^{-1}\ K$ and $0.5 \times 10^5\ \Omega^{-1}\ cm^{-1}\ K$ respectively. The activation enthalpy value obtained agrees well and falls within the reported literature value of $\Delta H_a \approx 0.3\text{-}0.66$ eV reported for this material[66]. Representative Nyquist plots obtained at temperatures above the superprotonic phase transition temperature T_{SP} are presented in Figure 5.5. The conductivity of both sample conditions increased sharply at the transition temperature. Moreover, the jump in conductivity was significantly lower for the unmodified pellet than for the modified crystal sample. An explanation for this behavior is that more vacancies are intentionally introduced into the lattice by ball milling thereby providing a faster route for hydrogen proton mobility. Above the T_{SP}, neither sample type exhibited a linear, Arrhenius region, as is typical for other superprotonic conductors[67]. Below the superprotonic phase transition ($T < T_{SP}$), Figure 5.5(a), well-resolved semi-circles were observed. The real resistance of the sample at low temperatures was identified by the intercept of the semicircle with the real axis (Z'). The apex of the semicircle, ωo, is the characteristic frequency defined in terms of the resistive and capacitive response of the material under test. In contrast, at $T \geq T_{SP}$, the resistance approaches that of a single crystal, Figure 5.5 (b), and the intercept with Z' was used as the estimated resistance of the sample. In both cases (modified and unmodified), the conductivity increased by 3 to 4 orders of magnitude at the transition temperatures.

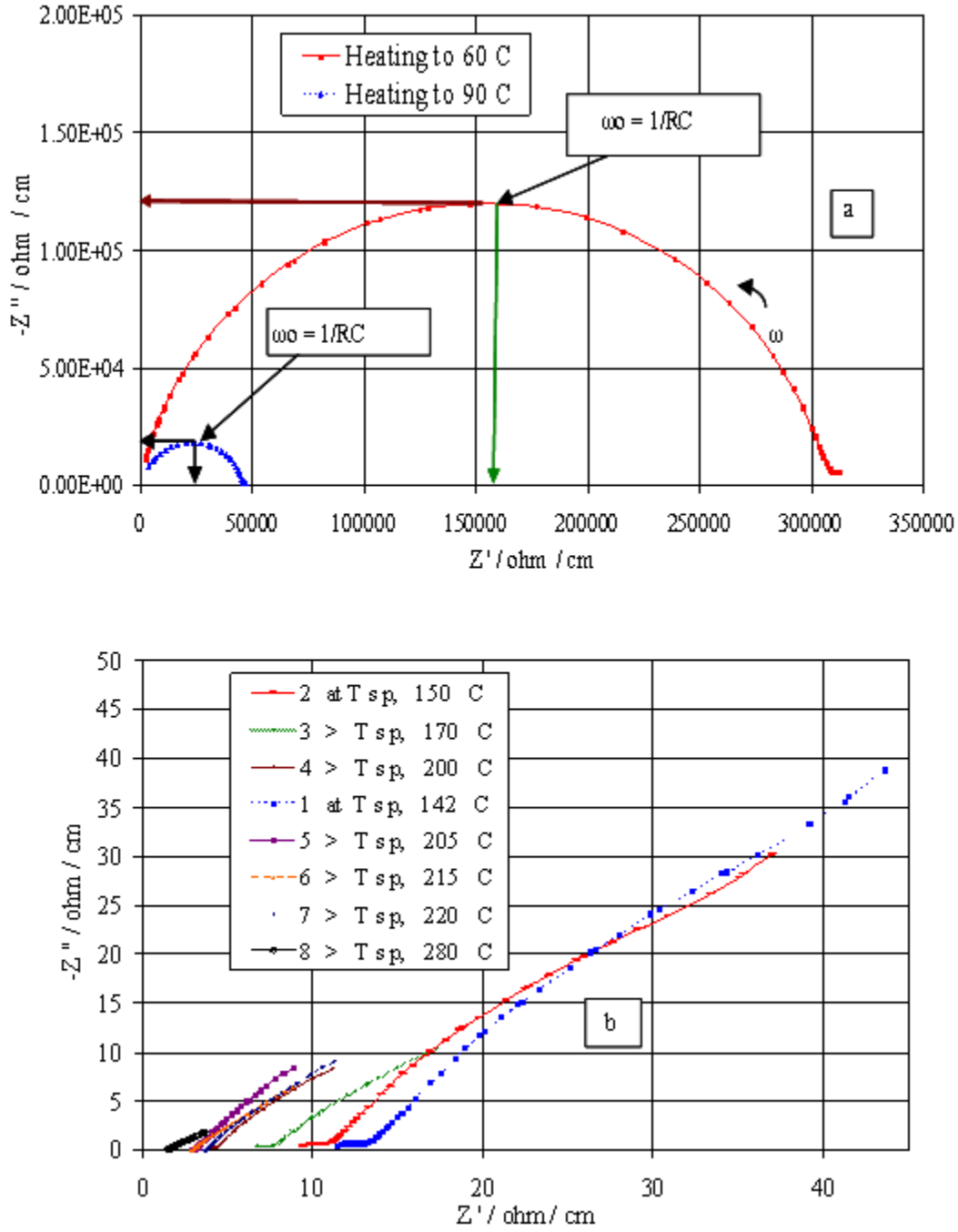

Figure 5.5 Nyquist plots at various temperatures upon heating ($CsHSO_4$). Below and above its superprotonic transition temperature (Tsp) for modified polycrystalline pellet; (a) at T< Tsp; (b) at T> Tsp.

In conclusion, high energy planetary milling process was applied successfully to improve the ionic conductivity of $CsHSO_4$. The electrochemical impedance spectroscopy measurements indicate that the three hour mechano-chemical pulverization process by ball milling quadrupled the ionic conductivity of $CsHSO_4$. However, simultaneous differential calorimetry and thermogravimetric analysis indicate that the decomposition temperature of 202^oC for both the modified and unmodified remained constant. . It is hoped that the application of ball milled $CsHSO_4$-based membrane to electrolytic splitting of hydrogen sulfide gas will show a great promise in reducing the activation barriers associated with this type of process.

5.4 **Permeability of H_2S on $CsHSO_4$ Membrane**

5.4.1 **Morphological Characterization of the Surface**

Any surface morphology changes of the $CsHSO_4$ membranes due to H_2S exposure were investigated by atomic force microscope (AFM). The surface structure was analyzed before and after the permeability study at several different locations in order to obtain an average roughness value. The AFM was utilized in contact mode making use of a sample-stationary scanning device by means of a Digital Instrument piezoscanner with x, y, z cantilever displacements.

The 1D AFM images with area of 1 μm x 1 μm of the $CsHSO_4$ membranes before and after permeability testing are shown in Figure 5.6. The surface analysis performed show that both samples in Figure 5.6 (a, b) have a smooth textured surface constituted of rounded grains with a RMS roughness of 5 nm. Furthermore, the structures are continuous, with a well-defined geometry and a rounded profile. This observation

indicates that prolonged exposure to (100 %) H_2S does not significantly affect surface morphology. A possible reason for the surface morphology retention may be attributed to the compact layered structure of the membrane which resists diffusion of any kind (molecular, Knudsen and surface) on the surface of the membrane in contact with H_2S even after prolonged hours (100 h) of operation.

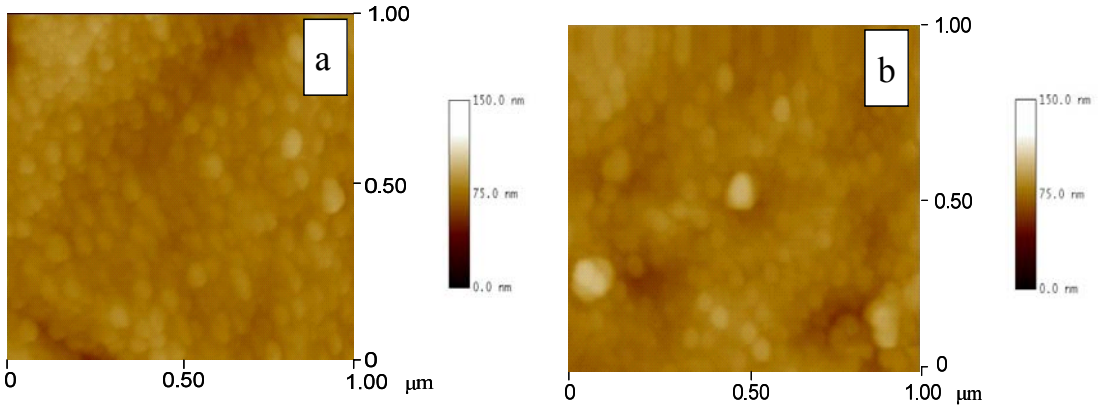

Figure 5.6 Atomic force microscope images of $CsHSO_4$ membranes used in the permeation study. (a) image before permeability measurement; (b) image after permeation process.

5.4.2 **Gas Chromatography and Mass Spectrometry Analysis**

Samples drawn from the receiving compartment were analyzed by gas chromatography and mass spectrometry (Shimadzu GC-MS-QP5000) utilizing an Agilent technology column DB-5 with column length, thickness and diameter (30 m, 0.25 µm, and 0.25 mm) respectively with helium being used as carrier gas.

A GC analysis is shown in Figure 5.7. In Figure 5.7(b-f)), the spectra obtained indicated that no H_2S gas was detected after the passage of H_2S through $CsHSO_4$ membrane for the three membrane thicknesses investigated. None of the spectra observed has a peak that matched the retention time of H_2S peak. MS analyses identified the remaining peaks as a

composition of diatomic nitrogen and water, which infiltrated the system from the nitrogen purge gas and water displacement apparatus. The GC-MS results are further supported by the absence of pressure drop across the membranes tested as well the information obtained from the graphical representation of Eqn. (2.2). This is also consistent with an earlier study[68] which involved splitting of H_2S electrolytically using a $CsHSO_4$-based membrane in which no H_2S gas was detected in the product stream.

Based on findings in this study and in corroboration with earlier analyses, $CsHSO_4$ is impermeable to H_2S gas. Though a theoretical result via mathematical modeling capable of simulating quantitative H_2S-transport has not been explored and is beyond the scope of this work.

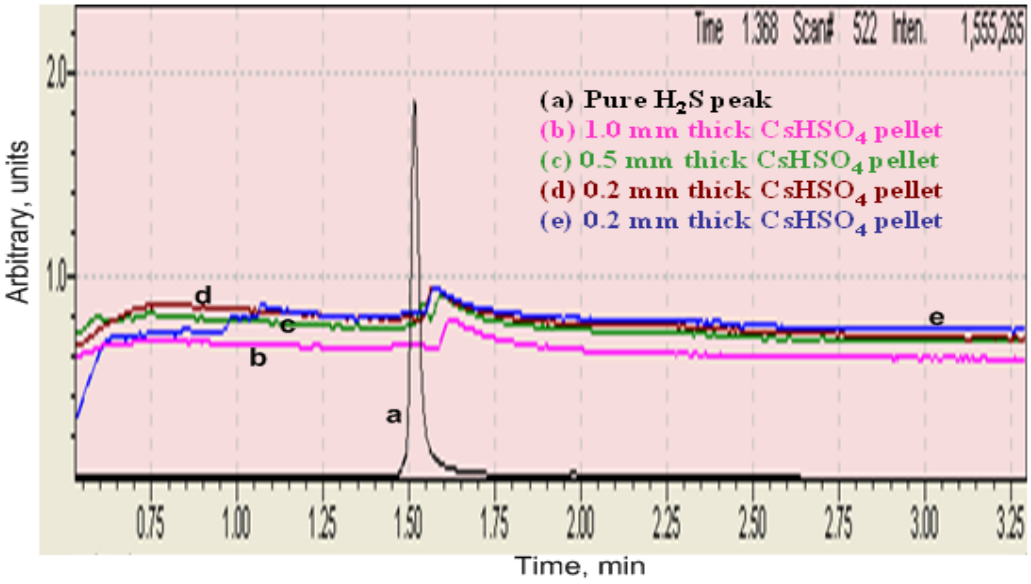

Figure 5.7 Qualitative comparison of permeability at 150 C by GC-MS instrument. (a) Pure H_2S gas; (b) measurement of H_2S permeability through 1 mm thick $CsHSO_4$ membrane; (c) permeability test with a 0.5 mm thick $CsHSO_4$ membrane (d-e) effect of further reduction in $CsHSO_4$ membrane thickness on H_2S permeability at 150 ^oC during a period of 24 h and 100 h respectively.

5.4.3 **Micropore Analysis**

To compare pore size distribution in the material before and after the permeability measurements, the distribution of pore volume with respect to pore size was determined with Autosorb-1 software, ASI WIN from Quantachrome instruments before and after the permeation tests. The Autosorb-1 operates by measuring the quantity of gas adsorbed onto or desorbed from a solid surface at some equilibrium vapor pressure by the static volumetric method. This volume-pressure data can be reduced by the Autosorb-1 software into pore size and surface area distributions and, micropore volume using an extensive set of built-in data reduction procedures. The analysis most suitable for this study used a type of ASI WIN software based on the Saito-Foley (SF)[69] method which assumes cylindrical pore geometry to calculate pore size distributions within a microporous range. The apparent pore distribution isotherms using a computational approach based on the Saito-Foley (SF) method for the membrane before and after the permeation study are shown in Figure 5.8. It is clearly seen that both isotherms (a, b) remain congruent during 100 hours of data acquisition, which implies that the passage of H_2S has no significant influence on the apparent pore diameter distribution. Differentiation of weight (volume) of gas adsorbed relative to the total uptake, W/W_0, with respect to the effective pore width yields a pore size distribution in the micropore range expressed as a Gaussian isotherm[70]. W is the weight adsorbed at P/P_0 and T, and W_0 is the total weight adsorbed. P/P_0 and T are the relative pressure and adsorption temperature (K) respectively. The mean pore diameter values are randomly distributed around the average d_{SF} = 10.5 Å. The two isotherms both exhibited a narrow range of pore size distribution with no evidence of any mesopores or macropores present as shown

in Figure 5.8. One conclusion that can be inferred from this observation is that the pores in $CsHSO_4$ are not connected. Furthermore, due to the range of pore diameter sizes and the narrow pore walls of the membranes, when compared to the mean free path of H_2S molecules, could have contributed to the non porosity observed. No previous work on the pore size distribution of $CsHSO_4$ could be found to compare our results; therefore we rely on the accuracy of the measurements obtained before and after the permeability study in addition to our earlier observations to arrive at this conclusion.

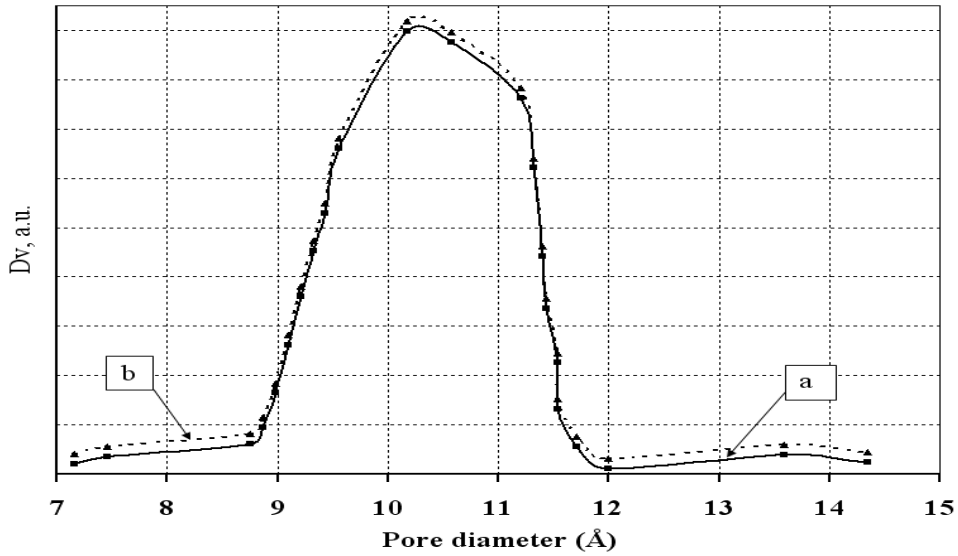

Figure 5.8 A typical Saito-Foley (SF) D_V (d) method of pore size distribution isotherm. Measured on, (a) CsHSO4 membrane before permeation investigation; (b) $CsHSO_4$ membrane after permeation investigation.

5.4.4 **XRD Analysis**

The phases of $CsHSO_4$ are sensitive to external conditions, so the aim of the XRD analysis is for structural characterization of $CsHSO_4$ membrane in order to identify the phases present, structure determination, and crystal orientation. The XRD pattern of $CsHSO_4$ membrane before and after permeation testing is presented in Figure 5.9 (a, b).

In agreement with Belushkin et al.[71] the XRD pattern for $CsHSO_4$ membrane before and after permeation testing correspond to a mixture of monoclinic structural phases III/II. It is clear from the diffractogram in Figure 5.9 (b) that there is no mixture of different phases from passage of H_2S gas through the membrane. As a result, the structure and phases of the membrane are preserved. The diffractogram depicts a typical sample comprising one crystalline phase with the same average crystalline sizes. All XRD measurements were performed on samples at room temperature, but the different sample history exhibits the same XRD patterns.

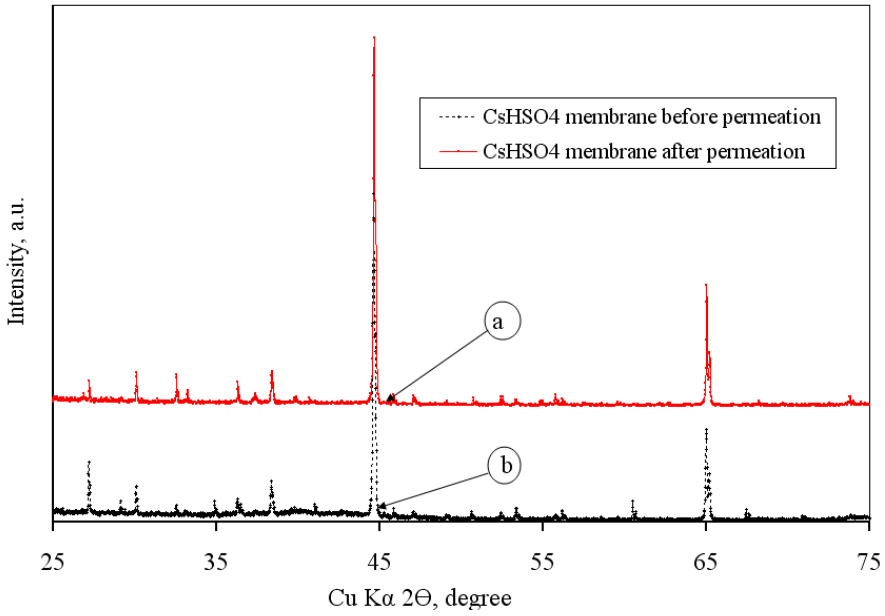

Figure 5.9 XRD diffractogram of $CsHSO_4$ with different sample history. Here, (a) XRD pattern of $CsHSO_4$ membrane before permeability measurements; (b) XRD pattern of $CsHSO_4$ membrane after permeability study.

5.4.5 **Resistance Measurements of $CsHSO_4$ Membranes**

Resistance measurements as a function of temperature of $CsHSO_4$ were examined by EIS in the temperature range of 142–170 ^oC. This was carried out by two-probe AC

measurements techniques. In the 2-probe setup only two leads wires are located at the endpoints of the copper strips. The apparatus is similar to the ionic conductivity measurements (see Figure 4.3).

The use of alternating current (AC) impedance spectroscopy has been made to characterize the resistances at two different thicknesses (1 mm and 0.2 mm) of $CsHSO_4$ membranes investigated for permeability as a function of temperature at ambient pressure. Since we have confirmed the impermeability of 0.2 mm thickness to H_2S gas, it will be worthwhile to also study the effect such reduction will have on the membrane resistance. The temperatures selected for this examination were 142, 150, and 170 ^oC. These are the temperatures at which $CsHSO_4$ experience a jump in its protonic conductivity the so-called the "superprotonic phase"[72,73]. Also, in the electrolytic splitting of H_2S the viscosity of sulfur product is minimized at 150 ^oC such that it can flow out of the electrolytic cell without hindrance[54].

The Nyquist plot at three different temperatures is shown in Figure 5.10 for the two cases of 1 mm and 0.2 mm $CsHSO_4$ membranes. As was in the ionic conductivity measurements, real resistance of the samples at these high temperatures was identified by the intercept of the spectra with the real axis (Z′). At the superprotonic transition phases ($T \geq T_{SP}$), only an electrode response was observed, so the intercept with Z′ was used as the estimated resistance of the sample.

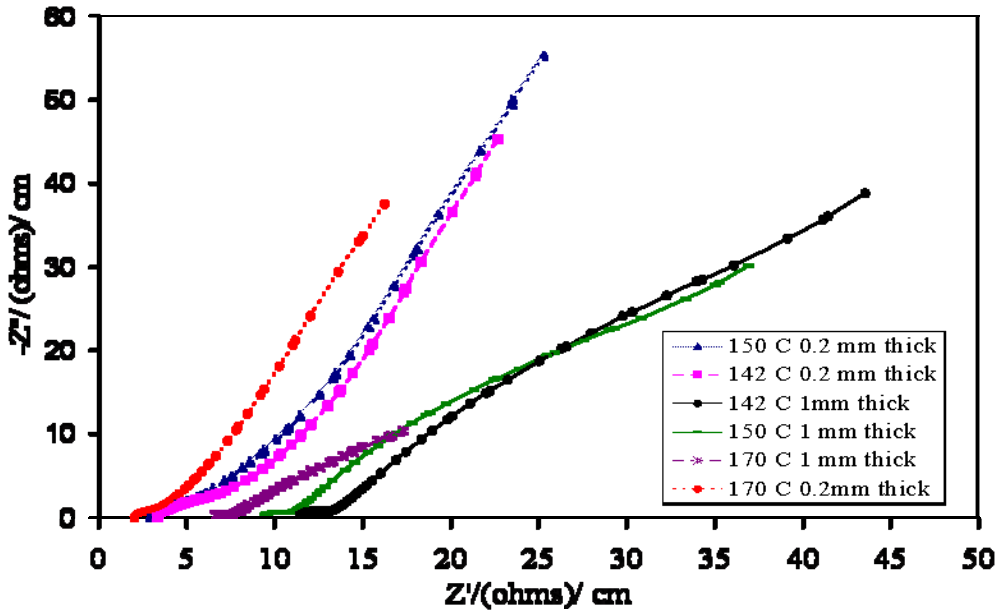

Figure 5.10 Nyquist spectra at and above $CsHSO_4$ superprotonic transition temperatures (Tsp) for the two membrane thicknesses 1 mm and 0.2 mm. Reduction in resistance with membrane thickness is shown by the intercept of the spectra with the real (Z′) axis.

The decrease in resistance as the thickness is reduced from 1 mm to 0.2 mm is confirmed in the spectra for the three temperatures. Although, it was expected that the reduction in thickness by 80 % will have equal effect on the resistance but, only about 30 % reduction in the resistance was achieved as shown by the Nyquist spectra observed. Nevertheless, the correlation between the membrane thickness and its resistance as observed in the Nyquist spectra shows that thinner membranes will be more effective in minimizing ohmic polarization experienced when this membrane is used for electrochemical synthesis[59].

5.4.6 **Permeability**

The permeability of the membrane was tested by measuring the pressure differences in the permeation compartments which could only loose pressure by the passage of material through the membrane[74,75]. Figure 5.11 shows permeability of H_2S gas through $CsHSO_4$ membrane and the pressure drop observed as a function of time. The pressure drop observed was not sufficient to sustain any driving force necessary for material crossover through the membrane. Therefore, pressure differential in the cell remained absolutely constant even with continuous influx of H_2S gas through out the experimental period. Also, the duration of the experimental period has no effect on the permeability of H_2S on $CsHSO_4$ membrane since this value remained fairly constant. The membrane maximum permeance is 0.09 Barrer (6.75×10^{-19} $m^2.s^{-1}.Pa^{-1}$) which is insignificant to support any material crossover. The permeation profile of H_2S for $CsHSO_4$ membrane is a function of pressure difference across the membrane[73].

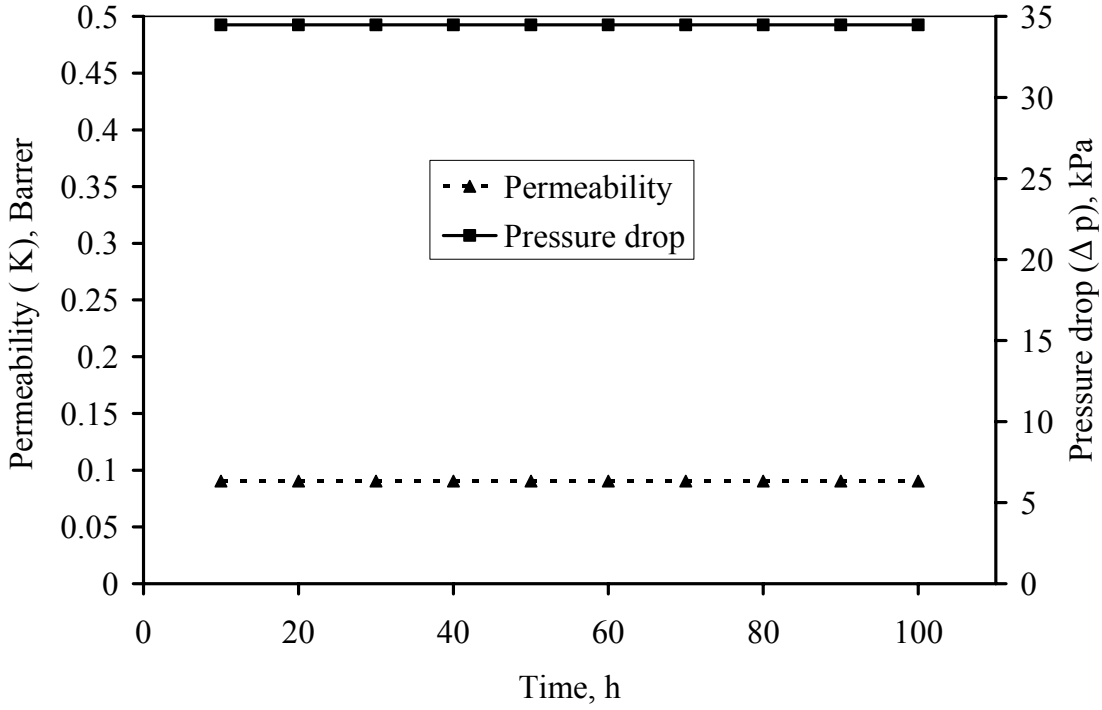

Figure 5.11 Permeability and pressure drop as a function of time for $CsHSO_4$ membrane.

Both diffusive and convective gas transport contributed to the total flux over the membrane. We assumed that the mean free path of the gas molecule is greater than the pore diameter due to the microporous nature of our membranes and the low pressure regiment of operation. Therefore, it will be a reasonable assumption to state that Knudsen diffusion dominates over molecular diffusion through out the experimental time. Also the difractogram obtained from XRD analysis show only one crystalline phase present which is an indication that H_2S did not adsorb on the surface of the membrane thereby ruling out any contribution from surface diffusion. Diffusion coefficient of H_2S through $CsHSO_4$ (1.38×10^{-8} cm^2 s^{-1}) were based on estimation by Gilliland et al.[76]. The impact of molecular diffusion on the diffusivities is beyond the scope of this investigation. But the resistance to diffusion along the pore could be attributed primarily to molecular collisions

with the wall rather than with each other, as in ordinary diffusion. Nevertheless, in the intermediate regime both wall collisions and intermolecular collisions contributed to the diffusional resistance and the effective diffusivity depends on both the Knudson and molecular diffusivities.

5.5 **Electrochemical Synthesis**

5.5.1 **Current Density from H_2S Splitting**

The current density generated at a constant cell pressure of 138 kPa and H_2S flowrate 0.25 cm^3/min is shown as function of voltage applied for modified and unmodified $CsHSO_4$-based MEAs. Figure 5.12 (a, b) show current density as function of voltage based on the total exposed surface for modified and unmodified cases respectively. The results of Figure 5.12 show that higher current density was attainable by applying modified (Figure 5.12 (a) than the unmodified (Figure 5.12 (b) CsHSO4-based MEAs. One explanation proposed is that the reduction in particle size, which results from mechano-chemical pulverization of the ball milling process, creates more defect structure in the material. This in turn facilitates the rate at which hydrogen protons are being transported from the reaction sites hence, favoring the reaction kinetics.

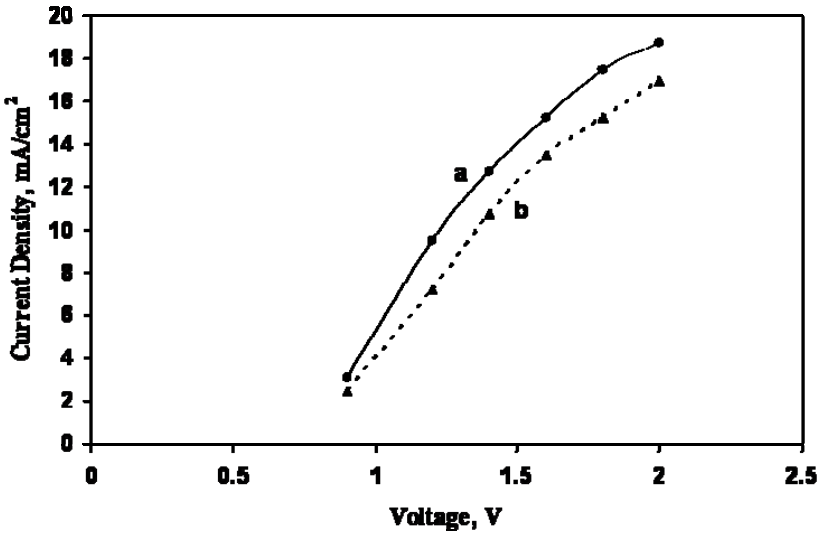

Figure 5.12 Current density as a function of voltage generated with anode catalyst S3. (a) using modified ($CsHSO_4$-based MEA); (b) applying unmodified $CsHSO_4$-based MEA).

For both scenarios in (Figure 5.12), the curve is linear as Ohms law at lower current density. At higher currents diffusion limitations seem to be coming into play. However, other factors such as, mass transport limitations (concentration losses), electronic conduction and activation losses (losses due to electrochemical reaction) will affect the cell performance. In consideration that this is a novel investigation, our preliminary data was on the proof of principle, therefore, system optimization will take into account the effects of these factors on the system performance which is the topic of the factorial experiments covered later in the document.

5.5.2 **Electrolysis of H_2S**

Examination of the performance of the MEAs at a constant applied voltage of 900 m V was carried out on three different anode catalysts configurations as shown in Table 4.1 for both cases of modified and unmodified $CsHSO_4$. Our intention is to minimize the

overvoltage required to split H_2S electrolytically, hence 900 m V was selected for this study. The sustainable application of anode catalyst (S1) for 8 h of operation has now been demonstrated. The conversion of H_2S (feed: 100 %), during the first 8 hours of operation, is shown in Figure 5.13. In Figure 5.13 (a, b), curves (S1) (representing the anode catalysts used) shows that conversion increased steadily until it attained a constant value of 100 % and 92 % respectively after 5 hours of operation. The conversion rate is limited by the membrane current density attainable. Figure 5.13 (a, b), curves (S2) and (S3), which represent the anode catalyst used, did not show appreciable H_2S conversion under the same conditions.

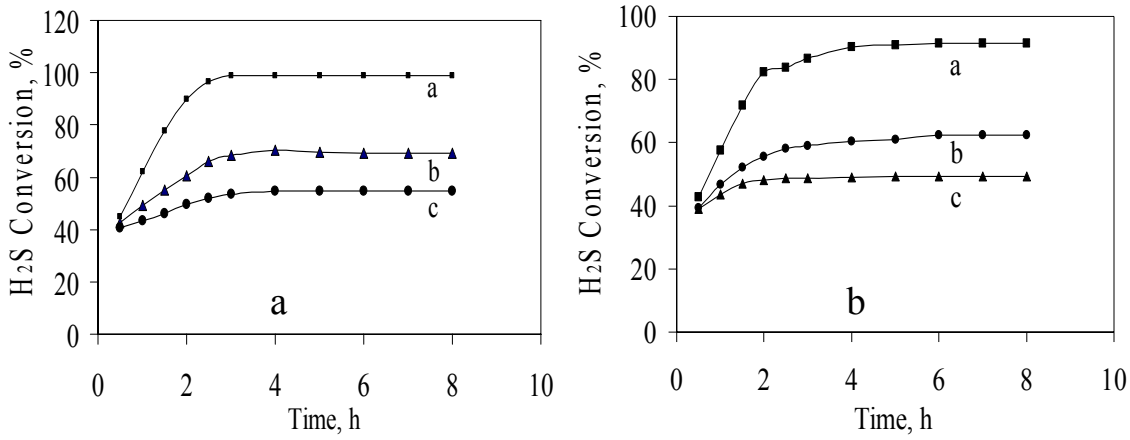

Figure 5.13 Relationship of H_2S conversion to time on stream with a voltage 900 mV. (a) modified ($CsHSO_4$-based MEA) with anode catalysts configurations: S1, S2, S3; (b) unmodified ($CsHSO_4$-based MEA) at different anode catalysts combinations: S1, S2, S3.

The exclusion of Pt black in curves (S2 and S3) decreased the rate at which electrons are being conducted away from the electrolyte surface after reaction. Pt black as an electron conductor facilitated the rate at which these electrons are being transported away from the reaction surface as H_2S conversion proceeds as evident in curves (S1) which have

high rates of H_2S conversion. Curve (S3) shows the lowest t performance because of the absence of a good porous media for gas diffusion which decreases the rate at which feed gas is transported to the reaction surface. The inclusion of p-dichlorobenzene in catalysts (S1) and (S2) provides a good porous media needed for gas to contact the reaction surface easily and rapidly. In the final analysis, modified $CsHSO_4$-based MEA (Figure 5.13 (a)) has a higher rate of H_2S conversion when compared to the unmodified $CsHSO_4$-based MEA (Figure 5.13 (b)) which exhibit a lower conversion rate, although, this increase is more prominent in the presence of Pt black catalyst and p-dichlorobenzene as evident in Figure 5.13 (a) curves (S1 and S2). A proposed explanation of this is the action of the mechano-chemical pulverization of $CsHSO_4$-based MEAs which enhanced the rate at which hydrogen protons hop from position to position within the lattice and ensures that reaction proceeds smoothly by transporting hydrogen proton away from the reaction surface as soon as they are formed. This conclusion is supported by conductivity measurements which indicate that modified $CsHSO_4$ conductivity is improved by the action of the ball milling process.

The relationship of current generated verses time is shown in Figure 5.14 for the two cases of modified and unmodified $CsHSO_4$-based MEAs under study. As expected, anode catalyst (S1) proved to be a superior catalyst since it provides favorable kinetics over catalyst configurations (S2 and S3). The current generated was sustainable over an extended operating period (5 h), as evident from the values between the third and eight hours of operation.

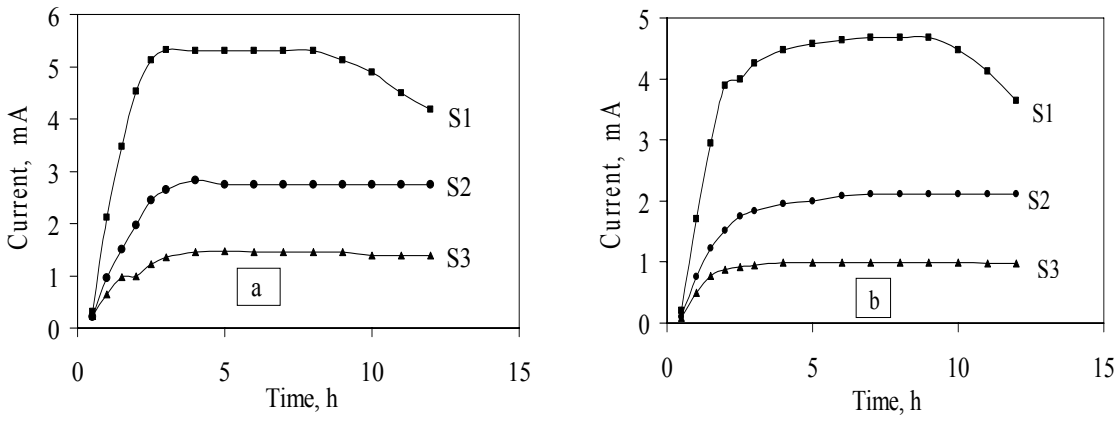

Figure 5.14 Relationship of current to time during a period of 12 h of operation with a voltage 900 mV. (a) modified ($CsHSO_4$-based MEA) at different anode catalysts configurations: S1, S2, S3; (b) unmodified ($CsHSO_4$-based MEA) with different anode catalysts combinations: S1, S2, S3.

As seen in Figure 5.14, the performance of catalyst (S1) degrades after 8 hours of operation. Such degradation was not seen for catalysts S2 and S3. It is proposed that this behavior is due to concentration polarization resulting from sulfur poisoning of Pt black catalyst. For sustainability over a long operational period, additional investigation is warranted as future work in order to minimize this effect. The durability of the catalysts and membranes, and sensitivity to pore blocking or catalyst deactivation by deposited sulfur, will be presented in a subsequent section. Again, the current generated was less for the unmodified than for the modified $CsHSO_4$ as expected given that current generated is a function of ionic conductivity of the electrolyte. Nevertheless, the correlation of current generated and H_2S conversion proves that the process is indeed the due to the electrolytic splitting of H_2S, and not as a result of interaction between MEA materials.

5.5.3 **Material Balance**

H_2S was electrolyzed for 5 hours at a steady voltage of 900 mV with anode catalyst S1 (see Figure 5.13 (a)) which produced a sustained current of 0.00531 A. At the anode, the half redox equation for electrolysis is:

$$H_2S \rightarrow 2H^+ + 2e^- + (1/8)\, S_8 \qquad (5.8)$$

2 moles of electrons (2 Faradays) are required to produce 1/8 mole of S_8 and 2 moles of hydrogen ions. A current of 0.00531 A for 5 hours represents 95.58 coulombs or (95.58/96,500) = 0.001 Faraday. This is sufficient to produce 0.001 moles (0.001 g) of hydrogen ions and 6.25E-5 moles (0.016 g) of S_8. At the cathode, the half redox equation for electrolysis is:

$$2H^+ + 2e^- \rightarrow H_2 \qquad (5.9)$$

The 2 moles of hydrogen ions produced in Eqn. 5.8 are converted to 1 mole of hydrogen gas in Eqn. 5.9. The 0.001 moles (0.001 g) of hydrogen ions produced at the anode by 0.001 Faraday are converted to 0.0005 moles (0.0005 g) of hydrogen gas at the cathode.

For the gas measurement, the gas issuing from the cathode compartment was collected and measured by displacement of water in a 50 cm^3 burette at 25 ^oC and 102.4 kPa. The observed volume was 10 cm^3. Gas collected by displacement of water is saturated with water vapor whose vapor pressure at 25 ^oC is 3.17 kPa. The partial pressure of hydrogen in the burette was then (102.4 -3.17) = 99.2 kPa. By the ideal gas law, 0.0004 moles of gas has a volume of 10 cm^3 at a partial pressure of 99.2 kPa and temperature of 25 ^oC. Thus the measured volume of hydrogen gas is about 80 % of the theoretical limit for the electrolysis as calculated in the previous section. We are unable to account for the

remaining 20 % which may have resulted due to some current leakage in the system; this is currently under investigation. .

5.5.4 **Stability of H_2S Electrolytic Cell Anode Materials**

Electrocatalysis offers a convenient route to the synthesis of H_2S. Requisites of the anode material are a low overpotential for product evolution and high stability. We have tested a group of anode electrocatalysts for their suitability as endurance materials for H_2S splitting. A particular one of interest is the metal sulfide group comprising RuO_2/CoS_2 composite which has shown in this application to be stable and efficient in splitting H_2S gas.

Figure 5.15 illustrates the XRD pattern for RuO_2/CoS_2 as prepared, after 12 h exposure to H_2S, and after 24 h exposure to 100 % H_2S content feed gas at 150 ^oC. This composite shows no phase or compositional changes after exposure to (100 %) H_2S gas at the cell operating temperature. The chemical stability of this material in H_2S was expected, as the preparation of RuO_2/CoS_2 anode composite was done with the intention to increase its catalytic activity via the mechano-chemical pulverization process in inert (99.5 % nitrogen) atmosphere at elevated temperature 150 ^oC. The stability of RuO_2/CoS_2 when exposed to H_2S (for prolonged periods of time) made it an attractive anode candidate for H_2S splitting.

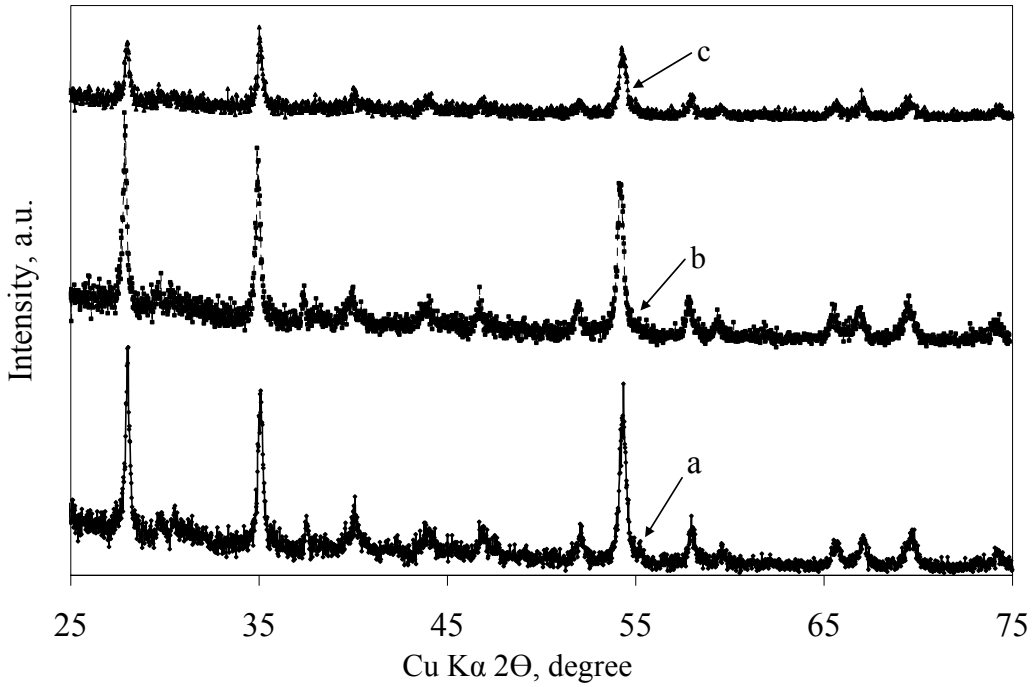

Figure 5.15 XRD pattern for (RuO_2/CoS_2 composite). (a) as prepared; (b) after 12 h exposure to 100 % H_2S feed content at 150 ^oC; (c) after 24 h exposure to 100 % H_2S feed content at 150 ^oC.

The catalytic active surface area of the composite was obtained by using a Multipoint BET method which requires a minimum of three points in the appropriate relative pressure range as shown in Figure 5.16. At high relative pressures, the rate of adsorption equals the rate of desorption which is very essential for material catalytic performance. The specific surface area calculated from the total surface area for the composite is (10.96 m^2/g). This is sufficient to sustain the reaction without interruption by providing sufficient compensation for sulfur poisoning as well as providing enough area for the reaction for the reaction to proceed.

Table 5.2 shows a list of different anode configurations and their corresponding BET surface areas. The small catalytic active areas exhibited by both RuO_2 and CoS_2 when compared to RuO_2/CoS_2 composite could be responsible for the blockage of the anode surface by sulfur as observed in the SEM image (see Figure 5.17). As mentioned previously, this occurrence decreases the rate of chemical reaction which adversely affects the overall performance of the system.

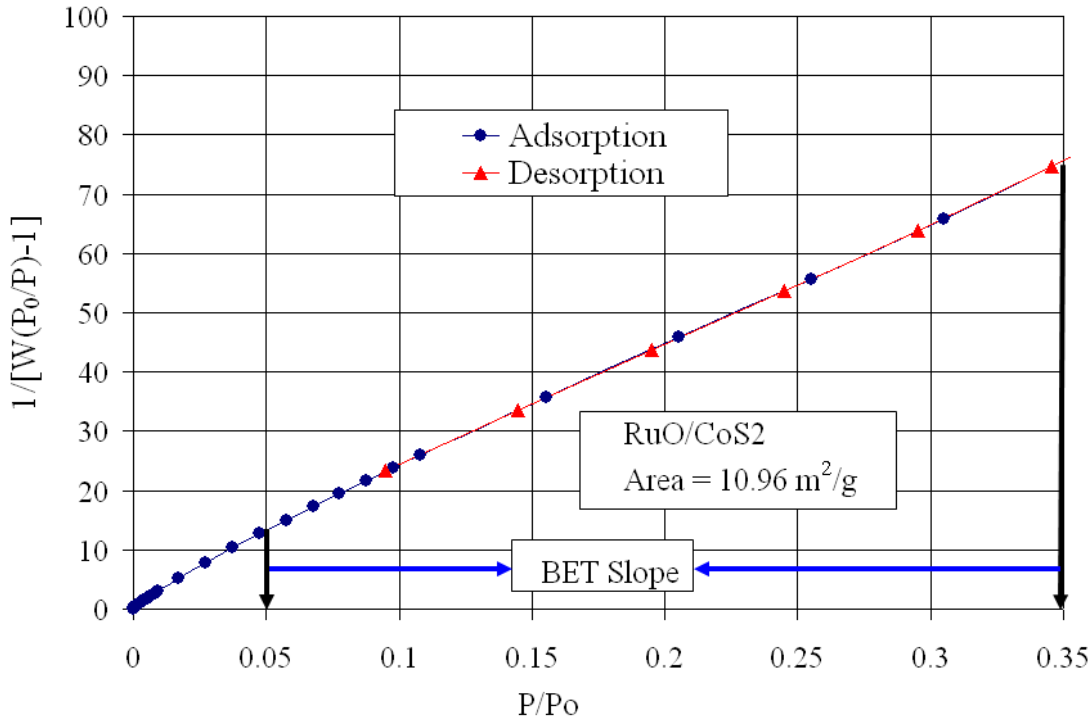

Figure 5.16 Multipoint BET plot for anode metal sulfide (RuO_2/CoS_2) nanocomposite.

Table 5.2 Various anode configurations and their BET catalytic active areas.

Catalysts	BET , Specific Surface Areas (m^2/g)
CoS_2	6.77
RuO_2	6.41
RuO_2/CoS_2	10.96

The composite RuO_2/CoS_2 has a relatively high surface and expanded area metallic nanoparticles facing away from the electrolyte. Figure 5.17 shows a scanning electron micrograph of a porous electrode (composite nanoparticles on carbon mesh support for strength). These electrodes have tortuous pathways within them to expose orders of magnitude larger surface areas to reacting H_2S and to also allow the escape of the liquid sulfur product. The increased numbers of catalytically active sites as mentioned earlier enables the materials to be more resistant to poisoning. This is because these materials exhibit a certain number of catalytically active sites that can be sacrificed to the effects of poisonous sulfur production as shown in Figure 5.17 (b) while a large number of unpoisoned sites are preserved. In Figure 5.17 (c, d) which consists of non composite materials, the catalytic efficiency of the material is substantially less than that possible if a greater number of catalytically active sites were available. This was due to concentration polarization caused by sulfur blockage of the diffusion layers. In all the runs involving RuO_2/CoS_2 composite, there was only a trace amount of sulfur deposition on the anode surface.

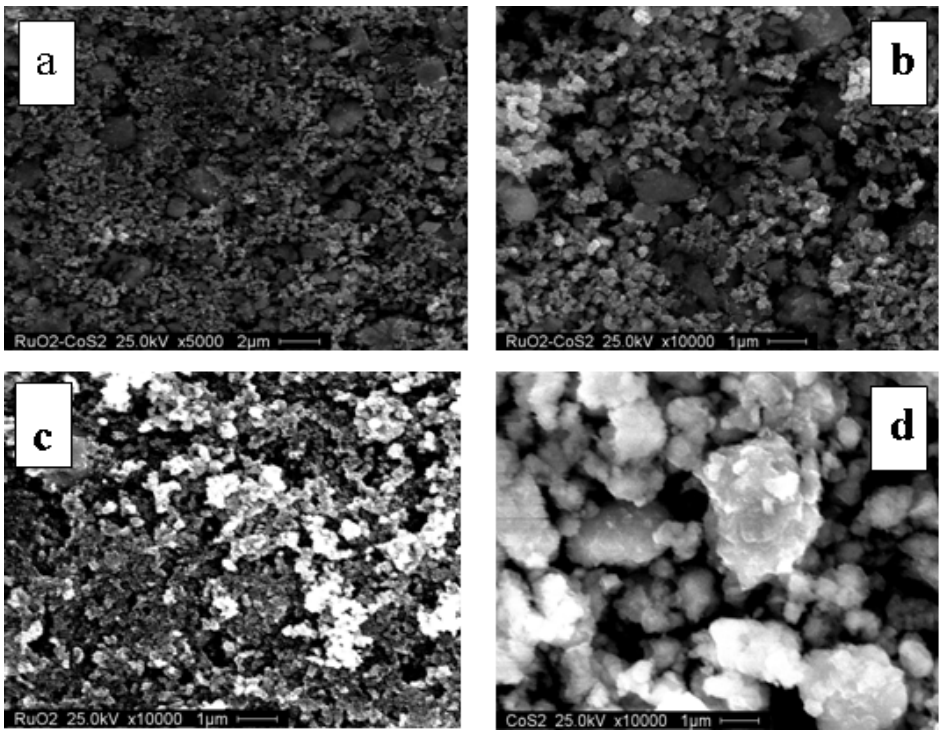

Figure 5.17 SEM images of surfaces of electrode. (a) RuO_2/CoS_2 electrocatalyst nanocomposite before electrolysis; (b) RuO_2/CoS_2 electrocatalyst nanocomposite after electrolysis; (c) RuO_2 electrocatalyst after electrolysis; (d) CoS_2 electrocatalyst after electrolysis.

5.5.5 **Electrochemical Performance of Anode Electrocatalysts**

The first sets of experimental runs, as shown in the previous sections, were aimed at examining the stability and performance contribution of the Pt electrocatalyst. It was shown that Pt degrades with time even though it gave the best performance but at a short period of time. Figure 5.18 compares the performance of four cells using: Figure 5.18 (a) modified with RuO_2/CoS_2 and Figure 5.18 (b-d) modified with CoS_2, modified with RuO_2 and unmodified with RuO_2 respectively as anode materials at 150 ^oC. Unmodified and modified as used in this context is the same as in previous sections. The conversion process did not affect any of the anode materials used and no de-lamination of the anode from the $CsHSO_4$ electrolyte was apparent. The performance of the RuO_2/CoS_2

composite anode was far superior to any of the anode materials. All the configurations initially increased, and subsequently maintained their performances for over 12 hours. Consequently, prior to measuring performance in all subsequent experimental runs, cells were operated at an input voltage of 900 mV and allowed to stabilize. If no noticeable decline in output after this time period was observed, the cell was deemed adequate for performance testing. Both systems had similar electrochemical behavior and deviations were probably caused by external factors (current collection, lead wires, etc.). Factorial experiments supported this observation.

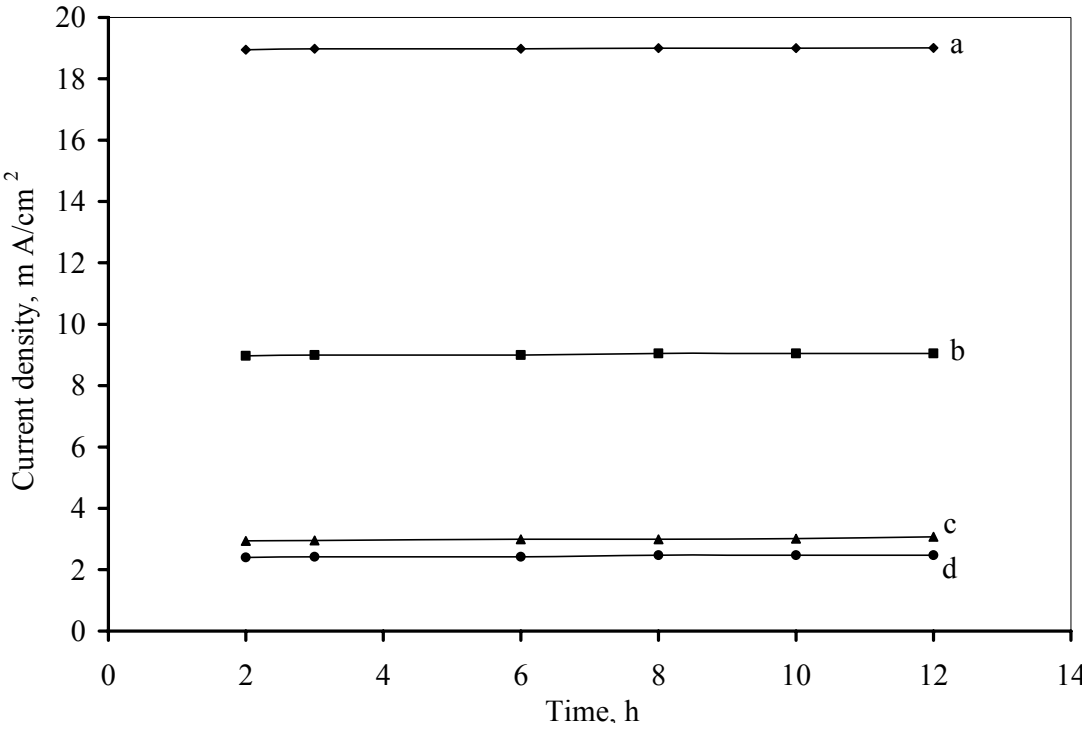

Figure 5.18 Testing for four cells with different anodes (Vcell = 0.9V, T = 150 ^{o}C, Fuel = 0.25 cm^3/min) H_2S was the fuel. (a) modified with RuO_2/CoS_2; (b) modified with CoS_2; (c) modified with RuO_2; (d) unmodified with RuO_2.

The main goal of this study was to identify and develop endurance materials for H_2S splitting electrolytically, thus full system optimization was considered a secondary goal. The large number of anode materials and experimental cells used in this project required the use of low cost materials with no system optimization configurations. For commercial applicability of this work, full system optimization will need to be carried out shown in Figure 5.19, are the effects of various anode configurations on current densities as a function of external applied voltages. Curve (a) represents the performance of the cell based on modified electrolyte with composite the RuO_2/CoS_2 anode. Curves (b-d) represent the performances of cells based on modified with CoS_2, modified with RuO_2 and unmodified with RuO_2 anodes respectively. At the low region where there are uniform potential gradients, current densities are proportional to potential gradients and are uniform; hence Ohm's law is appropriate. At high voltages, concentration gradient comes into play. By utilizing the anode composite RuO_2/CoS we were able to maintain a high current density at low potential. This is because the catalytic surface area provided by the composite highly minimized the activation barrier and also reduced most of the effects associated with concentration polarization; more gases were able to diffuse to the reaction interface and the reaction equilibrium is shifted toward product.

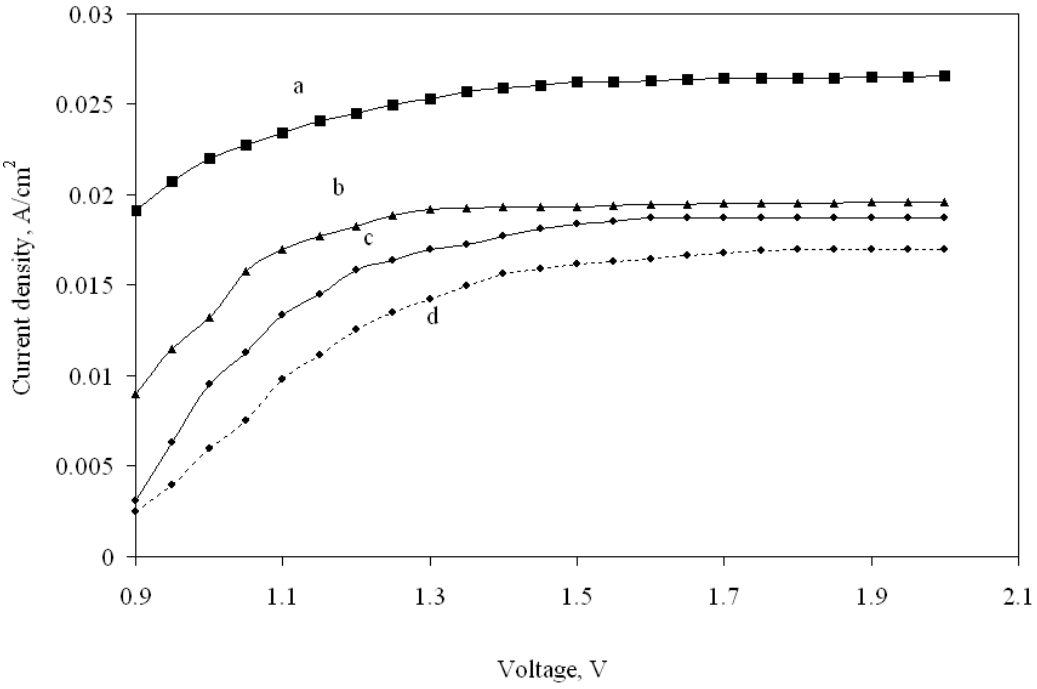

Figure 5.19 Current density for different anode configurations with 100 % H_2S feed gas content. (a) modified with RuO_2/CoS_2; (b) modified with CoS_2; (c) modified with RuO_2; (d) unmodified with RuO_2.

5.5.6 **Resistivity of Anode Catalysts**

The electrical resistivity of anode catalyst samples with the structure Au/anode catalyst/Au are listed in Table 5.3. The resistivity of composite catalyst pellet RuO_2/CoS_2 at 150 ^oC is less compared to the values obtained for CoS_2 and RuO_2 electrocatalysts. In the light of this observation, the present anode catalyst with the RuO_2/CoS_2 configuration was utilized due to superior electrical conductivity for use as anode catalysts under operating conditions. The contributions from these resistances are small compared to the total cell resistances. This suggests that the large different in current densities observed may not be significantly due to the resistances of these materials, but primarily due to the availability of catalytic active sites provided by the composite anode materials. However, it was necessary to reduce the internal ohmic resistance of the cell slightly using

RuO_2/CoS_2 anode composite. Note, as mentioned previously, the total resistances experienced by the electrolytic cell results from contributions due to, activation overvoltage loss (η_{act}) that from ohmic loss (η_{ohmic}) and from concentration loss (η_{con}). Furthermore, the contribution from η_{ohmic} comes from both the ionic and electrical resistances i.e. $j R_{ohmic} = j(R_{elec} + R_{ionic})$. Maximum current density as shown in Table 5.4 at 900 mV measured for the RuO_2/CoS_2 composite was 19 mA/m^2, which was higher than that for CoS_2 (9 mA/cm^2) using the same electrolyte thickness. To this end, we have achieved minimizing the contributions from both η_{act} and η_{con} by using the anode composite RuO_2/CoS_2 and also reducing the effect of R_{elec}. The ohmic resistance was determined from impedance measurements.

Table 5.3 Cell area specific ohmic resistance (RA). This shows different anode electrocatalysts at operating temperature of 150 ^oC.

Anode materials	RuO_2/CoS_2	CoS_2	RuO_2
RA (Ω cm^2)	3.12	7.30	9.23

5.5.7 **Fuel Utilization**

Table 5.4 summarizes the measured data in tabular form at specific operating voltage, comparing typical conditions to tested parameters. The data shows high reproducibility. The conversion efficiency depends on many factors which include the flowrate of H_2S to the reaction sites and the transportation of product away from these sites, the availability of active sites, and the thickness and nature of the electrolytes. As shown in Table 5.4, for

the same electrolyte thickness, H_2S consumption was twice the value for modified with RuO_2 as compared to unmodified with RuO_2. This suggests that the difference could be attributed to faster electrode kinetics observed with modified RuO_2 as explained in the previous sections. The fuel consumption rates had equal effects on the system efficiency for these two systems. By using a different catalyst configuration comprised of modified electrolyte with CoS_2 and reducing the electrolyte thickness by 80 % of its value boosted the system efficiency by 30 %. This led to a higher rate of fuel utilization almost tripling that observed in the case of modified electrolyte with the RuO_2 configuration. The contribution from the low resistance value of CoS_2 when compared to RuO_2 and the effect of reduction in ohmic losses as a result of decrease in the electrolyte thickness contributed to the increase observed. As pointed out previously, the reduction in the thickness of the electrolyte enhanced the fuel consumption. The introduction of the modified electrolyte with anode the composite RuO_2/CoS_2 using the same electrolyte thickness used in the modified with CoS_2 doubled the system efficiency and the fuel utilization. The increased electrode kinetics is attributed to the large active sites available for the reaction to progress, some of which were sacrificed to the effect of sulfur poisoning. This was also supported by the SEM image (Figure 5.17) after 12 hours of electrolysis.

Table 5.4 Conversion efficiency for several electrolytes. Electrolytes prepared from high surface composite nanometals (RuO_2/CoS_2) demonstrate the best performance.

0.9 V					
Fuel utilization	j, A/cm^2	Cell area, cm^2	Efficiency	H_2S flowrate, cm^3/min	Electrolyte thickness, cm
100 % utilization	0.03000	0.4	1	0.16	-
Unmodified with RuO_2	0.002475	0.4	0.06	0.01	0.1
Modified with RuO_2	0.003075	0.4	0.13	0.02	0.1
Modified with CoS_2	0.009025	0.4	0.31	0.05	0.02
Modified with RuO_2/CoS_2	0.019125	0.4	0.69	0.11	0.02

5.5.8 **Tafel Slope and Exchange Current Densities for Anode Configurations**

Improving kinetic performance stems from increasing j_0. To increase the value of j_0, we have increased the number of possible reaction sites (i.e., increase the reaction interface roughness) by incorporating a novel composite metal sulfide, RuO_2/CoS_2 electrocatalyst, in the electrode. The exchange current density is determined experimentally by extrapolating plots of In j vs. η to $\eta = 0$. This is a direct measure of the reaction rate constant at the electrolytic cell electrode. Figure 5.20 shows various plots for the anode configurations. One can use the slope t of the straight line to estimate the number of electrons involved in the electrochemical process. In all four cases of anode configurations n = 2 indicating the oxidation of H_2S to S_2. The anode composite consisting of RuO_2/CoS_2 shows great potential in reducing the activation barrier as a result of the increased catalytic active sites available for the reaction to proceed without

sulfur poisoning. This is reflected by the high exchange current density obtained compared to the configurations RuO_2 and CoS_2 which have lower values of j_0. For the composite configuration, the transfer coefficient is 0.68 and j_0 is 2.53 x 10^{-2} A/cm^2 signifying a rapid electrochemical reaction.

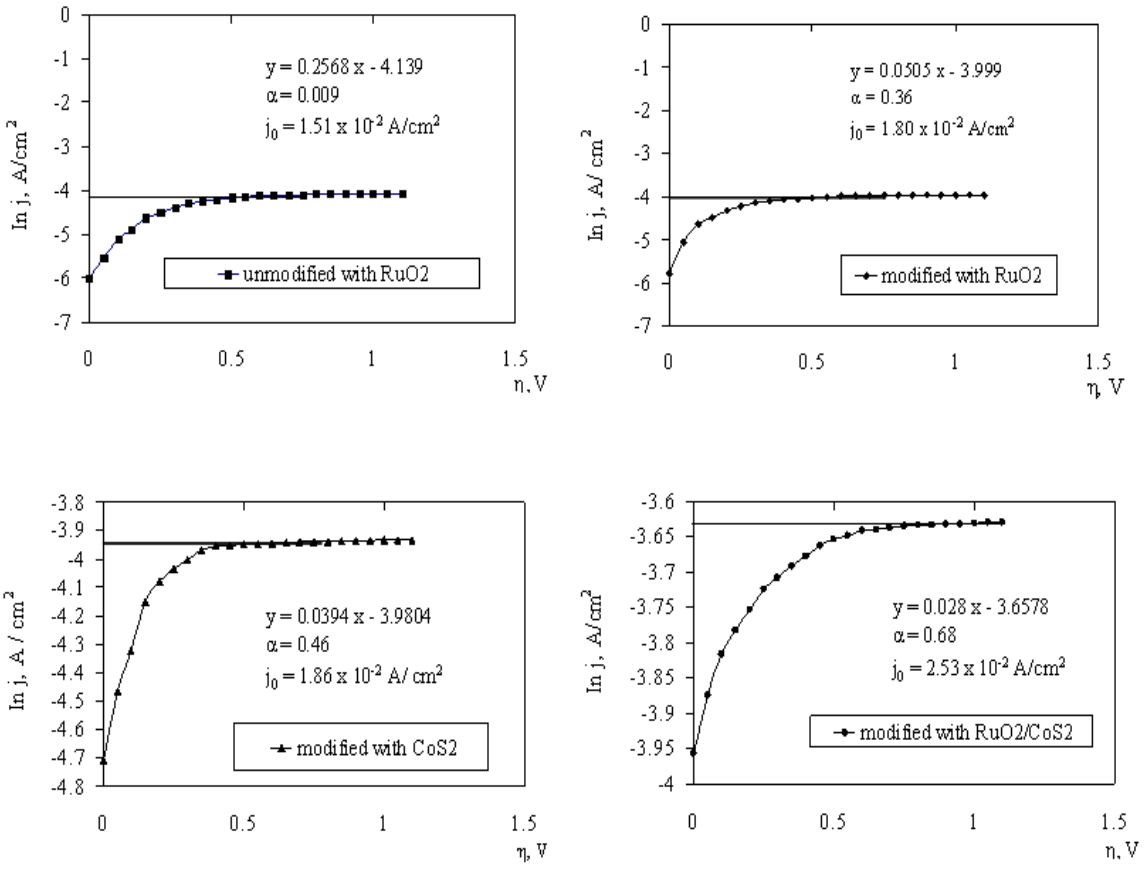

Figure 5.20 Tafel plots for anode configurations at operating temperature 150 ^oC and 100 % H_2S feed content.

5.5.9 **Factorial Experiment**

5.5.9.1 **Effect of Process Variables on Cell Resistances for RuO_2/CoS_2**

Cell polarization resistances are functions of charge transfer (electrochemical reaction) and mass transport (reactant and products) activities in the cell. A Labview program was

used to measure the effect of the three process variables on cell polarization resistances. A simplified graphical representation of results is shown in Figure 5.21. In this figure, straight lines indicate a zero effect for that particular process variable on cell polarization resistance. As expected, electrolyte thickness and age were the dominating factors on cell polarization resistance. It is not surprising that resistance decreased with age as this is in agreement with a previous study[39] which showed that the presence of H_2O molecules on the surface of $CsHSO_4$ crystal increases ionic conductivity. Since this material was not stored in a vacuum, it was prone to water vapor interaction attack on the surface of the material. However, examination of these variables shows that the most prominent dominating factor in performance is the electrolyte thickness. The interaction between these two variables is shown in Figure 5.22. As mentioned previously, resistance scales with electrolyte thickness and when normalized with area-specific resistance, a shorter path results in less resistance.

Thus, improvement of electrochemical cell performance can be achieved by utilizing thin and hydrated electrolyte membranes even though the latter contribution is not prominent. This new technique would either be more electronically conductive than previous method, or catalytically active towards the splitting of H_2S. XRD analysis showed all of MEA materials were stable when pellets of this material were exposed to H_2S-rich environments. XRD analysis performed after the electrochemical testing of cells was also unable to detect changes in either the crystal structure or composition of MEA materials after extended operation with 100 % H_2S feed gas. A second explanation was obtained

from kinetic experiments performed on the RuO_2/CoS_2 composite anode (see the exchange current density section of this document).

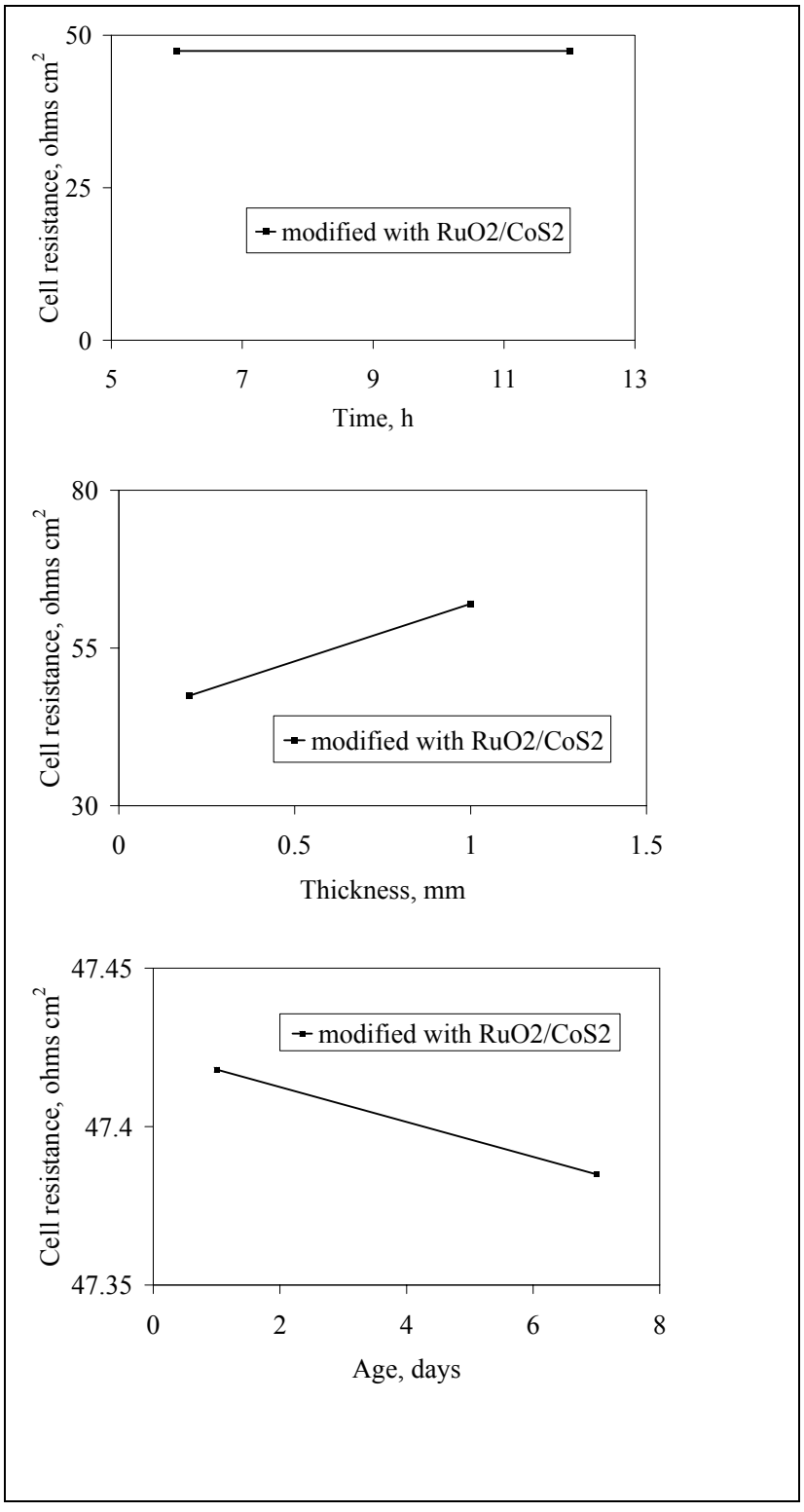

Figure 5.21 Measured effects of three process variables on cell polarization resistances. Time effect (top), electrolyte thickness (center), electrolyte age (bottom).

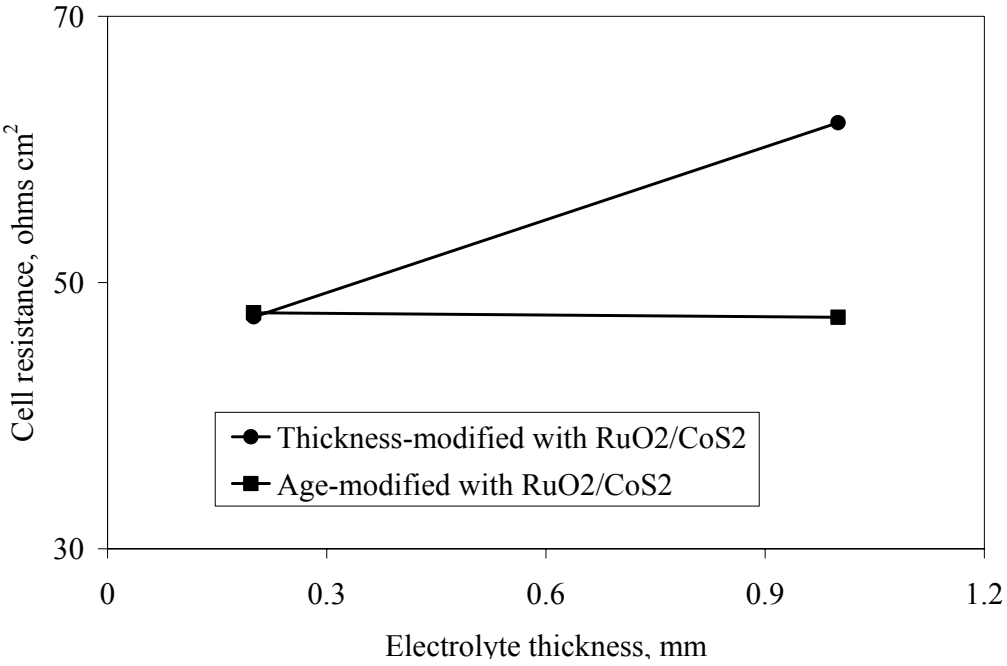

Figure 5.22 Factorial results showing the interaction effect between electrolyte age and electrolyte thickness on cell polarization resistance.

5.5.9.2 **Effect of Process Variables on Current Density for RuO_2/CoS_2**

Cell current density is inversely proportional to cell polarization resistances. Since all other experimental variables were left unaltered (i.e. H_2S flow, lead wires, etc.), cells with the lowest polarization resistance had the maximum current density. The effect of process variables on cell power is inversely proportional to that of cell resistance as shown in Figure 5.23. The benefit from factorial experiments is the ability to predict regions of optimum system performance (for future experiments) based on past results. With everything else equal, making the membrane thinner reduces the ohmic loss. However, note that the payoff does not scale directly with membrane thickness. Although the membrane thickness was cut by 80 %, the ohmic loss was only reduced by one-third.

This is because not all of the electrolytic cell's resistance contributions come from the electrolyte.

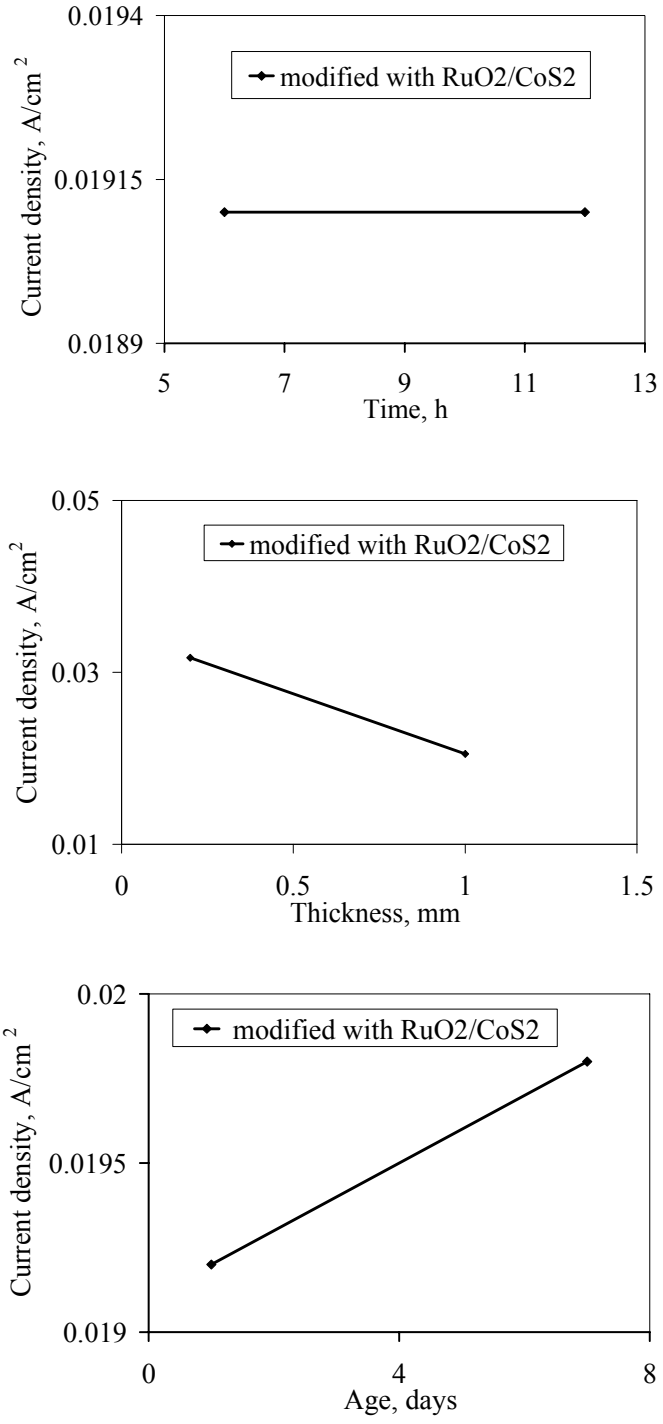

Figure 5.23 Measured effects of three process variables on cell current density. Time effect (top), electrolyte thickness (center), electrolyte age (bottom).

6 CONCLUSIONS AND RECOMMENDATIONS

In this investigation, a novel thin MEA from a solid acid material ($CsHSO_4$) and innovative composite anode electrocatalysts have been developed for the electrolytic splitting of (100 %) H_2S feed content gas operating at 135 kPa and 150 ^oC. A new class of anode electrocatalyst with general composition, RuO_2/CoS_2, and an improved proton conductor, $CsHSO_4$, have shown great stability and desired properties at typical operating conditions. This configuration showed stable electrochemical operation for 24 hours with a (100 %) H_2S fuel stream at 423 K. This same system exhibited a maximum current density of (19 mA/cm^2) at 900 mV. The performance of this new anode electrocatalyst when compared to that of Pt black investigated in a previous study showed an overall superiority in its application with a performance of over 40 % improvement in current density. This was an unexpected turnout considering that Pt has always been regarded as the state-of-the-art electrocatalyst used both in catalyzing the anode and the cathode in many applications. In the case of Pt black, sulfur poisoning of the anode material was a major issue after 8 h of exposure to H_2S, which degraded the system performance. This poisoning effect is irreversible which led to de-lamination of the MEA materials and blockage of the diffusion layers making it difficult for feed to be transported effectively. This detrimental effect is due to the fact that the state-of-the art Pt catalytic effect is based on crystalline catalytic active sites, which depend on the surface irregularities and may not be sufficient to accommodate the effect of sulfur poisoning. This was circumvented

by introducing a composite anode material which provided superior catalytic properties compared to Pt as well as reduced cost. However, of all the resistances encountered, ionic (electrolyte) resistance dominated over others. We have achieved a 30 % increase in the overall system performance by fabricating a thin (200 μm) $CsHSO_4$ electrolyte, which reduced the whole MEA thickness from 2.3 mm to 500 μm. The result of permeability measurements proved that this thin solid electrolyte is impermeable to H_2S gas and physical integrity was preserved throughout the experimental period. Further resistance losses were compensated by using high energy planetary milling system to enhance the ionic conductivity of $CsHSO_4$. The difference in stability and electrochemical performance of our cells compared to that of Pt anode based systems is directly attributable to the anode materials developed in this project.

Factorial experiments were used to characterize the effect of controllable process variables (electrolyte thickness, time, age of the electrolyte) on the cell current density and interfacial polarization resistances. As expected, cell current density and interfacial polarization resistances were a function of electrolyte thickness and age. Nevertheless, the effect of electrolyte thickness has a more prominent effect on the measured parameters. In addition, these experiments were used to identify regions of optimum system performance.

Tafel plots were constructed to investigate the kinetic behavior of various anode based electrocatalysts. Exchange current densities, which are directly a measure of the electrochemical reaction kinetics, increased with RuO_2/CoS_2-based anodes. These

experiments also suggested that high levels of fuel utilization were possible using these materials. This was an impressive result considering the drastic improvement in electrochemical performance, current density, and sulfur tolerance compared to e other anode configurations.

6.1 **Increase Reactant Concentration**

The thermodynamic benefit to increasing reactant concentration is minor due to the logarithmic form of the Nernst equation. In contrast, the kinetic benefit to increasing reactant concentration is significant, with linear rather than logarithmic impact. By operating the electrolytic cell at higher pressure, we can increase the reactant gas (H_2S), improving the kinetics commensurately. Unfortunately, the kinetic penalty due to decreasing reactant concentration is likewise significant. Again, reaction concentration tends to decrease at cell electrodes during high current density operation due to mass transport limitations. Essentially, the reactants are being consumed at the TPB faster than they can be replenished, causing the local reactant concentrations to diminish. This interaction between kinetics and mass transport was not part of this investigation. In this study, we have improved j_o by decreasing the activation barriers and increasing the number of possible reaction sites using the novel anode composite RuO_2/CoS_2.

6.2 **Electron Collection**

The bulk of the resistance in $CsHSO_4/RuO_2/CoS_2$-based cells can be directly attributed to the current collector and lead wires. They accounted for over 70 % of the bulk cell resistance. The system was setup such that leads and current collector (carbon mesh) are

attached to the electrolytic anode. The same type of setup was carried out in the cathode section. Differences in the thermal expansion properties of RuO_2/CoS_2, the mesh current collector, and the $CsHSO_4$ electrolyte lead to a partial de-lamination of the anode from the electrolyte pellet after prolonged operation. Despite that the anode was still in direct contact with the electrolyte, the contact region between both components was reduced, causing an increase in the bulk cell resistance.

One way of minimizing the cell resistance will be to replace the carbon mesh current collector. The MEA was expected to have lower electric conductivity compared to the carbon mesh, and this will result in low electrochemical activities and increase in ohmic polarization of the anodic cell. Another possibility would be the layering of conductive material over the MEA anode prior to cell operation. Thin metal plates with a corrosion resistant surface can significantly reduce the volume and weight of an electrolytic system, although the long term stability of such coatings needs improvement[77]. This will ensure smooth electron and gas transport and consequently, minimize ohmic polarization of the cell.

The most commonly used material for low temperature fuel cell flow plates is graphite. This can be applied to electrolytic cells as well because it satisfies most of the criteria discussed except: ease of manufacturability, cost, and high mechanical strength. These criteria are not fulfilled because of costly machining requirements and intrinsic brittleness of the material. New materials have to be sought or promising technology capable of

making graphite cost competitive and ease of manufacture are in place. This material is stable and electronically conductivity over a wide temperature range in H_2S atmosphere.

REFERENCES

1 J. K. Kroschwitz, M. Howe-Grant (eds.), Encyclopedia of Chemical Technology, Vol. 23, Wiley Press, pg. 276, New York (1997).

2 N. Keller, C. Pham-Huu, C. Crouzet , M. J. Ledoux , S. Savin-Poncet , J.B. Nougayrede, J. Bousquet , Catalysis Today 53**,** 535–542, (1999).

3 D.A. Boysen, C.R.I. Chisholm, S.M. Haile, S.R. Narayanan, J. Electrochem. Soc. 47 3610 (2000).

4 B. Zhu, Fuel Cell Bull*.,* 4, 9, (1999).

5 H. Iwahara, in Proc. 17th Risø Int. Symp. Mat. Sci. (eds Poulsen, F. W. et al.) 13–28 (Risø National Laboratories, Roskilde, Denmark, (1996).

6 S. M. Haile, D. A. Boysen, C. R. I. Chisolm, R. B. Merle, Nature 410, 910 (2001).

7 K. D. Kreuer, J. Membr. Sci*.* 185, 29 (2001); Solid State Ionics 125, 285 (1999).

8 R. Parsons, Trans. Faraday Soc. 54, 1053 (1958).

9 S. Trasatti, J. Electroanal.Chem, 111, 125 (1980).

10 J. A. Rodriguez and M. Kuhn, J. Vac. Sci. Technol. A*,* 14, 1609 (1996).

11 J. Donini, K.T. Chuang, S.V. Slavov, A. R. Sanger and V. Stanic, US 6,241,871 B1, June 5 (2001).

12 T. J. Kirk and J. Winnick, J. Electrochem. Soc*.,* 140, 3494 (1993).

13 Tetsuya Uda and Sossina M. Haile,z, Electrochemical and Solid-State Letters, 8, 5, A245-A246 (2005).

14 T. Chivers, J. B. Hyne, and C. Lau, Int. J. Hydrogen Energy, 5, 499 (1980).

15 http://www.wpbschoolhouse.btinternet.co.uk/pg. 04/4_75trans.htm.

16 Jurado J F, Ortiz E and Vargas R A Meas. Sci. Technol. 8 1151–5, (1997).

17 R. Fitzgerald, Solid State Ionics 125, 285 (1999).

18 J. A. Rodriguez and M. Kuhn, J. Vac. Sci. Technol. A, 14, 1609 (1996).

19 T. Uda, S. M. Haile, Electrochemical and Solid-State Letters, 8, 5, A245-A246 (2005).

20 T. Uda, D. A. Boysen, S. M. Haile, Solid State Ionics 176, 127–133 (2005).

21 B. Yang, A.M. Kannan, A. Manthiram, Materials Research Bulletin 38 691–698 (2003).

22 A.I. Baranov, L.A. Shuvalov, N.M. Shchagina, JETP Lett. 36 459 (1982).

23 A. Pawlowski, Cz. Pawlaczyk, B. Hilzcer, Solid State Ionics 44 17 (1990).

24 T. Norby, M. Friesel, B.E. Mellander, Solid State Ionics 77 105 (1995).

25 V.V. Sinitsyn, A.I. Baranov, E.G. Ponyatovsky, L.A. Shuvalov, Solid State Ionics 77 118 (1995).

26 A.V. Belushkin, M.A. Adams, S. Hull, L.A. Shuvalov, Solid State Ionics 77, 91 (1995).

27 K. Itoh, T. Ukeda, T. Ozaki, E. Nakamura, Acta Crystallogr., C Cryst. Struct. Commun. 46, 358 (1990).

28 A.V. Belushkin, W.I.F. David, R.M. Ibberson, L.A. Shuvalov, Acta Crystallogr., B47 161 (1991).

29 J. Lipkowski, B. Baranowski, A. Lunden, Pol. J. Chem. 67 1867 (1993).

30 C.R.I. Chisholm, S.M. Haile, Mater. Res. Bull. 35 999 (2000).

31 J. Baran, M. K. Marchewka, Journal of molecular structure, pg. 133- 149 (2002).

32 C. R. I. Chisholm and S. M. Haile, Materials Research Bulletin 35 999–1005 (2000).

33 A.M. Balagurov, A.I. Beskrovnyi, B.N. Savenko and B.V. Merinov. Phys Status Solidi A 100, pg. K3–K7 (1987).

34 P.L. Antonucci, A.S. Arico, P. Creti, E. Ramunni, V. Antonucci, Solid State Ion 125 431 (1999).

35 T. Ishii, J. Kawamura, J. Phys. Soc. Jpn., 67 (10), pg. 3517 (1998).

36 M.G. Lazarraga, J. Ibanez, M. Tabellout, J.M. Rojo, Composite Science and Technology, 64, pg. 759-765 (2004).

37 S.M. Haile, Solid State Ionics and Electroceramics Research Group, Improved solid acid electrolyte at Caltech, Materials Science Department, Pasedena, California, USA, (2004).

38 J. Otomo, N. Minaga, Solid State Ionics, 156, pg.357-369 (2003).

39 E. Ortiz, R.A. Vargas, B.E. Mellander, J. Phys.: Condens. Matter 18 pg. 9561–9573 (2006).

40 J. Maier, J. Phys. Chem. Solids, 46 (3), pg.309 (1985).

41 Ph. Colomban, M. Pham-Thi, A. Novak, Solid Sate Ionics, 24, pg. 193- 203 (1987).

42 K. Itoh, T. Ozaki, E. Nakamura, International Union of Chrystallography, 37B, pg.1908-1909 (1981).

43 H. Matsunaga, K. Itoh, E. Nakamura, Journal of the Physics Society in Japan, 48, pg. 2011-2014 (1980).

44 M. Pham-Thi, Ph. Colomban, A. Novak and R. Blink, Journal of Raman Spectroscopy, 18, pg. 185 (1987).

45 A. Goypiron, J. de Villepin and A. Novak, Journal of Raman Spectroscopy, 9, pg. 297 (1980).

46 L. Borjesson and L.M. Torell, Physics Review, 32, pg. 2471 (1985).

47 Ph. Colomban, M. Pham-Thi and A. Novak, Solid State Ionics, 21, 1986, pg.125.

48 C. Berger (Ed.). Handbook of Fuel Cell Technology. Prentice-Hall, Englewood Cliffs, NJ, (1968).

49 R. Bird, W. Stewart, and E. Lightfoot. Transport Phenomena, 2nd ed. Wiley, New York, (2002).

50 E. L. Cussler. Diffusion: Mass Transfer in Fluid Systems. Cambridge University Press, Cambridge, (1995).

51 F. Delogu, G. Cocco, Journal of Alloys and Compounds 436, pg. 233-240 (2007).

52 Sossina M. Haile, Dane A. Boysen, Calum R. I. Chisholm & Ryan B. Merle *Nature* |Vol 410 | 19 April 2001 |www.nature.com.

53 Sossina Haile, Fuel Cells : Powering Progress in the 21st Century

54 B. Krakow, E. Weaver, L. Ecklund-Mitchell, E. Stefanakos, G. Moore, and M.Smith, in The 22nd Annual International Coal Conference, University of Pittsburgh, pg. 191/1-191/8 (2005).

55 T. J. Kirk and J. Winnick, J. Electrochem. Soc., 140, 3494 (1993).

56 Zha, Shaowu Electrochem. Solid-State Lett., Volume 8, Issue 8, pg. A406-A408 (2005).

57 D.A. Agievskii, M.V. Landau, and A. A. Slinkin, kinet. Katal., 29,792 (1989).

58 B.J. Bladergroen, F. Meyer, S. Pasupathi, V. Linkov, International Journal of Hydrogen Energy 33 3031-3035 (2008).

59 C. Berger (Ed.). Handbook of Fuel Cell Technology. Prentice-Hall, Englewood Cliffs, NJ, (1968).

60 L.I. Antropov, Theoretical Electrochemistry (Moscow: Mir Publishers), pg. 418 (1981).

61 http://www.gamry.com.

62 PANalytical X'pert Highscore (PW 3209) Software, Version 1.0F, (2004).

63 C. R. I. Chisholm, Y. H. Jang, S. M. Haile, and W. A. Goddard III, Phys. Rev. B 72, 134103 (2005).

64 F.D. Morrison, D.C. Sinclair, A.R. West, J. Appl. Phys. 86 (11) 6355- 6365 (1999).

65 J.R. Macdonald, Impendance Spectroscopy, Wiley, pg. 191- 205 (1987).

66 T. Ito, H. Kamimura, J. Phys. Soc. Jpn, Vol. 67, No. 6, pg. 1999-2007, June, (1998).

67 E. Ortiz, R. A. Vargas and B.E. Mellander, J. Phys.: Condens. Matter 18**,** 9561–9573, (2006).

68 J. Mbah, B. Krakow, E. Stefanakos, and J. Wolan, J. Electrochem. Soc. 155 (11) (2008) E166-E170.

69 A. Saito and H.C. Foley, AIChE Journal, 37, (1991) 429.

70 G. Horvath and K. Kawazoe, Method for the Calculation of Effective Pore Size Distribution in Molecular Sieve Carbon, J. Chem. Eng. Japan, Vol 16, No. 5, pp (1983) 470-475.

71 A.V. Belushkin, M. A. Adams, S. Hull, A. L. Kolesnikov, L. A. Shuvalov, Phys. B Condens Matter , 213-214, 1034-6 (1995).

72 A. I. Baranov, L. A. Shuvalov and N. M. Shchagina JETP Lett. 36 459–62 (1982).

73 T. Uda, D. A. Boysen, S. M. Haile, Solid State Ionics 176, pg.127–133 (2005).

74 M. H. Chahbani and D. Tondeur, Fundamentals of Adsorption, Vol. 6, F. Meunier (Ed.). Elsevier, New York, (1998).

75 G. Dagan, Flow and Transport in Porous Formations, Springer-Verlag, Berlin, (1989).

76 E. R. Gilliland, R.F. Baddour, G. P. Perkinson, and K. J. Sladek, Ind. Eng. Chem. Fundam., 13, 95, 100 (1974).

77 R.C. Makkus, A. H. H. Janssen, F. A. de Bruijn, and R. K. A. M. Mallant. Use of stainless steel for cost competitive bipolar plates in the spfc. Journal of Power Sources, 86 (1): 274-282, (2000).

APPENDICES

Apendix A Cell Preparation and H_2S Splitting

A.1 $CsHSO_4$ Synthesis

Solid Acid ($CsHSO_4$) can be synthesized by the method of the two reactions below:

a. $Cs_2SO_4 + H_2SO_4 \rightarrow 2CsHSO_4$ (A.1.a)

b. $Cs_2CO_3 + 2H_2SO_4 \rightarrow 2CsHSO_4 + CO_2 + H_2O$ (A.1.b)

Sulfuric acid has a molecular weight of 98.08, specific gravity of 1.84gm/ml and a concentration of 95.7 %. The molecular weights of cesium sulfate and cesium carbonate are 361.88 and 325.82 respectively. Using pure H_2SO_4 with 95.8 % purity gives,

0.957 x1.84gm/ml = 1.76088 gm/ml (specific gravity of H_2SO_4). From equation (A.1a), the amount of Cs_2SO_4 required for every 1 mil of H_2SO_4 = (1.76272 x 361.88)/98.08

= 6.497 gm/ml

Similarly, from equation (A.1b) the amount of $CsCO_3$ required for every mil of H_2SO_4 = (1.76272 x 325.82)/2 x 98.08

= 2.9278 gm/ml

Preparation of $CsHSO_4$ using $CsSO_4$

a. A measured quantity of $CsSO_4$ (6.504 g) was dissolved in 4 ml of DI water at 34 ^oC.

b. A (1.0 ml) H_2SO_4 was added to the solution, which raised the temperature to 64 ^oC (exothermic reaction).

Appendix A (Continued)

c. At the completion of reaction, the product is left to cool down in the hood until it starts to precipitate at 24 ^{o}C. At this point, the precipitation process was accelerated by the addition of 5 ml of acetone which was previously cooled with liquid nitrogen.

d. The crystalline precipitate which was at 8 ^{o}C is separated using a vacuum pump. At this temperature the filtrate is clear without any colloidal suspension. Also the liquid nitrogen helped to provide chilling effect to the resulting mixture on precipitation.

e. Then the resulting crystalline powder is vacuum dried using Schlenk filteration manifold at 80 ^{o}C overnight.

f. The crystalline powder was then ball milled in a high energy planetary mill for 3 h.

g. The next stage involved baking of the powdered sample in an Autosorb apparatus in outgassing station in nitrogen atmosphere at 150 ^{o}C to produce a pure homogeneous crystal sample.

h. Using an evacuated die set, the crystalline sample was pressed to make pellets of 0.5'' and 2'' diameter depending on the application desired.

A.2 Pellets Preparation

Pellet sizes of $CsHSO_4$ were prepared using pellet diameters 0.5'' and 2'' and thickness range (1-0.2 mm). The calculations outlined below show the amount of $CsHSO_4$ required for each diameter using 1 mm thick pellet for illustration.

a. 0.5'' diameter pellet and 1 mm thickness:

Volume =Area x 1 x 25^2

= ($\prod D^2$ x 25^2 x 1)/4

Appendix A (Continued)

$= (\prod \times 0.5^2 \times 25^2 \times 0.001)/4$

$= 0.1227$ ml

Density = mass/volume

Mass = Density x volume

Density of $CsHSO_4$ = 3.352 gm/ml

Mass of $CsHSO_4$ required = 3.352 x 0.1227

= 0.4113 gm

For 0.5 mm thickness we need

Volume =Area x 0.5 x 25^2

$= (\prod D^2 \times 25^2 \times 0.0005)/4$

$= (\prod \times 0.5^2 \times 25^2 \times 0.0005)/4$

$= 0.061328$ ml

Density = mass/volume

Mass = density x volume

Density of $CsHSO_4$ = 3.352 gm/ml

Mass of CsHSO4 required = 3.352 x 0.0613

= 0.2056 gm

For 0.2 mm thickness

Volume =Area x 0.2 x 25^2

$= (\prod D^2 \times 25^2 \times 0.0002)/4$

Appendix A (Continued)

$= (\prod \times 0.5^2 \times 25^2 \times 0.0002)/4$

$= 0.02453$ ml

Density = mass/volume

Mass = density x volume

Density of $CsHSO_4$ = 3.352 gm/ml

Mass of $CsHSO_4$ required = 3.352 x 0.02453

= 0.0822 gm

b. 2'' diameter pellet

Volume = $(\prod \times 2^2 \times 25^2 \times 0.001)/4$

=1.9635 ml

Mass of $CsHSO_4$ required = 1.9635 x 3.352

= 6.5816 gm

A.3 Computation of H_2S Flowrate Required for both the 0.5'' and 2'' Cells

Hydrogen sulfide will split according to the following equation:

$H_2S \rightarrow 2H^+ + ½\ S_2 + 2e^-$ (A.3.1)

The current density target obtained from literature, for this process is 0.030 A/cm^2

Current, A = C/s

For 0.5'' diameter cell:

For an active area of pellet of 0.281 diameter,

$A = \prod D^2/4$

Appendix A (Continued)

$= \prod (0.281)^2/4 = 0.062 in^2 = 0.4\ cm^2$

Faraday requirement:

96400 Coulombs = 1 Faraday

1 Faraday = 1 mole of electron

From equation (A.3.1),

(96400 C/mole electron) x (mole 2 e^-/moles H_2S) = 192800 C/moles H_2S

The amount of current required = current density x active area of electrolyte

(Amp/cm^2) x cm^2= C/s=Amp

Amp = (0.030A/cm^2) x 0.4cm^2 = 12 mA

Therefore, flowrate of H_2S per electron is given by,

H_2S flowrate = 12 x10^{-3} C/s x [1/ (96400 C/moles H_2S)]

= 1.24 x 10^{-7} moles/s

1 mole of gas contains 22400 cm^3

(1.24 x 10^{-7} moles/sec) x 22400 cm^3/mole = 0.16 cm^3/min

Time Required to Electrolyze 1 mole of H_2S

Amperes x time = C

$$\text{Time (sec)} = \frac{192970\ \text{C/moles } H_2S}{12 \times 10^{-3}\ \text{C/s}} = 1.61 \times 10^7\ \text{s/mole } H_2S$$

And 1.61 x 10^7 s/mole

or

1 mole of sulfur in 186 days

Appendix A (Continued)

1 mole S = 32g of sulfur

Density of sulfur = 2.07g/cm^3

Atomic volume = 15.46 cm^3

1 mole ≡ 15.46 cm^3 sulfur ≈ 186 days

1 ml sulfur ≡ 186/15.46 = 12 days

1 day ≡ 1/12 = 0.08 ml/day of sulfur

For 2'' diameter Cell:

Active area of pellet = 1.4760 in ≈ 1.5''

Area in cm^2 = ∏ x $(381000)^2/4$ = 11.395 cm^2

Current density, j = 0.030A/cm^2

Amp = 0.030A/cm^2 x 11.4 cm^2 = 0.342 C/s

H_2S Flowrate = (0.342 C/s) x [1/ (192970 C/moles H2S)]

= 1.772 x 10^{-6} moles/s

= 2.38 ml/min of sulfur

Time Required to electrolyze 1 mole of H_2S

Time (s) = (192970 C/moles H_2S)/ (0.342 C/s)

= 81012.907 s/mole H_2S

= 1 day

1 mole sulfur ≡ 32g sulfur

Density of sulfur = 2.07 g/cm^3

Atomic volume of sulfur = 15.46 cm^3

Appendix A (Continued)

1 mole sulfur ≡ 15.46 cm^3 sulfur ≈ 1 day

1 ml sulfur = 1/15.46= 0.06 ~1.5 h

A.4 Gasket and O ring for the ½'' Cell

Both the O-rings and the gasket were from (CTG). These are all made from aflas material which can withstand the effect of H_2S on them. The inner O-ring has the dimension: OD (0.441'') and the ID (0.301'') while the outer O-ring has the dimension: OD (2.270'') and the ID (1.850'').

O-ring thickness = (OD-ID)/2

Gasket dimension is calculated from the formula below.

Gasket thickness = Pellet thickness + 2 [O-ring (inner) thickness] – 2 (grove depth)

=1 mm + 2(0.07'') - 2(0.05'')

= 0.04'' + 0.14 – 0.1'' = 0.08''

Gasket size = OD (1.8'') x ID (0.64'') x Thickness (0.0625'')

ID of gasket is a little bigger than ID of pellet to allow for pellet fitting, and the OD is a little smaller than OD of cell to be able to accommodate the outer O-ring. The thickness is made to be a little smaller than the calculated value.

A.5 System Pressure

A PX481A pressure transducer from Omega engineering with 9-30 VDC/output: 1-5 VDC and range: 0-30 psig and accuracy of ± 0.5 % FS maximum was used with the

Appendix A (Continued)

data acquisition (DAQ) instrument. This was linked to LabView DAQ and the conversion for the transducer is shown in Figure A.5.1:

V = (1-5) V

P = (0-30) psig

P = 30/4 (V-1)

P = 7.5 (V-1)

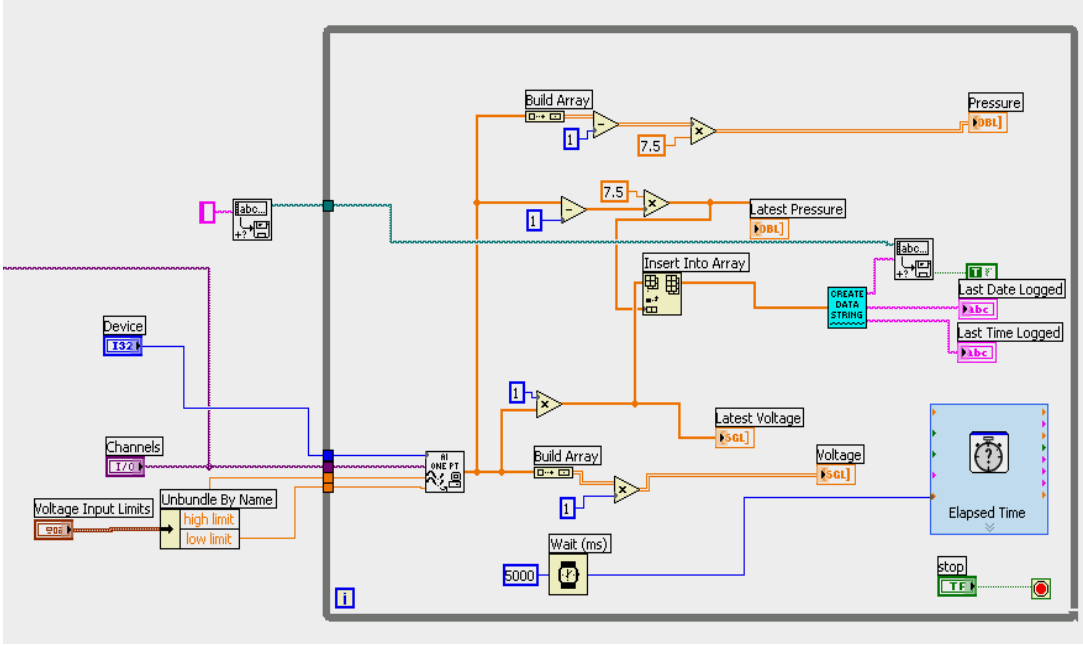

Figure A.5.1 A LabView block diagram for monitoring system pressure.

Appendix A (Continued)

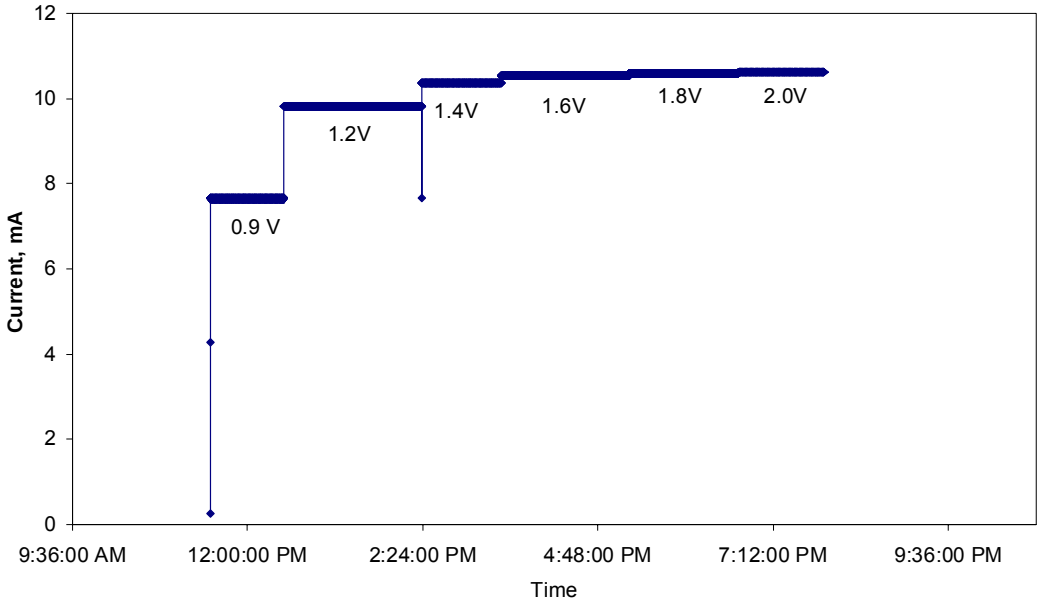

Figure A.5.2 A sample LabView representation of an electrolytic system. Comprising of anode based RuO_2/CoS_2 and cathode based Pt black at different voltage input.

The sulfur collection vessel is filled with mineral oil to the same height where the liquid sulfur exits the cell to avoid oil being sucked into the cell as a result of this vacuum created by a higher oil level than the sulfur exit point in the cell before the start of the experiment.

$$P_{atm}\,\text{oil} = P_{atm}\,\text{cell} \quad \text{(before experiment)}$$

$$P_{abs}\,\text{cell} = P_{atm}\,\text{cell} + \text{gauge pressure (~1-2 psig)} \quad \text{(experiment start up)}$$

The flow of sulfur will then push oil in the line back since pressure in the cell is higher than the oil pressure. It is assumed that the rise in oil level due to sulfur production will not be enough to off set this balance and reverse the flow of sulfur.

Appendix A (Continued)

A.6 Material Balance

The electrolysis of H_2S produces hydrogen at the cathode and sulfur at the anode. A steady voltage of 0.9V is allowed to flow through hydrogen sulfide for 5 hours, splitting it at a sustainable current of 5.31 mA. Mass of sulfur deposited at the anode.

Method:

Sulfur analysis

a. The half equation for the electrolysis.

$$H_2S \rightarrow 2H^+ + 2e^- + (1/8)\ S_8 \qquad \text{(A.6.1)}$$

2 moles of electrons (2 Faradays) are required to deposit 1/8 mole of sulfur.

b. Number of Faradays that have passed through the hydrogen sulfide in 5.31 hours.

$$Q = I \times t \qquad \text{(A.6.2)}$$

5.31 hours contains (5.31 x 60 x 60) seconds

= 18,000 seconds.

Q = (5.31 x 18,000)/1000

= 95.58 Coulombs.

1 Faraday = 96,400 coulombs.

95.58 coulombs = 95.58 ÷ 96,400 Faradays

= 0.001 Faradays.

c. From the proportion in (A.6.1), 2 Faradays (2 moles of electron) are required to produce (1/8) mole of sulfur and 2 moles of hydrogen ions. This is sufficient to produce

Appendix A (Continued)

0.001 moles (0.001g) of hydrogen ions and 6.25E-5 moles (0.016g) of S_8.

Hydrogen analysis: The half equation for the electrolysis

$$2H^+ + 2e^- \longrightarrow H_2 \qquad \text{(A.6.3)}$$

The 2 moles of hydrogen ions produced in Eqn. A.6.1 are converted to 1 mole of hydrogen gas in Eqn. A.6.3. The 0.001 moles (0.001g) of hydrogen ions produced at the anode by 0.001 Faraday are converted to 0.0005 moles (0.0005g) of hydrogen gas at the cathode.

For the gas measurement, the gas issuing from the cathode compartment was collected and measured by displacement of water in a 50 ml burette at 25 ^oC and 102.4 kPa. The observed volume was 10 ml. Gas collected by displacement of water is saturated with water vapor whose vapor pressure at 25 ^oC is 3.17 kPa. The partial pressure of hydrogen in the burette was then (102.4 -3.17) 99.2kPa. By the ideal gas law, 0.0004 moles of gas has a volume of 10 ml at a partial pressure of 99.2 kPa and temperature of 25 ^oC. Thus the measured volume of hydrogen gas is about 80 % of the theoretical limit for the electrolysis as calculated in the previous section. When the water level is equal in the test tube and the trough, the pressure inside the test tube will be equal to the atmospheric pressure. Ideal gas law is used to determine the number of hydrogen moles in the test tube. The water displaced by hydrogen has vapor pressure that will distort the equation if not accounted for because of the Dalton's Law of partial pressure: the pressure in the test

Appendix A (Continued)

tube is from both the hydrogen and the water. To find just the hydrogen, the vapor pressure of the water has to be subtracted. Vapor pressure of water is published in most chemistry books, and varies by the temperature of the water.

Calculations using Dalton's law:

In our lab, the atmospheric pressure is 102.4 kPa (768 torr or 1 atm). The temperature of our water is 25 °C. We used a 10 mL test tube to collect the hydrogen. The pressure of the hydrogen will be calculated, and then moles of hydrogen are obtained using the ideal gas law.

Step 1: We need to know the vapor pressure of the water. A common table lists the pressure at 25 °C as 23.76 torr. A torr is 1 mm of mercury at standard temperature. In kilopascals, that would be 3.17 (1 mm mercury = 7.5 kPa). We should also convert the 10 mL to 0.010 L and 25 °C to 298 °C.

Step 2: We can use Dalton's Law to find the hydrogen pressure. It would be:

$$P_{Total} = P_{Water} + P_{Hydrogen}$$

$$102.4 \text{ kPa} = 3.17 \text{ kPa} + P_{Hydrogen}$$

So the pressure of Hydrogen would be: 99.23 kPa or 99.2 kPa.

Step 3: We use the Ideal Gas Law to get the moles. Recall that the Ideal Gas Law is:

$$PV = nRT$$

where P is pressure, V is volume, n is moles, R is the Ideal Gas Constant (0.010 L-atm/mol-K or 8.31 L-kPa/mol-K), and T is temperature.

Therefore, our equation would be:

Appendix A (Continued)

$$99.2 \text{ kPa} \times 0.010 \text{ L} = n \times 8.31 \text{ L-kPa/mol-K} \times 298 \text{ K}$$

This can be re-arranged so:

$$n = 99.2 \text{ kPa} \times 0.010 \text{ L} / 8.31 \text{ L-kPa/mol-K} / 298 \text{ K}$$

$$n = .00046 \text{ mol or } 4.6 \times 10^{-4} \text{ mol Hydrogen}$$

1 coulomb is the amount of electrical charge in 6.241506×10^{18} electrons or other elementary charged particles.

The charge of one electron equal to -1.6022×10^{-19} C

1 C = 6.241506×10^{18} = Amp x s

For a theoretical 12 m A, the rate of proton (and electron) generation is approximately [$(6.241506 \times 10^{18}$ x 12 A)/1000] = 5.47 x 10^{16} electrons/s for 100 % conversion of H_2S at 48.50 Psi or 334.39 kPa,150 ^oC, and a flow rate of 0.25 cm^3/min. The sustainable current under these conditions is 5.31 m A corresponding to 3.12 x 10^{16} electrons/s for a cell that uses RuO_2, Pt.black, p-Dichlorobenzene and $CsHSO_4$ as the anode catalyst. This value agrees well with the previous calculation. Given the severe limitations on precision of the above measurements, it is seen that the values for the H_2S conversion and current generated are consistent with each other.

A.7 Product Analysis

Sulfur produced in the anode compartment was characterized using XRD and SEM. XRD analysis indicates the molten sulfur produced freezes to monoclinic crystals on cooling.

Figure A.7.1 is an XRD pattern observed on the sulfur produced and that from pure sulfur as received. Sulfur from electrolysis product matches that of pure sulfur as shown in spectra (a) and spectra (b) respectively.

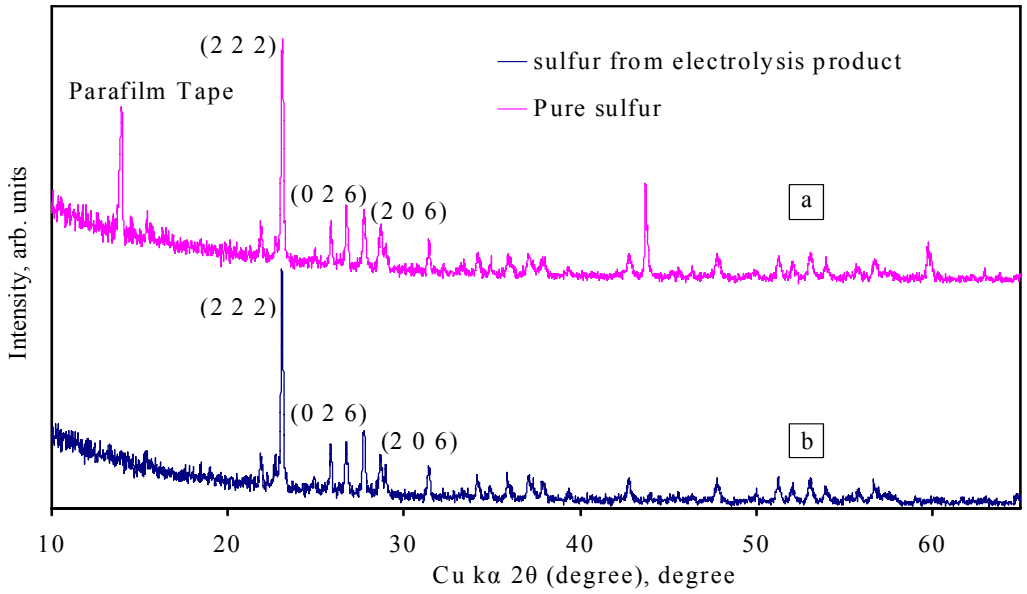

Figure A.7.1 X-ray diffraction comparison of sulfur. (a) pure sulfur; (b) sulfur from electrolysis product.

Figure A.7.2 (a) and (b) show the SEM-EDS of the electrolyzed pellet. Figure A.7.2 (a) shows SEM image of layers of yellowish sulfur deposit on the surface of the electrolyzed pellet (the area is depicted by the white background). Figure A.7.2 (b) is the EDS showing sulfur deposited on top of the electrolyzed pellet.

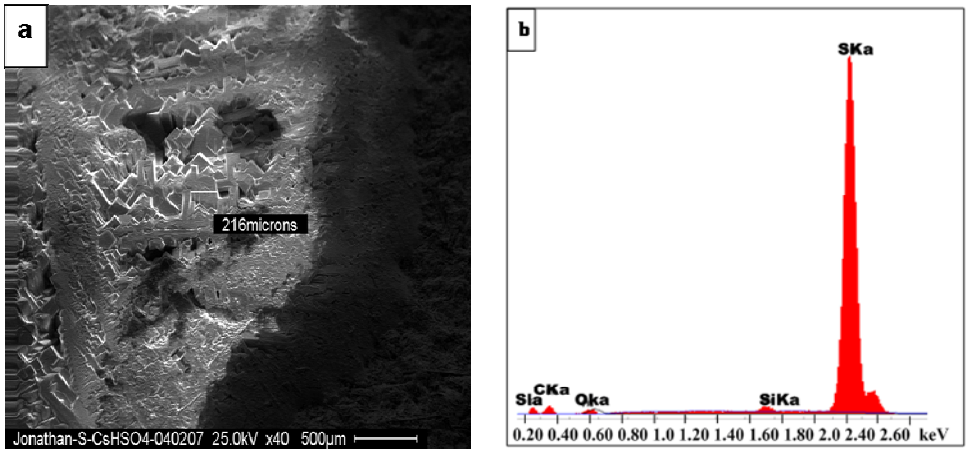

Figure A.7.2 SEM and EDS images of sulfur. Product resulting from the electrochemical splitting of H_2S: (a) SEM image showing sulfur deposit on the pellet, (b) EDS spectra showing sulfur formed from H_2S electrolysis within an area of (216) microns Sulfur formed in this region is 65 wt %.

DSC analysis indicates the molten sulfur produced is the monoclinic crystal when compared to the commercial supplied sulfur. Figure A.7.3 compares the melting point of sulfur from the electrolysis product to that of pure sulfur as received. The two spectra shown both matched each other with the melting point of pure sulfur at 119.87 ^{o}C and that from electrolysis product at 119.21 ^{o}C , but in the electrolysis other allotropes of sulfur compound are formed such as orthorhombic sulfur which has a lower melting point than the monoclinic sulfur. It is not clear at this time whether the low rate of production led to formation of sulfur molecules smaller than S_8.

Appendix A (Continued)

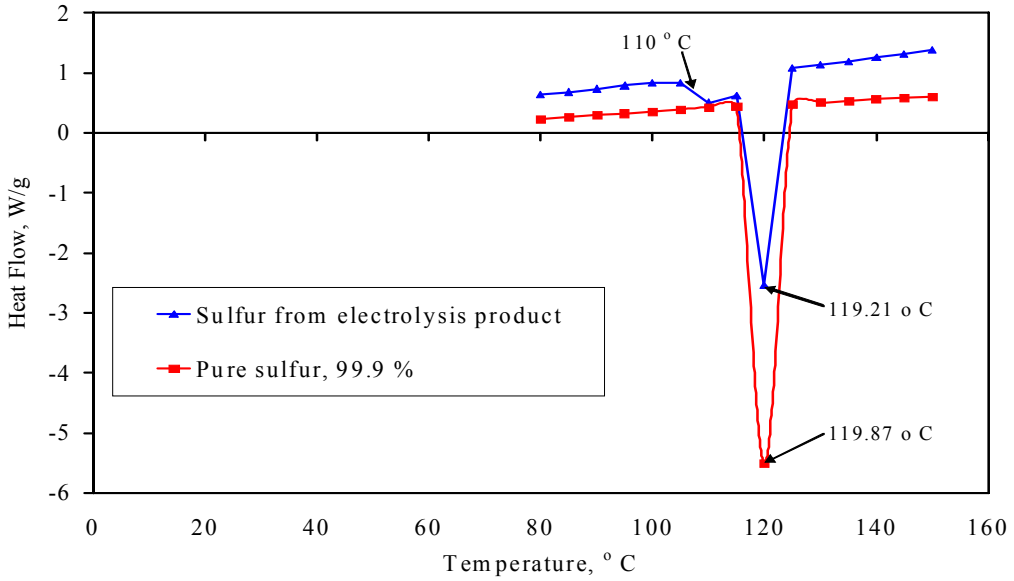

Figure A.7.3 Differential scanning calorimetry comparison of sulfur melting points.

Hydrogen gas produced was collected and measured by displacement of aqueous solution and identified by gas chromatography. The chromatogram indicated the gas contained about 15 % air. This probably infiltrated the sample even with a "gas tight syringe" while it was being transferred to gas chromatograph. Figure A.7.4 shows the gas chromatograph of hydrogen sample from the electrolysis product. The hydrogen peak produced by the sample containing about 65 % hydrogen was small because the thermal conductivity of hydrogen is almost the same as the helium carrier gas. It was too small for accurate integration to get a direct measure of the hydrogen concentration.

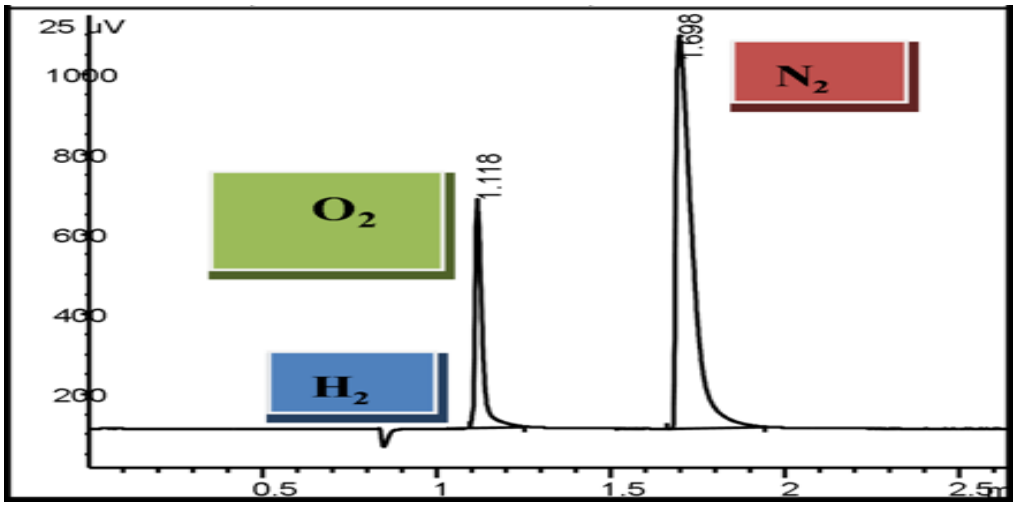

Figure A.7.4 Gas chromatograph analysis of hydrogen produced. This was by displacement of water from the electrolytical splitting of H_2S gas using helium as a carrier gas.

A.8 Graphical Comparison of the Claus and the Electrolytic Processes

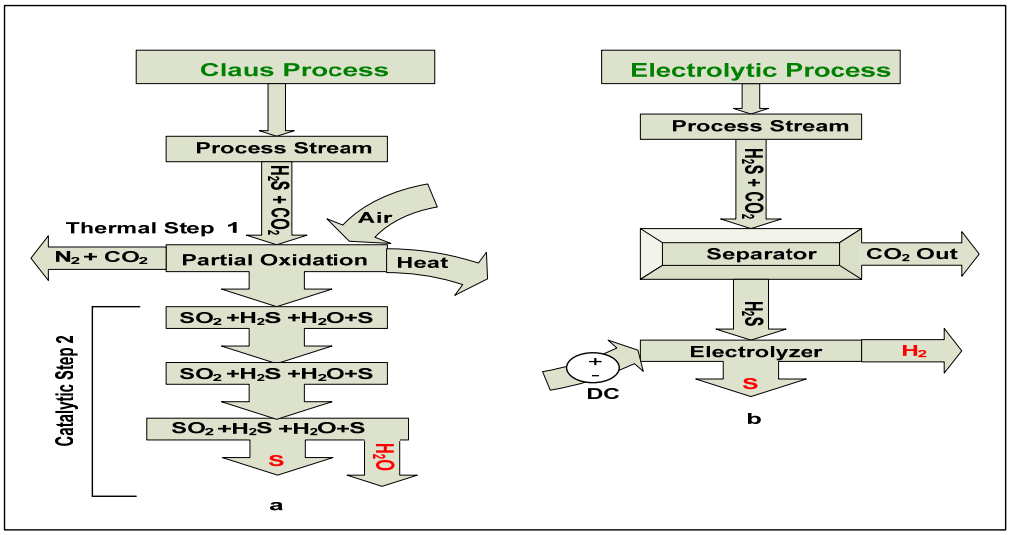

Figure A.8.1 Comparison of the Claus and the electrolytic processes. (a) Claus process: the reactions are highly exothermic and this heat is wasted; (b) one step electrolytic process: energy can be recovered as electricity.

Appendix A (Continued)

A.9 LCR Calibration

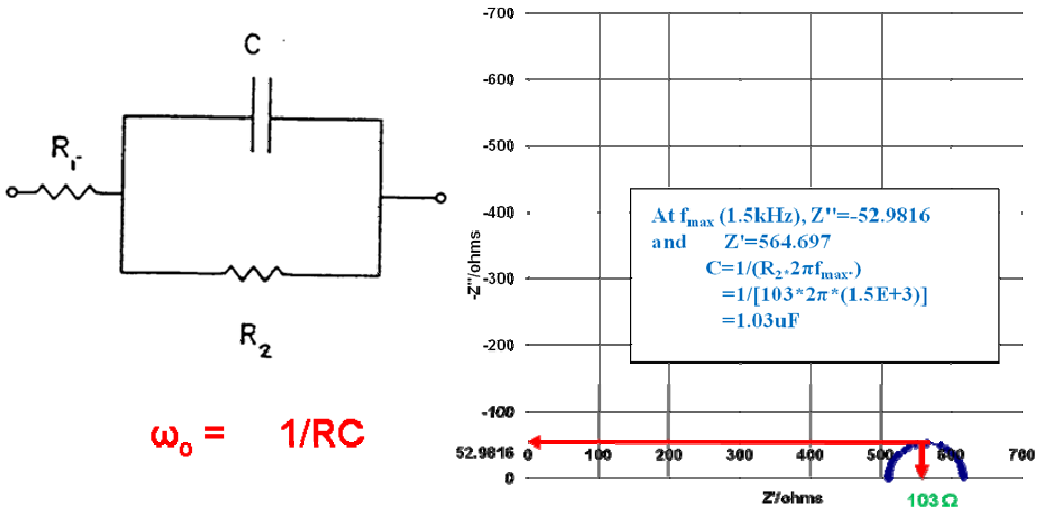

Figure A.9.1 LCR calibration with known resistors and capacitor.

Appendix A (Continued)

A.10 Thermochemistry Data

Table A.10.1 Thermochemistry data (evaluated at $T = 298$ K).

Material	ΔH(k J/ mol)	G(k J/ mol)	S (J/K mol)
$H_2S_{(g)}$	-20.1	-33.9	43.1
H_2	0	-38.96	130.68
S	0		31.8
O_2	0	-61.12	205

Reactions:

$$H_2S_{(g)} \rightarrow 1/2S_2 + H_{2(g)}$$

$\Delta H = -\Delta H_{H2S} = -20.1$ k J/mol

$\Delta S = [0.5(31.8) + 130.68] - 43.1 = 103.48$ J/Kmol

$\Delta G = \Delta H - T\Delta S$

$\Delta G = -20.1 - (298)(0.10348) = -50.937$ k J/mol = -12.17 kcal/mole

$\Delta G = -n F E$

$E^0 = -\Delta g^0 / n F$

$$E^0 = -\left[\left(\frac{-50937 J/mol}{\left(\frac{2 mole^-}{molreac}\right)\left(\frac{96{,}400 C}{mol}\right)}\right)\right] = 0.26 \text{ V}$$

ABOUT THE AUTHOR

Jonathan Chinwendu Mbah comes from the Ibo tribe in the eastern region of Nigeria. He received his B.S.Ch.E and M.S.Ch.E from University of Lagos, Nigeria, and North Carolina Agricultural and Technical State University, North Carolina respectively. In the Spring of 2006, he enrolled into doctoral program in chemical engineering at the University of South Florida where he received his Ph.D. in the Fall of 2008.